Study of Reactive and Non-Reactive Chemical Processes in Condensed Phase

by

Surma Talapatra

A dissertation submitted in partial fulfillment
of the requirements for the degree of
Doctor of Philosophy
(Chemistry)
in The University of Michigan
2014

Doctoral Committee:

Professor Eitan Geva, Chair
Professor Charles L. Brooks III
Professor Roseanne J. Sension
Assistant Professor Dominika K. Zgid

For My Parents

ACKNOWLEDGEMENTS

I would like to thank my PhD advisor, Prof. Eitan Geva, for supporting me and encouraging me throughout my PhD, and most of all, for sharing his knowledge, about condensed phase chemistry in general, and quantum mechanics in particular, and also about life occasionally. I would also want to thank the Chemistry Department at the University of Michigan for giving me the opportunity of experiencing the vibrant research environment of the campus. Next, I would like to thank my committee members, Prof. Roseanne J. Sension, Prof. Charles L. Brooks III, Dr. Dominika K. Zgid at the University of Michigan and Dr. Barry Dunietz at Kent State University for their continued support and helpful feedback on my research. I would next like to thank the past and present group members of the Geva group, Heidi Phillips, Dr. Frank Vazquez, Dr. Kijeong Kwac, Dr. Myeong Hwa Lee, Aaron White, Dr. Porsha McRobbie, Christina Franzese, Kyle Williams and Dr. Xiang Sun for helping me experience a very positive, cooperative and happy environment in the lab throughout my dissertation research. I would like to specially thank Dr. Frank Vazquez for being an amazing mentor, Dr. Kijeong Kwac for helping me with molecular dynamics simulations, and Heidi, for being an amazing lab member and friend.

I would now like to mention the people who have been a special part of my journey at the University of Michigan. First of all, I would like to thank my parents and my brother, for being there for me, encouraging me and really giving me the support that I couldn't have done without. At the same time, I am really grateful and thankful to my husband, Dr. Krishna Chaitanya Suddala, for being so generous and kind and

encouraging and most of all, for being such a positive presence in my journey at the University of Michigan.

I would also like to thank my M.Sc. thesis advisor, Dr. Charusita Chakravarty, IIT Delhi, India, for helping me realize my interest in theoretical physical chemistry and for teaching me the basics of computational chemistry. In addition, I would like to thank Dr. Hrishikesh Chatterjee, Narendrapur Ramkrishna Mission, India, and Dr. Udita Mukherjee, Lady Brabourne College, India, for igniting in me the curiosity and interest about physical chemistry during my undergraduate years at Lady Brabourne College, India.

TABLE OF CONTENTS

LIST OF FIGURES

Figure

LIST OF TABLES

Table

LIST OF ABBREVIATIONS

1. CHD - 1,3-Cyclohexadiene
2. CMD - Centroid Molecular Dynamics
3. DOF - Degrees of Freedom
4. FDF - Force Derivative Free
5. FFCF - Force Force Correlation Function
6. FT - Fourier Transform
7. HT - 1,3,5-hexatriene
8. IR - Infra Red
9. LHA - Local Harmonic Approximation
10. LJ - Lennard-Jones
11. LRT - Linear Response Theory
12. LSC - Linearized Semiclassical
13. LT - Landau Teller
14. MD - Molecular Dynamics

15. MF/MQC - Mean-Field Mixed Quantum Classical

16. NMAD - Deuterated N-methylacetamide

17. NMPIMD - Normal Mode Path Integral Molecular Dynamics

18. PI/FGR - Path Integral Fermi?s Golden Rule

19. PI/IF - Path Integral Influence Functional

20. PIMD - Path Integral Molecular Dynamics

21. PRIMPIMD - Primitive Path Integral Molecular Dynamics

22. QCF - Quantum Correction Factor

23. RESP - Restrained Electrostatic Potential

24. RFT - Reactive Flux Theory

25. TS - Transition State

26. TST - Transition State Theory

27. VER - Vibrational Energy Relaxation

28. WHAM - Weighted Histogram Analysis Method

29. Z-HT - *cis*-1,3,5-hexatriene

30. 2D - Two Dimensional

ABSTRACT

Study of Reactive and Non-Reactive Chemical Processes in Condensed Phase

by

Surma Talapatra

Chair: Prof. Eitan Geva

Chemical dynamics in condensed phase environments is dictated by an intricate interplay between reactive and competing non-reactive processes. This dissertation is aimed at the molecular level understanding of both types of processes in liquid solution environments within the framework of nonequilibrium statistical mechanics and using advanced molecular dynamics simulation techniques.

The first part of this thesis is focused on understanding quantum effects on the rates of non-reactive vibrational energy relaxation processes in several experimentally relevant systems. The systems studied include neat liquid HCl and DCl and CN^- isotopomers dissolved in H_2O and D_2O. The vibrational energy relaxation rates constants for those systems were calculated within the framework of the Landau-Teller formula. Accounting for quantum effects was achieved by calculating the vibrational energy relaxation rate constants via the linearized semiclassical method. The rate constants calculated via the linearized semiclassical method for both systems are in excellent agreement with the experimentally measured rate constants. Furthermore, comparison to the corresponding classical results suggest that quantum effects are

strongly pathway dependent and that failure to account for them can lead to misinterpretation of the molecular mechanism underlying vibrational energy relaxation in liquid solution.

The second part of this thesis is focused on understanding solvent effects on single-bond *cZt-tZt* isomerization rate constant of 1,3,5-*cis*-hexatriene dissolved in a series of explicit alkane (cyclohexane, *n*-heptane and cycloheptane) and alcohol (methanol, ethanol and *n*-propanol) solvents. The isomerization rate constants are calculated within the framework of reactive flux theory and transition state theory, at different temperatures (275-325K), via classical molecular dynamics simulations. Our results reproduce the experimentally observed trend of slower isomerization rate constants in alcohol solvents in comparison to alkane solvents. Further analysis also reveals that the experimentally observed solvent dependence may be traced back to the fundamentally different structure of the solvation shell in alcohol and alkane solvents. More specifically, whereas in alcohol solvents, hexatriene fits inside a rigid cavity formed by the hydrogen-bonded network, which is relatively insensitive to conformational dynamics, alkane solvents form a cavity around hexatriene that adjusts to the conformational state of hexatriene, thereby increasing the entropy of transition state configurations relative to reactant configurations and giving rise to faster isomerization.

CHAPTER I

Introduction

Chemistry is a study of how molecules interact with each other. One way to understand these interactions is through the study of how energy gets transferred or exchanged between molecules. Chemical processes where the energy transfer between molecules lead to the breaking and/or making of chemical bonds that eventually result in a chemical reaction are called *reactive processes*. On the other hand, chemical processes that involve transfer or exchange of energy between molecules, but do not necessarily lead to chemical reactions are called *nonreactive processes*. Chemical dynamics is all about the interplay between energy flowing into these two competing fundamental pathways leading to reactive and/or nonreactive processes.

Another fundamental classification of chemical processes is based on quantum effects. Depending on the amount of energy exchanged between molecules, the dynamics of the energy transfer can be described within the framework of classical mechanics or quantum mechanics. This categorization can be demonstrated by using the $\hbar$ scale (refer figure 1.1.) according to which, if the energy transfer is large, such that $\hbar\omega \gg k_B T$, the involved dynamics is dictated by quantum mechanics. On the other hand, if the energy transfer is such that $\hbar\omega \ll k_B T$, the involved dynamics need to be described by classical mechanics.

In my dissertation research, I have attempted to study the above mentioned fun-

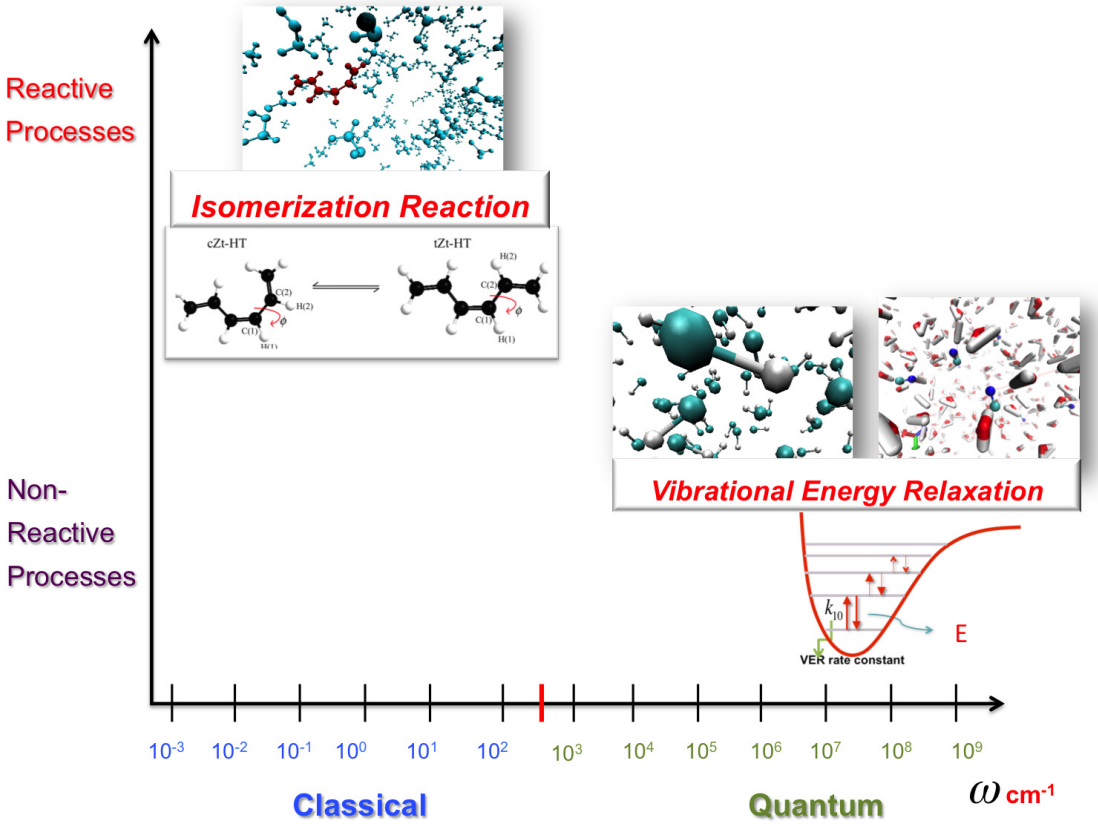

Figure 1.1: Schematic Representation of the Fundamental Classifications of Chemical Dynamics and the Chemical Processes that have been studied in this Dissertation Research.

damental aspects of condensed phase chemistry using molecular dynamics simulation methods. To this end, we have done a fully classical molecular dynamics study of the conformational isomerization between *cis*-1,3,5-hexatriene and *trans*-1,3,5-hexatriene where we have focused on understanding solvent effects on the rate and mechanism of the isomerization reaction. We have also studied a nonreactive process called vibrational energy relaxation, where we have focused on understanding quantum effects on the rate and pathway of the relaxation dynamics in two liquid systems, neat liquid HCl and DCl, and CN^- isotopomers solvated in water and D_2O. The schematic diagram given in figure 1.1 demonstrates these systems with respect to the fundamental classification of chemical dynamics.

A major part of this research has been centered around studying vibrational energy relaxation in condensed phase systems. Vibrational energy relaxation (VER) is the process where an excited vibrational mode equilibrates by transferring its excess energy into other intramolecular and/or intermolecular degrees of freedom (DOF). Understanding the time scale and mechanism of VER in condensed phase systems at the molecular level is of key importance to the understanding of chemical reactivity in solution(36; 37; 38; 39; 40; 41; 42; 43; 44; 45). Over the last several decades, VER has been studied extensively in a variety of condensed phase systems, using experimental (46; 159; 48; 49; 50; 51; 52; 53) and computational(54; 55; 56; 57; 58; 59; 60; 61; 62; 63; 64; 65; 66; 67; 68; 69; 70; 71; 72; 73; 74; 75; 76; 77; 78) techniques. These studies have demonstrated that VER can occur over a wide range of time scales, extending from subpicoseconds to minutes, via different mechanisms, depending on the frequency of the relaxing and accepting modes and the nature of the interaction between them. Recent theoretical and computational studies of VER have been mostly based on the Landau-Teller (LT) formula,(40; 155) which gives the VER rate constant in terms of the Fourier transform (FT), at the vibrational transition frequency, of the *quantum-mechanical* autocorrelation function of the fluctuating force (FFCF) exerted on the

relaxing mode by the other DOF, i.e. the bath. In systems where the energy mismatch between the relaxing and accepting modes is low, such that $\hbar\omega/k_BT \leq 1$, the VER rate constant can be calculated by replacing the quantum-mechanical FFCF with its classical counterpart(66; 82; 83; 81; 80). However, many of the vibrational transitions of interest do not fall under this category. In systems with high-energy vibrations, such that the energy mismatch between the relaxing and accepting is very high ($\hbar\omega/k_BT \gg 1$), classical description of the relaxing mode and the accepting modes is no longer suitable, and a quantum treatment of the involved dynamics is necessary.

An exact calculation of the quantum-mechanical FFCF in a condensed phase system is beyond the scope of present day computational resources due to exponential scaling of computational cost with the number of DOF. To this end, we have explored the application of semiclassical methods in the calculation of VER rate constants in high-frequency vibrational modes in condensed phase. In particular, we have applied the semiclassical method based on the linearized semiclassical (LSC) approximation(87; 62; 86; 76; 54; 56), that has been developed in the Geva group in the past several years. In our research, we have carried out the first ever implementation of the LSC approximation in the calculations of VER rate constant in case of a polar liquid system (neat liquid HCl and DCl)(78), Chapter IV, and an ionic system in polar solvent (cyanide ion in aqueous solution)(125), Chapter III. In addition, an extensive study of the VER rates and mechanisms in cyanide ion solvated in aqueous solution using classical molecular dynamics simulations and quantum correction factors has also been carried out(126) and reported in Chapter II. In the present chapter, in section 1.1, the theoretical background of the LSC method is outlined, while in Chapter II, III and IV, the various applications of the method are discussed in detail.

The other major part of the dissertation research consists of an investigation of

solvent effects on the rates of chemical reactions. Solvents can influence chemical reactions in many different ways. For example, through equilibrium properties like solvation energies and free energy surfaces, or dynamical properties such as dynamical cage effects, by solvent induced friction affecting the recrossing over the barrier top, or by affecting the diffusion of reactants towards each other(1). Molecular dynamics (MD) simulations have been frequently implemented to the study of condensed phase reactions in a number of molecular systems(213; 214; 215; 216; 217; 218; 219; 220; 221; 222; 223; 224; 225; 226), including several polyene isomerization reactions. To this end, in collaboration with the experimental research group of Prof. R. J. Sension, we have investigated the solvent effects in the single bond *cZt-tZt* isomerization reaction of 1,3,5-cis-hexatriene in alkane and alcohol solvents using classical MD simulations(126). The ultrafast photoinduced ring opening reaction of 1,3-cyclohexadiene (CHD) derives importance from various areas of research and has been extensively studied by experimental and theoretical methods over the last several decade(182; 183; 184; 185; 186; 187; 188; 189; 190; 191; 192; 193; 194; 195; 196; 197; 198; 199; 200; 201; 202; 203; 204; 205). Being a simple polyene molecule, CHD and its derivatives serve as a prototype for studying the different aspects of polyene reaction dynamics which have attracted considerable amount of attention over the past few decades due to their presence in various important biochemical processes. The multistep photochemical ring opening reaction of CHD displays an interesting spectrum of intramolecular and intermolecular energy exchange between the different polyene derivatives formed during the cascade of reactions that follow UV excitation of CHD. In addition, CHD also derives importance from the fact that the multistep ring opening reaction of CHD is similar to the photoreaction of 7-dehydrocholesterol resulting in vitamin D formation(206; 207; 208; 209; 193). Moreover, the photoinduced ring opening reaction of 1,3-cyclohexadiene (CHD) provides an excellent platform for studying several aspects of condensed phase dynamics, including the influence of sol-

vent on the thermalization of excited photoproducts and energy redistribution among the resulting ground state rotational isomers.

In the calculation of the rate constant for the single bond *cZt-tZt* isomerization reaction of 1,3,5-cis-hexatriene, we have implemented the reactive flux theory (RFT)(228; 229; 230; 231; 232; 233) and the transition state theory (TST)(235) using classical MD simulations. RFT provides a route for calculating the *exact* isomerization rate constant from MD simulations (provided of course that the dynamics can be described by classical mechanics and that the force fields are accurate). More specifically, the only assumption underlying RFT is that the rate of barrier crossing is slower than the rates of all other dynamical processes that take place in the reactant and product wells, so that the reaction dynamics can be described by a rate constant. RFT also allows the calculation of the rate constant by using trajectories that start at the barrier top, thereby bypassing convergence problems associated with rare event statistics(234). The popular TST can be obtained from RFT in the limit where barrier *recrossing* events are negligible. A detailed mathematical derivation of the RFT and TST is provided in section 1.2, while the detailed discussion of the single bond *cZt-tZt* isomerization reaction of 1,3,5-cis-hexatriene is discussed in chapter V.

1.1 Quantum Dynamics in Condensed Phase : Vibrational Energy Relaxation

Over the last few decades there have been substantial progress in the developement and application of experimental and theoretical methods in the prediction and analysis of VER rates and pathways in condensed phases. The energy relaxation of an excited vibrational mode, VER, is followed by the transfer of the excess energy to intramolecular and/or intermolecular modes available in the solute and the solvent molecules. The rates and mechanisms of VER in condensed phases has the potential

to provide a direct probe of the energy exchange dynamics which is crucial to the molecular level understanding of chemical reactions in solution.

With the advancement of ultrafast laser spectroscopy, many important experimental studies have been made in the field of ultrafast vibrational dynamics in numerous molecular systems. Among the various experimental methods, IR pump-probe spectroscopy, ultrafast IR-Raman spectroscopy, 2D-IR spectroscopy, IR photon echo method have been extensively used to study fundamental chemical phenomena like intramolecular and intermolecular vibrational energy and population relaxation, along with vibrational dephasing and vibrational coupling dynamics in a range of molecular systems including small molecules and ionic species in condensed phases(46; 159; 48; 49; 50; 51; 52; 53), metal carbonyl complexes(2; 3; 4; 5; 6; 7; 8) and biological systems(9; 10; 11; 69; 13; 14; 15; 16; 17; 18; 19; 20; 21; 22) among many others.

Along with the experimental studies numerous theoretical and computational methods have been employed for the investigation of VER at a molecular level. Theoretical description of VER rate constant in condensed phase is usually given by the LT formula, according to which, the rate constant for VER is given in terms of the FT, at the vibrational transition frequency, of a quantum mechanical autocorrelation function of the fluctuating force (FFCF) exerted by the bath DOF on the relaxing mode. In systems where the vibrational modes involved can be described by classical dynamics, the calculation of VER rate constant is particularly simplified since the quantum-mechanical FFCF can be replaced by the corresponding classical correlation function(66; 82; 83; 81; 80). However, there are a multitude of systems, where the vibrational transition frequency is comparatively large, such that $\hbar\omega/k_BT \gg 1$. In such cases, the relaxing mode and the relevant accepting modes need to be described quantum-mechanically and a classical treatment is no longer appropriate. However, the exact calculation of the quantum-mechanical FFCF is extremely diffi-

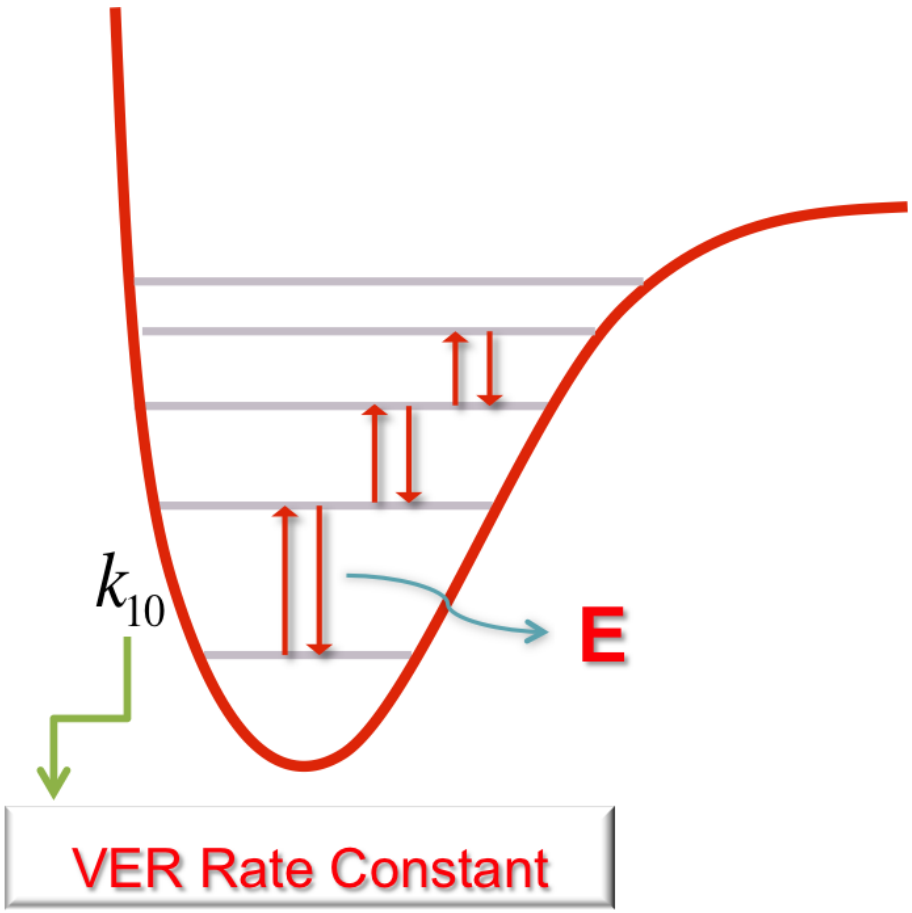

Figure 1.2: Schematic Representation of Vibrational Energy Relaxation

cult for systems with more than a few DOF. To this end, for the last few decades, there have been a huge advancement in the development of theoretical methods that can capture the quantum effects, with rigorous approximation, in the calculation of dynamical properties in significantly large systems. Some of the key examples include mixed quantum-classical methods, centroid molecular dynamics and methods based on semiclassical approximations(23; 24). These methods have been applied to a wide spectrum of important systems and, in many cases, have been successful in capturing quantum dynamical properties.

In a series of recent publications,(87; 62; 86; 76; 54; 56) Geva and co-workers have pursued a rigorous approach for calculating VER rate constants which can account for quantum effects within the framework of the LSC approximation. This approximation amounts to linearizing the forward-backward action in the exact path-integral expression for the quantum-mechanical FFCF with respect to the difference between the forward and backward paths(122). In the following subsections a detailed theoretical background of the LSC approximation and its application to the calculation of VER rate constant for high-frequency vibrational modes in condensed phase is discussed in detail. The application of the LSC approximation to various condensed phase systems are discussed in chapters II, III and IV.

1.1.1 Theoretical Background

In this subsection the linearized semiclassical (LSC) approximation is introduced. The LSC approximation is one of the rigorous approaches that are employed for the calculation of dynamical quantities in the framework of quantum mechanics in condensed phase systems. The LSC approximation can be derived by linearizing the forward-backward action in the path-integral expression for the quantum-mechanical correlation function with respect to the difference between the forward and backward trajectories(122). The resulting LSC approximation for a real time correlation

function has the following form:

$$Tr(e^{-\beta\hat{H}}e^{i\hat{H}t/\hbar}\hat{B}e^{-i\hat{H}t/\hbar}\hat{A}) \approx \frac{1}{(2\pi\hbar)^f}\int \boldsymbol{dq_0}\int \boldsymbol{dp_0}\times \\ (\hat{A}e^{-\beta\hat{H}})_W(\boldsymbol{q_0},\boldsymbol{p_0})B_W(\boldsymbol{q_t}^{(Cl)},\boldsymbol{p_t}^{(Cl)}) \tag{1.1}$$

Here, f is the number of DOF, $\boldsymbol{q_0} = (q_0^{(1)},...,q_0^{(f)})$ and $\boldsymbol{p_0} = (p_0^{(1)},...,p_0^{(f)})$ are the corresponding coordinates and momenta

$$A_W(\boldsymbol{q_0},\boldsymbol{p_0}) = \int d\Delta e^{-ip_0\Delta/\hbar}\left\langle \boldsymbol{q_0}+\Delta/2|\hat{A}|\boldsymbol{q_0}-\Delta/2\right\rangle \tag{1.2}$$

is the Wigner transform of $\hat{A}$ [with $\Delta = (\Delta^{(1)},...,\Delta^{(f)})$], and $\boldsymbol{q_t}^{(Cl)} = \boldsymbol{q_t}^{(Cl)}(\boldsymbol{q_0},\boldsymbol{p_0})$ and $\boldsymbol{p_t}^{(Cl)} = \boldsymbol{p_t}^{(Cl)}(\boldsymbol{q_0},\boldsymbol{p_0})$ are propagated classically with the initial conditions $\boldsymbol{q_0}$ and $\boldsymbol{p_0}$.

In the following subsections the theoretical derivation of the LSC approximation and its application to the calculation of VER rate constant is outlined in detail. To this end, in subsection 1.1.2 the theoretical basis for **path integral technique** is outlined which is essential for the understanding of the LSC approximation, followed by the theoretical derivation of the **LSC approximation for a real-time quantum-mechanical correlation function** starting from its exact path-integral expression, outlined in section 1.1.3. The **application of the LSC approximation in the calculation of VER rate constant** is outlined step by step in subsections, 1.1.4, 1.1.5, 1.1.6. The general calculation of VER rate constant using the LT formula is discussed in subsection 1.1.4, followed by the application of the LSC approximation in the calculation of the VER rate constant using the LT formula, discussed in subsection 1.1.5. Finally, in subsection 1.1.6, an advanced version of the application of the LSC approximation in the calculation of systems with higher levels of complexity is discussed.

1.1.2 Path Integral Technique

The path integral formulation of quantum mechanics was introduced by R. P. Feynman in 1948(25). The two main formulations of path integration, imaginary time path integration and real-time path integration are introduced and discussed in the following two subsections.

- **Imaginary Time Path Integrals**

  The imaginary time path integral technique is an elegant and efficient method of calculating statistical mechanical properties of a many-body quantum mechanical system. In the following, we establish an exact mathematical relation between the partition function of a many-body quantum mechanical system and a corresponding fictitious classical system using path integral technique.

  To this end, let us consider a quantum system with a single particle with mass m, momentum p, and coordinate x, moving in a one dimensional potential $V(x)$, the partition function for this system is given as:

$$\begin{aligned} Q = Tr(e^{-\beta H}) &= \int dx_1 \left\langle x_1 | e^{-\beta H} | x_1 \right\rangle \\ = \int dx_1 \int dx_2 ... \int dx_P \left\langle x_1 | e^{-\epsilon H} | x_2 \right\rangle \left\langle x_2 | e^{-\epsilon H} | x_3 \right\rangle ... \left\langle x_P | e^{-\epsilon H} | x_1 \right\rangle &= \int dx_1 \int dx_2 ... \int dx_P \prod_{i=1}^{P} \left\langle x_i | e^{-\epsilon H} | x_{i+1} \right\rangle \end{aligned} \tag{1.3}$$

  where, $x_{P+1} = x_1$. It should be noted that in eq 1.3, the term $e^{-\beta H}$ has been divided into P terms in the following way

$$e^{-\beta H} = \left[e^{\frac{\beta}{P} H} \right]^P = \left[e^{\epsilon H} \right]^P \tag{1.4}$$

  where, $\beta/P = \epsilon$, followed by inserting $P - 1$ closures. In the next step, the

Hamiltonian for the system H is expanded into the kinetic and potential energy components, such that, for the ith term:

$$\begin{aligned}\left\langle x_i|e^{-\epsilon H}|x_{i+1}\right\rangle &= \left\langle x_i|e^{-\frac{\epsilon}{2}V(x)}e^{-\frac{\epsilon p^2}{2m}}e^{-\frac{\epsilon}{2}V(x)}|x_{i+1}\right\rangle \\ &= e^{-\frac{\epsilon}{2}V(x_i)}\left\langle x_i|e^{-\frac{\epsilon p^2}{2m}}|x_{i+1}\right\rangle e^{-\frac{\epsilon}{2}V(x_{i+1})}\end{aligned} \tag{1.5}$$

which leads to the following:

$$e^{-\frac{\epsilon}{2}[V(x_i)+V(x_{i+1})]}\left\langle x_i|e^{-\frac{\epsilon p^2}{2m}}|x_{i+1}\right\rangle \tag{1.6}$$

Further expansion of the term $\left\langle x_i|e^{-\frac{\epsilon p^2}{2m}}|x_{i+1}\right\rangle$ in eq 1.6 leads to the following:

$$\begin{aligned}\left\langle x_i|e^{-\frac{\epsilon p^2}{2m}}|x_{i+1}\right\rangle &= \int_{-\infty}^{\infty} dp\left\langle x_i|e^{-\frac{\epsilon p^2}{2m}}|p\right\rangle\langle p|x_{i+1}\rangle \\ = \int_{-\infty}^{\infty} dp e^{-\frac{\epsilon p^2}{2m}}\langle x_i|p\rangle\langle p|x_{i+1}\rangle &= \frac{1}{2\pi\hbar}\int_{-\infty}^{\infty} dp e^{-\frac{\epsilon p^2}{2m}}e^{\frac{i}{\hbar}px_i}e^{-\frac{i}{\hbar}px_{i+1}}\end{aligned} \tag{1.7}$$

It should be noted that the identity, $F(\hat{p})|p>=F(p)|p>$ is used to obtain the desired result in eq 1.7. Further simplification of eq 1.7 leads to the following expressions:

$$\begin{aligned}\left\langle x_i|e^{-\frac{\epsilon p^2}{2m}}|x_{i+1}\right\rangle &= \frac{1}{2\pi\hbar}\int_{-\infty}^{\infty} dp e^{-\frac{\epsilon p^2}{2m}}e^{\frac{i}{\hbar}p(x_i-x_{i+1})} = \frac{1}{2\pi\hbar}\int_{-\infty}^{\infty} dp e^{-\frac{\epsilon}{2m}\left(p^2-\frac{i}{\hbar}p(x_i-x_{i+1})\frac{2m}{-\epsilon}\right)} \\ = \frac{1}{2\pi\hbar}e^{-\frac{\epsilon}{2m}\frac{1}{\hbar^2}(x_i-x_{i+1})^2\frac{m^2}{\epsilon^2}}\sqrt{\frac{2m\pi}{\epsilon}} &= \sqrt{\frac{m}{2\pi\epsilon\hbar^2}}e^{-\frac{m(x_i-x_{i+1})^2}{2\epsilon\hbar^2}} = \sqrt{\frac{m\beta\omega_P^2}{2\pi}}e^{-\frac{m\beta\omega_P^2}{2}(x_i-x_{i+1})^2}\end{aligned} \tag{1.8}$$

It should be noted that the last step in eq 1.8 is obtained by considering $\omega_P^2 = P/(\beta\hbar)^2$ and $\beta/P = \epsilon$. Substituting eq 1.8 back into eq 1.3, we obtain the final result for the path integral representation of partition function for a one dimensional quantum system,

$$Q = \left(\frac{m\beta\omega_P^2}{2\pi}\right)^{P/2} \int dx_1 \int dx_2 ... \int dx_P e^{-\beta\left[\sum_{i=1}^{P} \frac{m\omega_P^2}{2}(x_i - x_{i+1})^2 + \frac{V(x_i)}{P}\right]} \tag{1.9}$$

Generalizing eq 1.9 to a three dimensional system, we obtain the following form for the partition function:

$$Q = \left(\frac{m\beta\omega_P^2}{2\pi}\right)^{3P/2} \int d\overrightarrow{r_1} \int d\overrightarrow{r_2} ... \int d\overrightarrow{r_P} e^{-\beta\left[\sum_{i=1}^{P} \frac{m\omega_P^2}{2}(\overrightarrow{r_i} - \overrightarrow{r}_{i+1})^2 + \frac{V(\overrightarrow{r_i})}{P}\right]} \tag{1.10}$$

Generalizing eq 1.10 to a many-body system, where the positions and momenta for the N number of particles are repressnted as $\overrightarrow{R} = (\overrightarrow{r}^{(1)}, \overrightarrow{r}^{(2)}, ..., \overrightarrow{r}^{(N)})$ and $\overrightarrow{P} = (\overrightarrow{p}^{(1)}, \overrightarrow{p}^{(2)}, ..., \overrightarrow{p}^{(N)})$, respectively, we obtain,

$$\begin{aligned} Q = \left\{\prod_{j=1}^{N} \left(\frac{m^{(j)}\beta\omega_P^2}{2\pi}\right)^{3P/2}\right\} \int d\overrightarrow{R_1} \int d\overrightarrow{R_2} ... \int d\overrightarrow{R_P} \\ exp\left[-\frac{\beta}{P}\left(V(\overrightarrow{R_1}) + ... + V(\overrightarrow{R_P})\right) - \sum_{i=1}^{P} \frac{m^{(j)}\omega_P^2}{2}\left(\overrightarrow{r_i}^{(j)} - \overrightarrow{r}_{i+1}^{(j)}\right)^2\right] \end{aligned} \tag{1.11}$$

The quantum partition function in eq 1.11 is isomorphic to the configurational partition function for a fictitious classical system, where every quantum particle is represented by a necklace of P beads, where each bead is linked to other beads in the necklace with a harmonic potential with frequency ω_P, and every

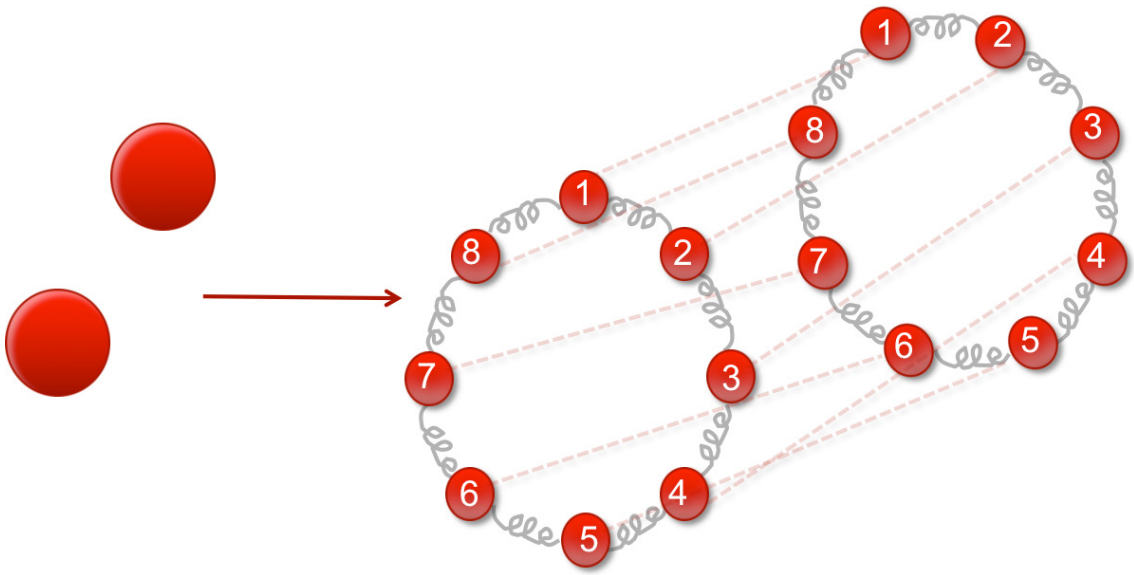

Figure 1.3: Schematic Representation of the Imaginary Time Path Integral Technique. The system in the left side of arrow corresponds to the quantum-mechanical system, and the system in the right side of arrow corresponds to the fictitious classical system. The classical system results from the path integral formulation applied to the quantum system and has a partition function that is isomorphic with the quantum system.

ith bead in a necklace feels an external potential, $V(x)$, from the *ith* bead $(where, 1 < i < P)$ of every other necklace.

The importance of the path integral technique comes from the fact that, because of the isomorphism between the configurational partition functions of the quantum and the fictitious classical systems, the exact calculation of the quantum partition function and any thermodynamic property that is derivable from the partition function is now possible to be calculated using classical simulations. A pictorial representation of the path integral technique is given in figure 1.3.

- **Real Time Path Integrals**

The real time path integral formulation of quantum mechanics aims at describing dynamical quantities of many-body quantum mechanical systems. The underlying idea is to represent the quantum propagator as a sum over all possible paths between the initial and final time points. Since, in this research, real time path integral method has been employed to the calculation of two time quantum mechanical correlation functions, the real time path integral formulation of a quantum mechanical two-time correlation function is outlined in this subsection. To this end, consider a quantum mechanical two time correlation function:

$$C_{AB}(t) = Tr\left(Ae^{iHt/\hbar}Be^{-iHt/\hbar}\right) = \int dx_0^+ \left\langle x_0^+|Ae^{iHt/\hbar}Be^{-iHt/\hbar}|x_0^+\right\rangle$$
$$= \int dx_0^+ \int dx_0^- \int dx_N^+ \int dx_N^- \left\langle x_0^+|A|x_0^-\right\rangle \left\langle x_0^-|e^{iHt/\hbar}|x_N^-\right\rangle \left\langle x_N^-|B|x_N^+\right\rangle \left\langle x_N^+|e^{-iHt/\hbar}|x_0^+\right\rangle \tag{1.12}$$

It should be noted that, in eq 1.12 four closure relations are insterted. In the next step, we derive expressions for the propagators $\left\langle x_0^-|e^{iHt/\hbar}|x_N^-\right\rangle$, and $\left\langle x_N^+|e^{-iHt/\hbar}|x_0^+\right\rangle$. Assuming $\lambda = it/\hbar$, we get $e^{-iHt/\hbar} = \left(e^{-\lambda H/N}\right)^N$, such that,

$$\begin{aligned}\left\langle x_N^+|e^{-iHt/\hbar}|x_0^+\right\rangle = \left\langle x_N^+|\left(e^{-\lambda H/N}\right)^N|x_0^+\right\rangle = \int dx_{N-1}^+ \int dx_{N-2}^+ ... \int dx_1^+ \\ \left\langle x_N^+|e^{-\lambda H/N}|x_{N-1}^+\right\rangle \left\langle x_{N-1}^+|e^{-\lambda H/N}|x_{N-2}^+\right\rangle ... \left\langle x_1^+|e^{-\lambda H/N}|x_0^+\right\rangle \\ = \int dx_{N-1}^+ \int dx_{N-2}^+ ... \int dx_1^+ \prod_{i=0}^{N-1} \left\langle x_{i+1}^+|e^{-\lambda H/N}|x_i^+\right\rangle\end{aligned} \tag{1.13}$$

In this step, the integral $\int dx_{N-1}^+ \int dx_{N-2}^+ ... \int dx_1^+$ represents the sum over all paths from x_0^+ to x_{N-1}^+. Essentially, every continuous time-path has been approximated by broken-line path assuming the intervals (λ/N) are infinitesimally small. In the next step, we consider the term $\left\langle x_{i+1}^+|e^{-\lambda H/N}|x_i^+\right\rangle$ in eq 1.13,

$$\begin{aligned}\left\langle x_{i+1}^+|e^{-\lambda H/N}|x_i^+\right\rangle &= \left\langle x_{i+1}^+|e^{-\frac{\lambda}{N}\frac{V(x)}{2}} e^{-\frac{\lambda}{N}\frac{p^2}{2m}} e^{-\frac{\lambda}{N}\frac{V(x)}{2}}|x_i^+\right\rangle \\ &= e^{-\frac{\lambda}{N}\frac{1}{2}[V(x_{i+1})+V(x_i)]} \left\langle x_{i+1}^+|e^{-\frac{\lambda}{N}\frac{p^2}{2m}}|x_i^+\right\rangle\end{aligned} \tag{1.14}$$

Considering the term $\left\langle x_{i+1}^+|e^{-\frac{\lambda}{N}\frac{p^2}{2m}}|x_i^+\right\rangle$ in eq 1.14,

$$\begin{aligned}\left\langle x_{i+1}^+|e^{-\frac{\lambda}{N}\frac{p^2}{2m}}|x_i^+\right\rangle &= \int_{-\infty}^{\infty} dp \left\langle x_{i+1}^+|e^{-\frac{\lambda}{N}\frac{p^2}{2m}}|p\right\rangle \left\langle p|x_i^+\right\rangle = \int_{-\infty}^{\infty} dp e^{-\frac{\lambda}{N}\frac{p^2}{2m}} \left\langle x_{i+1}^+|p\right\rangle \left\langle p|x_i^+\right\rangle \\ &= \frac{1}{2\pi\hbar} \int_{-\infty}^{\infty} dp e^{-\frac{\lambda}{N}\frac{p^2}{2m}} e^{-\frac{i}{\hbar}px_i} e^{\frac{i}{\hbar}px_{i+1}} = \frac{1}{2\pi\hbar} \int_{-\infty}^{\infty} dp e^{-\frac{\lambda}{N}\frac{p^2}{2m}} e^{\frac{i}{\hbar}p(x_{i+1}-x_i)} \\ &= \sqrt{\frac{mN}{2\pi\hbar^2\lambda}} e^{-\frac{mN}{2\lambda\hbar^2}(x_{i+1}-x_i)^2}\end{aligned} \tag{1.15}$$

Substituting eq 1.15 back to eq 1.13, we obtain the following expression,

$$\left\langle x_N^+|e^{-\frac{i}{\hbar}Ht}|x_0^+\right\rangle = \int dx_{N-1}^+ \int dx_{N-2}^+ ... \int dx_1^+ \prod_{i=0}^{N-1} \left\langle x_{i+1}^+|e^{-\frac{\lambda}{N}H}|x_i^+\right\rangle$$

$$= \int dx_{N-1}^+ \int dx_{N-2}^+ ... \int dx_1^+ \prod_{i=0}^{N-1} \sqrt{\frac{mN}{2\pi\hbar^2\lambda}} e^{-\frac{\lambda}{N}\frac{1}{2}[V(x_{i+1})+V(x_i)]} e^{-\frac{mN}{2\lambda\hbar^2}(x_{i+1}-x_i)^2} \tag{1.16}$$

Further simplification of eq 1.16 using the identity $\lambda/N = it/\hbar N = i\epsilon/\hbar$ we obtain the following expression:

$$\begin{aligned}\left\langle x_N^+|e^{-\frac{i}{\hbar}Ht}|x_0^+\right\rangle &= \left(\frac{mN}{2\pi\hbar^2\lambda}\right)^{\frac{N}{2}} \int dx_{N-1}^+ \int dx_{N-2}^+ ... \int dx_1^+ \\ &\quad e^{-\sum_{i=0}^{N-1}\left[\frac{\lambda}{N}\frac{1}{2}[V(x_{i+1})+V(x_i)]+\frac{mN}{2\lambda\hbar^2}(x_{i+1}-x_i)^2\right]} \\ &= \left(\frac{m}{2\pi i\hbar\epsilon}\right)^{\frac{N}{2}} \int dx_{N-1}^+ \int dx_{N-2}^+ ... \int dx_1^+ \\ &\quad e^{-\sum_{i=0}^{N-1}\left[\frac{i}{\hbar}\frac{\epsilon}{2}[V(x_{i+1})+V(x_i)]+\frac{m}{2i\hbar\epsilon}(x_{i+1}-x_i)^2\right]} \\ &= \left(\frac{m}{2\pi i\hbar\epsilon}\right)^{\frac{N}{2}} \int dx_{N-1}^+ \int dx_{N-2}^+ ... \int dx_1^+ \\ &\quad e^{\frac{i}{\hbar}\epsilon\sum_{i=0}^{N-1}\left[\frac{m}{2}\left(\frac{x_{i+1}-x_i}{\epsilon}\right)^2-\frac{V(x_{i+1})+V(x_i)}{2}\right]}\end{aligned} \tag{1.17}$$

In the next step, we define the forward action as follows:

$$S\left(x_0^+, ..., x_N^+\right) = \epsilon \sum_{i=0}^{N-1} \left[\frac{m}{2}\left(\frac{x_{i+1}-x_i}{\epsilon}\right)^2 - \frac{V(x_{i+1})+V(x_i)}{2}\right]$$

$$= \epsilon \sum_{i=0}^{N-1} \left[\frac{m}{2}\left(\frac{x_{i+1}-x_i}{\epsilon}\right)^2\right] - \left[\frac{1}{2}V(x_0^+) + V(x_1^+) + ... + V(x_{N-1}^+) + \frac{1}{2}V(x_N^+)\right]$$

$$= S_{kin} + S_{pot} \tag{1.18}$$

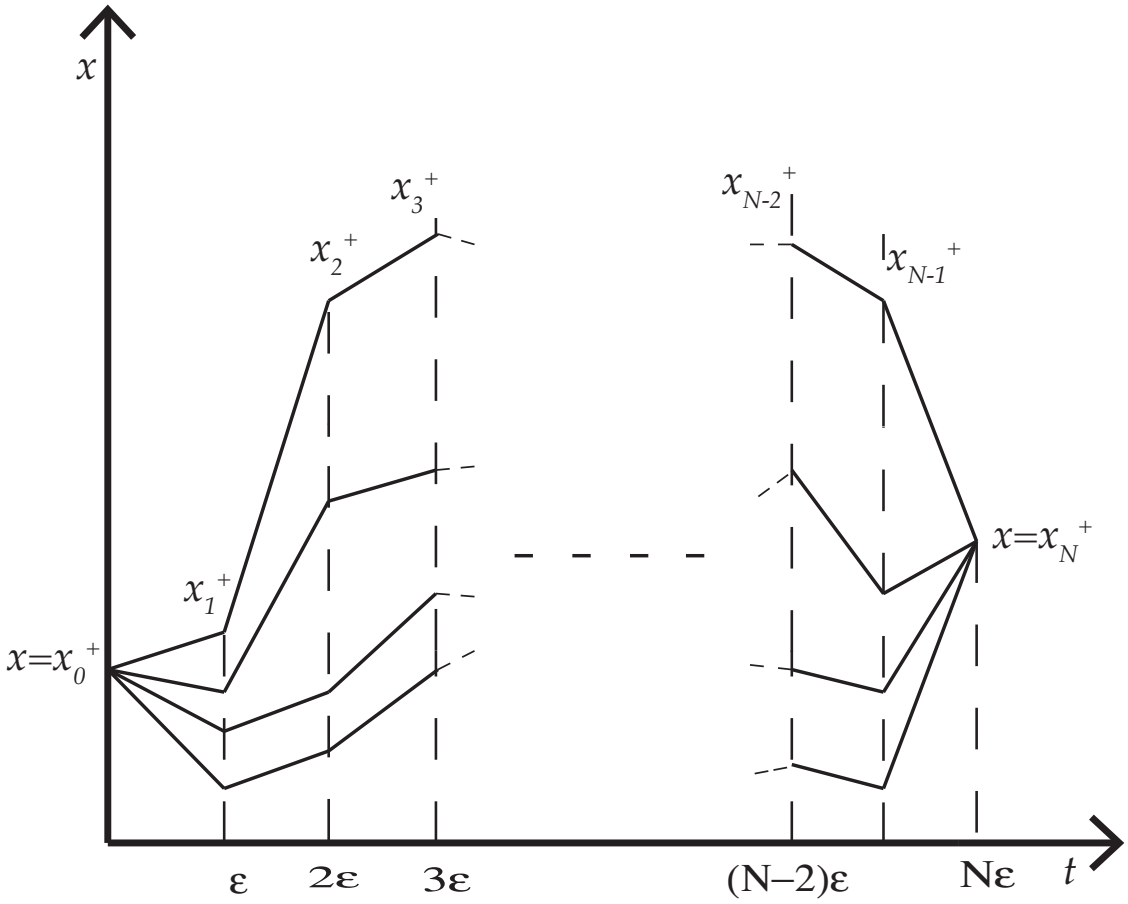

Figure 1.4: Schematic Representation of Real Time Path Integration Method. The line paths represent the time evolution for the quantum propagator $\left\langle x_N^+ | e^{-iHt/\hbar} | x_0^+ \right\rangle$ divided in N parts, where $\epsilon = t/N$.

Substituting eq 1.18 back to eq 1.17 we obtain

$$\left\langle x_N^+|e^{-\frac{i}{\hbar}Ht}|x_0^+\right\rangle = \left(\frac{m}{2\pi i\hbar\epsilon}\right)^{\frac{N}{2}} \int dx_{N-1}^+ \int dx_{N-2}^+ ... \int dx_1^+ e^{\frac{i}{\hbar}S(x_0^+,...,x_N^+)} \quad (1.19)$$

Going over the same derivation for the other propagator in eq 1.12, $\left\langle x_0^-|e^{iHt/\hbar}|x_N^-\right\rangle$, we obtain a similar equation as eq 1.19:

$$\left\langle x_0^-|e^{\frac{i}{\hbar}Ht}|x_N^-\right\rangle = \left(\frac{im}{2\pi\hbar\epsilon}\right)^{\frac{N}{2}} \int dx_{N-1}^- \int dx_{N-2}^- ... \int dx_1^- e^{-\frac{i}{\hbar}S(x_0^-,...,x_N^-)} \quad (1.20)$$

In the final step, the time propagators, eq 1.19 and eq 1.20, are substituted back to the expression for the correlation function in eq 1.12,

$$\begin{aligned} C_{AB}(t) = \left(\frac{m}{2\pi\hbar\epsilon}\right)^N \int dx_0^+ ... \int dx_N^+ \int dx_0^- ... \int dx_N^- \\ \left\langle x_0^+|A|x_0^-\right\rangle \left\langle x_N^-|B|x_N^+\right\rangle e^{\frac{i}{\hbar}\left[S(x_0^+,...,x_N^+)-S(x_0^-,...,x_N^-)\right]}. \end{aligned} \quad (1.21)$$

Eq 1.21 is the final form of the real time path integral representation of the two-time quantum-mechanical correlation function. The essence of the real-time path integral technique is to divide the time evolution of the quantum propagater over all possible paths (the number of possible paths is infinity, such that, the exact quantum-mechanical correlation function is obtained at the limit of $N \to \infty$).

The underlying idea is the quantum mechanical rule for combining amplitudes, according to which, if the time evolution of the propagators can occur in a number of possible ways, the amplitudes for each of the possible paths can be

added. As a result, in real time path integral method, the time propagation through all possible paths is considered and the corresponding amplitudes are integrated over all possible intermediate positions. The method is, in concept, similar to Young's double slit experiment, where the amplitudes for passing through the slits interfere constructively and destructively. Figure 1.4 shows a schematic representation of the real time path integral method, where the line paths represent the time evolution for the quantum propagator $\left\langle x_N^+ | e^{-iHt/\hbar} | x_0^+ \right\rangle$ divided in N parts.

- **Path Integral Molecular Dynamics**

  Using AMBER software package imaginary time path integral molecular dynamics (PIMD) simulations can be performed for many-body systems. There are two versions of PIMD available in AMBER,

  - *Primitive approximation (PRIMPIMD)* -In this approach, the PIMD is performed following eq 1.11, where using the potential and kinetic terms as components of the Hamiltonian, classical molecular dynamics (MD) simulations are performed for the fictitious classical system with P beads where the fictitious mass of each bead is chosen as $\mu_i = m/P$, where m is the particle mass.
  - *Normal mode PIMD (NMPIMD)* - In this implementation, the normal mode transformation is used to uncouple the harmonic term in eq 1.11, prior to using the potential and kinetic terms as components of the Hamiltonian, following which classical molecular dynamics (MD) simulations are performed for the fictitious classical system with P beads where the fictitious mass of each bead is chosen as $\mu_i = m/P$, where m is the particle mass.

1.1.3 Linearized Semiclassical Approximation-Inital Value Representation

In this subsection, the derivation of the LSC approximation for a real-time quantum-mechanical two-time correlation function from its exact path integral expression(122) is outlined.

We begin by considering a general quantum-mechanical two-time correlation function

$$C_{AB}(t) = Tr(\hat{A}e^{i\hat{H}t/\hbar}\hat{B}e^{-i\hat{H}t/\hbar}) \tag{1.22}$$

$C_{AB}(t)$ can also be expressed in terms of a real-time path integral given below in terms of the discrete time, $0, \epsilon, 2\epsilon, ..., N, \epsilon = t$, (refer to eq 1.12 and eq 1.21)

$$\begin{aligned} C_{AB}(t) = \int dx_0^+ \int dx_0^- \int dx_N^+ \int dx_N^- < x_0^+|\hat{A}|x_0^- > \\ \times < x_0^-|e^{i\hat{H}t/\hbar}|x_N^- >< x_N^-|\hat{B}|x_N^+ >< x_N^+|e^{-i\hat{H}t/\hbar}|x_0^+ > \\ = \Big(\frac{m}{2\pi\hbar\epsilon}\Big)^N \int dx_0^+ ... \int dx_N^+ ... \int dx_0^- ... \\ \times \int dx_N^- < x_0^+|\hat{A}|x_0^- >< x_N^-|\hat{B}|x_N^+ > e^{i(S_N^+ - S_N^-)/\hbar} \end{aligned} \tag{1.23}$$

The forward and backward actions are given by

$$S_N^{\pm} = \sum_{j=0}^{N-1} \epsilon \left[\frac{1}{2} m \left(\frac{x_{j+1}^{\pm} - x_j^{\pm}}{\epsilon} \right)^2 - V(x_j^{\pm}) \right], \tag{1.24}$$

where $\epsilon = t/N$. The evaluation of eq 1.23 is difficult to converge due to sign problem resulting from the presence of the oscillatory terms in the integral . One of the methods to overcome this issue is the linearization approximation, which amounts to the expansion of the forward-backward action, $S_N^+ - S_N^-$, to first order in the difference between the forward and backward trajectories, $z_0 - z_N$, such that,

$$y_j = \frac{1}{2}(x_j^+ + x_j^-), z_j = x_j^+ - x_j^-. \tag{1.25}$$

This yields:

$$\begin{aligned} S_N^+ - S_N^- &\approx \epsilon \sum_{j=0}^{N-1} \left[\frac{m}{\epsilon^2}(y_{j+1} - y_j)(z_{j+1} - z_j) - V'(y_j) z_j \right] \\ &= \epsilon \sum_{j=1}^{N-1} z_j \left[\frac{m}{\epsilon^2}(2y_j - y_{j-1} - y_{j+1}) - V'(y_j) \right] \\ &\quad + \epsilon z_0 \left[-\frac{m}{\epsilon^2}(y_1 - y_0) - V'(y_0) \right] \\ &\quad + \epsilon z_N \frac{m}{\epsilon^2}(y_N - y_{N-1}) \end{aligned} \tag{1.26}$$

The physical interpretation of the linearization approximation can be understood by considering that the forward-backward trajectory pairs that are farther in the phase space have smaller contribution towards the integral due to cancellation of the highly oscillatory terms. As a result, only the trajectory pairs closer to each other have major contribution towards the integral. Following the linearization, the integration over the difference variables, $z_1, ..., z_{N-1}$, can be performed explicitely, using the following identity:

$$\begin{aligned} &\int dz_j e^{(-i/\hbar)\epsilon[m/\epsilon^2(y_{j+1} - 2y_j + y_{j-1}) + V'(y_j)]z_j} \\ &\quad = \frac{2\pi\hbar}{\epsilon} \delta \left[\frac{m}{\epsilon^2}(y_{j+1} - 2y_j + y_{j-1}) \right] \end{aligned} \tag{1.27}$$

It should also be noted that in the limit $N \to \infty (\epsilon \to 0)$,

$$\epsilon z_0 \left[-\frac{m}{\epsilon^2}(y_1 - y_0) - V'(y_0) \right] \to -z_0 p_0,$$
$$\epsilon z_N \frac{m}{\epsilon^2}(y_N - y_{N-1}) \to z_N p_N, \tag{1.28}$$

where $p_0/m = \lim_{\epsilon\to 0}(y_1 - y_0)/\epsilon$ and $p_N/m = \lim_{\epsilon\to 0}(y_N - y_{N-1})/\epsilon$. Changing the integration variables $y_1, ..., y_{N-1}$ into $f_1, ..., f_{N-1}$, such that

$$f_j = \frac{m}{\epsilon^2}(y_{j+1} - 2y_j + y_{j-1}) + V'(y_j), \tag{1.29}$$

and explicitely integrating over $f_1, ..., f_{N-1}$, then leads to the following approximation:

$$C_{AB}(t) \approx \frac{1}{2\pi\hbar} \int dy_0 \int dy_t \int dz_0 \int dz_t \left| \frac{\partial p_0}{\partial y_t} \right|$$
$$\times \left\langle y_0 + z_0/2 \left| \hat{A} \right| y_0 - z_0/2 \right\rangle \times \left\langle y_t + z_t/2 \left| \hat{B} \right| y_t - z_t/2 \right\rangle e^{-ip_0 z_0/\hbar} e^{ip_t z_t/\hbar} \tag{1.30}$$

It should be noted that in arriving to eq 1.30, we have explicitely incorporated the limit $N \to \infty$ ($\epsilon \to 0$), such that $y_N \to y_t$ and $z_N \to z_t$, and made use of the following identity

$$\lim_{N\to\infty} \frac{1}{\epsilon} \left(\frac{m}{\epsilon^2} \right)^{N-1} \left| \frac{\partial y}{\partial f} \right| = \frac{1}{m} \left| \frac{\partial p_0}{\partial y_t} \right| \tag{1.31}$$

($|\partial y/\partial f|$ is the determinant of the $(N-1)\times(N-1)$ matrix whose (i,j)th element is $\partial y_i/\partial f_i$). It should also be noted that $y_t = y_t(y_0, p_0)$ in eq 1.30 follows a classical trajectory [cf. eq 1.27]:

$$
\begin{aligned}
f_j = \frac{m}{\epsilon^2}(y_{j+1} - 2y_j + y_{j-1}) + V'(y_j) = 0 \\
\xrightarrow{N\to\infty} m\frac{d^2}{dt^2}y(t) = -V'\left[y(t)\right]
\end{aligned}
\tag{1.32}
$$

Finally, changing the integration variable y_t into p_0, which amounts to a transformation to the initial value representation, and using the Wigner transform given below:

$$
A_W(x,p) = \int d\Delta e^{-ip\Delta/\hbar} \left\langle x + \Delta/2 \left| \hat{A} \right| x - \Delta/2 \right\rangle, \tag{1.33}
$$

The resulting LSC approximation for the correlation function $C_{AB}(t)$ is given as:

$$
C_{AB}(t) \approx (2\pi\hbar)^{-1} \int dy_0 \int dp_0 A_W(y_0,p_0) B_W(y_t,p_t), \tag{1.34}
$$

where $y_t = y_t(y_0,p_0)$ and $p_t = p_t(y_0,p_0)$ follow classical trajectory.

Some of the key points that should be noted about the LSC approximation are listed below:

1. The LSC approximation can also be derived by linearizing the forward-backward action in the *semiclassical* initial-value representation expression for a real-time quantum-mechanical correlation function, with respect to the difference between the forward and backward trajectories(124; 23; 28; 29; 30; 31; 32; 33; 34; 35). However, the LSC approximation presented here, as derived by Geva and coworkers(87; 62; 86; 76; 54; 56), is obtained by linearizing the forward-backward action in the exact real time path integral expression for a quantum-mechanical correlation function, without explicitly invoking the semiclassical stationary phase approximation(23). However, conceptually a semiclassical method is one that strives to connect the purely classical and exact quantum mechanical description for a particular quantity or process of interest. It should also be noted

that, classically the time evolution of the correlation function is dictated by the path with the minimum action, while the exact quantum-mechanical description corresponds to summing over the amplitudes of an infinite number of paths. The LSC approximation minimizes the number of paths by applying the linearization approximation (refer eq 1.25) resulting in a semiclassical method that is feasible for complex systems such as molecular liquids.

2. Apart from the elegant and straightforward derivation, the LSC approximation is exact (1) at initial time, (2) at the classical limit, and (3) for harmonic systems.

3. The main disadvantage of the LSC approximation is that it can only capture quantum dynamical effects that arise from the short time interferences between the various trajectories. However, in case of high-frequency VER in condensed phase, the relaxation is primarily dominated by short-time dynamics of the correlation functions.

4. Although, one of the major advantages of the LSC approximation is the computational feasibility in calculating the quantum dynamical properties in many-body anharmonic systems, the computation of the Wigner transform in such cases is non-trivial. However, various computational schemes have been devised by Geva and co-workers for successful implementation of the LSC approximation for systems with many DOF, these are discussed in the following subsections.

In the following subsections, the application of the LSC approximation in the calculation of VER rate constant is discussed, followed by the various *computational schemes* devised for the implementation of the approximation in a variety of condensed phase systems.

1.1.4 Landau Teller Formula

In this subsection the Landau Teller (LT) formula for the calculation of VER is outlined. The derivation of the LT formula is based on a perturbative approach and is aimed at the calculation of VER rate constant in high-frequency vibrational modes. We begin by considering a general quantum mechanical Hamiltonian with a harmonic vibrational mode coupled to a bath of accepting modes:

$$\hat{H} = \hat{H}_s + \hat{H}_b + \hat{H}_{bs} \equiv \hat{H}_0 + \hat{H}_{bs} \tag{1.35}$$

where

$$\hat{H}_s = \frac{\hat{p}^2}{2\mu} + \frac{1}{2}\mu\omega^2\hat{q}^2 \tag{1.36}$$

is the Hamiltonian of the vibrational mode being probed ($\hat{q}, \hat{p}, \mu$, and ω are the corresponding coordinate, momentum, reduced mass and frequency, respectively)

$$\hat{H}_b = \sum_{i=1}^{N} \frac{\left(\hat{P}^{(i)}\right)^2}{2M^{(i)}} + \hat{V}\left(\hat{Q}^{(1)}, ..., \hat{Q}^{(N)}\right) = \sum_{i=1}^{N} \frac{\left(\hat{P}^{(i)}\right)^2}{2M^{(i)}} + \hat{V}\left(\hat{\boldsymbol{Q}}\right) \tag{1.37}$$

is the Hamiltonian of the bath, which consists of the other intermolecular and intramolecular DOF. $\hat{\boldsymbol{Q}} = \left(\hat{Q}^{(1)}, ..., \hat{Q}^{(N)}\right), \hat{\boldsymbol{P}} = \left(\hat{P}^{(1)}, ..., \hat{P}^{(N)}\right), \{M^{(i)}\}$, and $\hat{V}\left(\hat{\boldsymbol{Q}}\right) = \left(\hat{Q}^{(1)}, ..., \hat{Q}^{(N)}\right)$ are the corresponding coordinates, momenta, masses, and potential energy, respectively, and

$$\hat{H}_{bs} = -\hat{q}\hat{F}\left(\hat{Q}^{(1)}, ..., \hat{Q}^{(N)}\right) = -\hat{q}\hat{F}\left(\hat{\boldsymbol{Q}}\right) \tag{1.38}$$

is the system-bath coupling term that is assumed to be linearized in the vibrational coordinate, $\hat{q}$, such that VER takes place via the emission of one vibrational quantum.

It is also assumed that the force on the vibrational mode, $\hat{F}\left(\hat{\boldsymbol{Q}}\right)$, is only dependent on the bath coordinates and does not depend on momentum terms. The underlying idea is to expand $\hat{V}\left(\hat{\boldsymbol{Q}},\hat{q}\right)$ to first order in $\hat{q}$ around equilibrium vibrational mode coordinate, $\hat{q}_0$, such that,

$$\hat{V}\left(\hat{\boldsymbol{Q}},\hat{q}\right)=\hat{V}|_{\hat{q}=0}\left(\hat{\boldsymbol{Q}}\right)+\left[\frac{\partial\hat{V}}{\partial\hat{q}}\right]_{\hat{q}=0}\hat{q}=\hat{V}\left(\hat{\boldsymbol{Q}}\right)+\hat{q}\hat{F}\left(\hat{\boldsymbol{Q}}\right) \tag{1.39}$$

It is a reasonable approximation in case of *weak system bath coupling* where the displacement of the vibrational mode relative to the equilibrium configuration is assumed to be small so as to cause negligible perturbation on the environment.

Given the general Hamiltonian above, the LT formula is based on the Redfield theory limit of the generalized quantum master equation. To this end, along with the *weak system-bath coupling*, two more fundamental assumptions are considered: (1) *separation of time scales*, the VER lifetime is assumed to be much longer than the correlation time of the bath-induced force; (2) the *rotating wave approximation*, resulting in the removal of highly oscillating terms and decoupling of population relaxation and phase relaxation. Under these conditions, the following equation for the vibrational populations can be obtained(87):

$$\frac{d}{dt}P_n=k_{n\leftarrow n+1}P_{n+1}+k_{n\leftarrow n-1}P_{n-1}-\left(k_{n+1\leftarrow n}+k_{n-1\leftarrow n}\right)P_n \tag{1.40}$$

Where,

$$k_{n\leftarrow n+1}=e^{\beta\hbar\omega}k_{n+1\leftarrow n}=\frac{n+1}{\beta\hbar\omega}\frac{\beta}{2\mu}\tilde{C}(\omega) \tag{1.41}$$

Here, $\beta=(k_BT)^{-1}$, and

$$\tilde{C}(\omega)=\int_{-\infty}^{\infty}dte^{i\omega t}C(t) \tag{1.42}$$

is the Fourier transform (FT) of the force-force correlation function (FFCF) of the force induced by the bath on the vibrational mode.

$$C(t) = \langle \delta\hat{F}_0(t)\delta\hat{F}\rangle_0 \tag{1.43}$$

where $\langle\hat{A}_0 = Tr[e^{-\beta\hat{H}_b}\hat{A}]/Z_b$, $Z_b = Tr[e^{-\beta\hat{H}_b}]$, $\delta\hat{F} = \hat{F} - \langle\hat{F}\rangle_0$ and

$$\delta\hat{F}_0 = e^{i\hat{H}_b t/\hbar}\delta\hat{F}e^{-i\hat{H}_b t/\hbar} \tag{1.44}$$

The population dynamics in eq 1.40 results in an exponential decay in the vibrational energy, such that:

$$\frac{d}{dt}\langle\delta\hat{H}_s\rangle = \sum_{n=0}^{\infty}(n+1/2)\hbar\omega\frac{d}{dt}P_n = -\frac{1}{T_1}\langle\delta\hat{H}_s\rangle \tag{1.45}$$

Here $\delta\hat{H}_s = \hat{H}_s - \langle\hat{H}_s\rangle_0$, and $\langle\hat{H}_s\rangle_0 = \hbar\omega/2 + \hbar\omega/(e^{\beta\hbar\omega} - 1)$ is the vibrational energy at thermal equilibrium. The VER rate constant, given as $1/T_1$ in eq 1.45 is given by the LT formula:

$$\frac{1}{T_1} = \frac{1 - e^{-\beta\hbar\omega}}{\beta\hbar\omega}\frac{\beta}{2\mu}\tilde{C}(\omega) \tag{1.46}$$

For a more detailed discussion on the LT formula, the reader is directed to ref (87). When considering only $0 \leftarrow 1$ vibrational relaxation, the rate constant for population relaxation is to the same effect as the rate constant for energy relaxation. Considering the equation for rate constant given in eq 1.41 for the $0 \leftarrow 1$ vibrational relaxation, we get

$$k_{10} = \frac{1}{2\mu\hbar\omega_{10}}\tilde{C}\left(\omega_{10}\right) \tag{1.47}$$

As mentioned in the earlier section, calculation of the exact quantum-mechanical correlation function, $\tilde{C}(\omega)$, for a vibrational mode with high vibrational transition

frequency, ($\beta\hbar\omega \gg 1$), in condensed phase is extremely difficult. There exists a number of theoretical schemes based on semicalssical and mixed-quantum classical methods, that are devised for the approximate calculations of the quantum mechanical correlation functions in many-body anharmonic systems. However, a highly popular simplification of the VER rate constant calculation using the LT formula is the use of a quantum correction factor (QCF)(90; 99; 39; 60; 100; 67; 101; 102; 103; 104; 105; 106; 107; 108; 88; 109; 110) multiplied to the classical limit of the LT formula

$$k_{10} = Q\left(\omega_{10}\right) \frac{1}{2\mu\hbar\omega_{10}} \tilde{C}_{Cl}\left(\omega_{10}\right) \tag{1.48}$$

where, $Q\left(\omega_{10}\right)$ is the QCF evaluated at the vibrational transition frequency of the excited vibrational mode. In general, QCFs are obtained by imposing certain features of the quatum-mechanical correlation functions. Although, there are numerous systems for which the VER rate constant calculations have been performed using QCFs resulting in VER rate constants with reasonable experimental agreement, the use of QCFs for the calculation of VER rate constant for a high energy vibrational mode, where $\beta\hbar\omega \gg 1$, is in general *ad hoc* and often a fair amount of experimentation needs to be employed in order to find the suitable QCF for the relaxation mechanism exhibited by the system of interest.

1.1.5 Vibrational Energy Relaxation Rate Constant using LSC Approximation

In this subsection, the application of the LSC approximation in the calculation of VER rate constant in condensed phase using the LT formula (discussed in subsection 1.1.4) is outlined.(87) To this end, we consider the LSC approximation, given in eq 1.1, of the quantum-mechanical FFCF, given in eq 1.43, which assumes the following form:

$$C(t) \approx \frac{1}{Z_b}\frac{1}{(2\pi\hbar)^N}\int d\boldsymbol{Q}_0 \int d\boldsymbol{P}_0 [\delta\hat{F}e^{-\beta\hat{H}_b}]_W(\boldsymbol{Q}_0,\boldsymbol{P}_0)\delta F_W(\boldsymbol{Q}_t^{(Cl)},\boldsymbol{P}_t^{(Cl)}) \tag{1.49}$$

Here

$$\delta F_W(\boldsymbol{Q}_t^{(Cl)},\boldsymbol{P}_t^{(Cl)}) = \delta F_W(\boldsymbol{Q}_t^{(Cl)}) \tag{1.50}$$

and

$$\begin{aligned}[\delta\hat{F}e^{-\beta\hat{H}_b}]_W(\boldsymbol{Q}_0,\boldsymbol{P}_0) = \int d\Delta e^{-iP_0\Delta/\hbar}\times \\ \left\langle \boldsymbol{Q}_0+\Delta/2|e^{-\beta\hat{H}_b}|\boldsymbol{Q}_0-\Delta/2\right\rangle \delta F(\boldsymbol{Q}_0+\Delta/2)\end{aligned} \tag{1.51}$$

The oscillatory phase factor, $e^{-iP_0\Delta/\hbar}$, in the integrand in eq 1.51 makes the direct calculation of the correlation function in eq 1.49 extremely difficult due to sign problem. In order to overcome this problem, a local harmonic approximation (LHA) is applied that allows the integrand in eq 1.51 to be solved analytically. The LHA is employed by considering the quadratic expansion of the potential energy of the bath, $V(Q)$, around an arbitrary point $\boldsymbol{Q} = \boldsymbol{Q}_0$:

$$\begin{aligned}V(\boldsymbol{Q}) \approx V(\boldsymbol{Q}_0) + \sum_{k=1}^{N}\frac{\partial V}{\partial Q^{(k)}}|_{\boldsymbol{Q}=\boldsymbol{Q}_0}[Q^{(k)}-Q_0^{(k)}]+ \\ \frac{1}{2}\sum_{k=1}^{N}\sum_{l=1}^{N}\frac{\partial^2 V}{\partial Q^{(k)}\partial Q^{(l)}}|_{\boldsymbol{Q}=\boldsymbol{Q}_0}[Q^{(k)}-Q_0^{(k)}][Q^{(l)}-Q_0^{(l)}]\end{aligned} \tag{1.52}$$

The quadratic term in eq. 1.52 is next written in terms of mass-weighted coordinates, $\{\sqrt{M^{(k)}[Q^{(k)}-Q_0^{(k)}]}\}$, and Hessian matrix elements

$$\mathscr{H}_{k,l} = \frac{1}{\sqrt{M^{(k)}M^{(l)}}} \frac{\partial^2 V}{\partial Q^{(k)} \partial Q^{(l)}} |_{\boldsymbol{Q}=\boldsymbol{Q}_0} \tag{1.53}$$

followed by a transformation to the normal mode representation:

$$\begin{aligned} \frac{1}{2}\sum_{k=1}^{N}\sum_{l=1}^{N} \frac{\partial^2 V}{\partial Q^{(k)} \partial Q^{(l)}} |_{\boldsymbol{Q}=\boldsymbol{Q}_0} [Q^{(k)} - Q_0^{(k)}][Q^{(l)} - Q_0^{(l)}] = \\ \frac{1}{2}\sum_{k=1}^{N}\sum_{l=1}^{N} \mathscr{H}_{k,l} \left(\sqrt{M^{(k)}}[Q^{(k)} - Q_0^{(k)}] \sqrt{M^{(l)}}[Q^{(l)} - Q_0^{(l)}] \right) = \\ \frac{1}{2}\sum_{k=1}^{N} (\Omega^{(k)})^2 [Q_n^{(k)}]^2 \end{aligned} \tag{1.54}$$

In eq 1.54

$$Q_n^{(k)} = \sum_{k=1}^{N} T_{l,k} \sqrt{M^{(l)}} [Q^{(l)} - Q_0^{(l)}] \tag{1.55}$$

are the mass-weighted normal mode coordinates and $\{(\Omega^{(k)})^2\}$ are the eigenvalues of the Hessian matrix, $\mathscr{H}_{k,l}$. Employing the LHA amounts to rewriting the linear term in eq 1.52 and the kinetic energy of the bath in terms of the normal mode coordinates and momenta. The resulting equation gives the LHA of the quantum-mechanical bath Hamiltonian around $\boldsymbol{Q} - \boldsymbol{Q}_0$:

$$\hat{H}_b \approx \sum_{k=1}^{N} \frac{1}{2} (\hat{P}_n^{(k)})^2 + V(\boldsymbol{Q}_0) + \sum_{k=1}^{N} G_n^{(k)} \hat{Q}_n^{(k)} + \sum_{k=1}^{N} (\Omega^{(k)})^2 [\hat{Q}_n^{(k)}]^2 \tag{1.56}$$

Here

$$\hat{P}_n^{(k)}(\boldsymbol{Q}_0) = \sum_{l=1}^{N} T_{l,k} (M^{(l)})^{-1/2} \hat{P}^{(l)} \tag{1.57}$$

and

$$G_n^{(k)}(\boldsymbol{Q}_0) = \sum_{l=1}^{N} T_{l,k}(M^{(l)})^{-1/2} \frac{\partial V}{\partial Q^{(l)}}|_{\boldsymbol{Q}=\boldsymbol{Q}_0} \tag{1.58}$$

In the next step, eq 1.51 is rewritten in the following way:

$$\begin{aligned}[\delta\hat{F}e^{-\beta\hat{H}_b}]_W(\boldsymbol{Q}_0,\boldsymbol{P}_0) = \Big\langle \boldsymbol{Q}_0|e^{-\beta\hat{H}_b}|\boldsymbol{Q}_0\Big\rangle \int d\Delta e^{-iP_0\Delta/\hbar}\times \\ \frac{\Big\langle \boldsymbol{Q}_0+\Delta/2|e^{-\beta\hat{H}_b}|\boldsymbol{Q}_0-\Delta/2\Big\rangle}{\Big\langle \boldsymbol{Q}_0|e^{-\beta\hat{H}_b}|\boldsymbol{Q}_0\Big\rangle}\delta F(\boldsymbol{Q}_0+\Delta/2)\end{aligned} \tag{1.59}$$

The LHA given in eq 1.56 is then applied to the ratio,
$\Big\langle \boldsymbol{Q}_0+\Delta/2|e^{-\beta\hat{H}_b}|\boldsymbol{Q}_0-\Delta/2\Big\rangle / \Big\langle \boldsymbol{Q}_0|e^{-\beta\hat{H}_b}|\boldsymbol{Q}_0\Big\rangle$. This results in an analytical solution for the integrand in eq. 1.49 by using the following simplication:

$$\frac{\Big\langle \boldsymbol{Q}_0+\Delta/2|e^{-\beta\hat{H}_b}|\boldsymbol{Q}_0-\Delta/2\Big\rangle}{\Big\langle \boldsymbol{Q}_0|e^{-\beta\hat{H}_b}|\boldsymbol{Q}_0\Big\rangle} \approx \exp[-\sum_{j=1}^{N}\alpha^{(j)}(\Delta_n^{(j)}/2)^2] \tag{1.60}$$

where

$$\Delta_n^{(j)} = \sum_{k=1}^{N} T_{k,j}\sqrt{M^{(k)}}\Delta^{(k)} \tag{1.61}$$

and

$$\alpha^{(j)} = \frac{\Omega^{(j)}}{\hbar} coth[\beta\hbar\Omega^{(j)}/2] \tag{1.62}$$

In order to simplify the $\Delta-$dependence of the force in eq. 1.59, $\delta F(\boldsymbol{Q}_0+\Delta/2)$ is approximated by its quadratic expansion, in terms of $\Delta/2$, around $\boldsymbol{Q}=\boldsymbol{Q}_0$:

$$\begin{aligned}\delta F(\boldsymbol{Q}_0 + \Delta/2) &\approx \delta F(\boldsymbol{Q}_0) + \sum_{k=1}^{N} {F'}_k \frac{\Delta^{(k)}}{2} + \frac{1}{2}\sum_{k=1}^{N}\sum_{l=1}^{N} {F''}_{k,l} \frac{\Delta^{(k)}}{2}\frac{\Delta^{(l)}}{2} \\ &= \delta F(\boldsymbol{Q}_0) + \sum_{k=1}^{N} \tilde{F}'_k \frac{\Delta_n^{(k)}}{2} + \frac{1}{2}\sum_{k=1}^{N}\sum_{l=1}^{N} \tilde{F}''_{k,l} \frac{\Delta_n^{(k)}}{2}\frac{\Delta_n^{(l)}}{2}\end{aligned} \tag{1.63}$$

Here

$$F'_k = \frac{\partial F}{\partial Q^{(k)}}|_{\boldsymbol{Q}=\boldsymbol{Q}_0}; F''_{k,l} = \frac{\partial^2 F}{\partial Q^{(k)} \partial Q^{(l)}}|_{\boldsymbol{Q}=\boldsymbol{Q}_0} \tag{1.64}$$

and

$$\tilde{F}'_k = \sum_{l=1}^{N} (M^{(l)})^{-1/2} T_{l,k} F'_l; \tilde{F}''_{k,l} = \sum_{i=1}^{N}\sum_{j=1}^{N} (M^{(i)} M^{(j)})^{-1/2} T_{i,l} T_{j,k} F''_{i,j} \tag{1.65}$$

In the next step, the approximations in eq 1.60 and eq 1.63 are substituted into eq 1.51, followed by changing the integration variables from $\{\Delta^{(k)}\}$ to $\{\Delta_n^{(k)}\}$, and performing the Gaussian integral over $\{\Delta_n^{(k)}\}$ analytically. This results in the following:

$$\begin{aligned}[\delta \hat{F} e^{-\beta \hat{H}_b}]_W = \left\langle \boldsymbol{Q}_0 | e^{-\beta \hat{H}_b} | \boldsymbol{Q}_0 \right\rangle \prod_{j=1}^{N} \left(\frac{4\pi}{M^{(j)} \alpha^{(j)}} \right)^{1/2} \exp\left[-\frac{(P_{n,0}^{(j)})^2}{p^2 \alpha^{(j)}} \right] \times \\ [\delta F(\boldsymbol{Q}_0) + D(\boldsymbol{Q}_0, \boldsymbol{P}_{n,0})]\end{aligned} \tag{1.66}$$

Here

$$D(\boldsymbol{Q}_0, \boldsymbol{P}_{n,0}) = -i \sum_{k=1}^{N} \frac{\tilde{F}'_k P_{n,0}^{(k)}}{\hbar \alpha^{(k)}} + \sum_{k=1}^{N} \frac{\tilde{F}''_{k,k}}{4\alpha^{(k)}} - \sum_{k,l=1}^{N} \frac{\tilde{F}''_{k,l} P_{n,0}^{(k)} P_{n,0}^{(l)}}{2\hbar^2 \alpha^{(k)} \alpha^{(l)}} \tag{1.67}$$

In the final step, eq. 1.66 is substituted back into eq. 1.49 followed by changing the

integration variables from $\{P_0^{(k)}\}$ to $\{P_{n,0}^{(k)}\}$ resulting in the final form of the LHA-LSC approximation of the quantum-mechanical FFCF:

$$C(t) \approx \int d\boldsymbol{Q}_0 \frac{\left\langle \boldsymbol{Q}_0 | e^{-\beta \hat{H}_b} | \boldsymbol{Q}_0 \right\rangle}{Z_b} \int d\boldsymbol{P}_{n,0} \prod_{j=1}^{N} \left(\frac{1}{\alpha^{(j)} \pi \hbar^2} \right)^{1/2} \times \exp\left[-\frac{(P_{n,0}^{(j)})^2}{\hbar^2 \alpha^{(j)}} \right] [\delta F(\boldsymbol{Q}_0) + D(\boldsymbol{Q}_0, \boldsymbol{P}_{n,0})] \delta F(\boldsymbol{Q}_t^{(Cl)}) \tag{1.68}$$

The LHA-LSC approximation, eq 1.68, has been successfully applied to the calculation of VER rate constant in many systems, discussed in chapters II, III and IV. Some of the prominent features of the method, that should be noted are listed below:

1. The LHA-LSC approximation, given in eq 1.68, is exact at time $t = 0$. This can be proved by considering that the integral over $D(\boldsymbol{Q_0}, \boldsymbol{P_{n,0}})$ with respect to $\boldsymbol{P_{n,0}}$ vanishes at $t = 0$. The only term left is $[\delta F(\boldsymbol{Q_0})]^2$, which upon integration over $\boldsymbol{Q_0}$ yields the exact result:

$$\begin{aligned} \frac{1}{Z_b} \int d\boldsymbol{Q_0} \left\langle \boldsymbol{Q_0} | e^{-\beta \hat{H}_b} | \boldsymbol{Q_0} \right\rangle [\delta F(\boldsymbol{Q_0})]^2 = \\ \frac{1}{Z_b} \int d\boldsymbol{Q_0} \left\langle \boldsymbol{Q_0} | e^{-\beta \hat{H}_b} [\delta \hat{F}]^2 | \boldsymbol{Q_0} \right\rangle \\ = \frac{Tr(e^{-\beta \hat{H}_b} [\delta \hat{F}]^2)}{Tr(e^{-\beta \hat{H}_b})} \end{aligned} \tag{1.69}$$

2. The classical limit of the LHA-LSC approximation, eq 1.68, coincides with the exact classical correlation function. This can be proved by considering that, in the classical limit:

   (a) $\left\langle \boldsymbol{Q}_0 | e^{-\beta \hat{H}_b} | \boldsymbol{Q}_0 \right\rangle / Z_b \to e^{-V(\boldsymbol{Q}_0)} / \int d\boldsymbol{Q}_0 e^{-V(\boldsymbol{Q}_0)}$

   (b) $\alpha^{(j)} \to 2/\beta\hbar^2$ since $\beta\hbar\Omega^{(j)} \ll 1$, such that $\sum_{j=1}^{N} (P_{n,0}^{(j)})^2 / \hbar^2 \alpha^{(j)} \to \beta \sum_{j=1}^{N} (P_{n,0}^{(j)})^2 / 2 \to$

$\beta \sum_{j=1}^{N} (P_0^{(j)})^2/2M^{(j)}$, and

(c) $D(\boldsymbol{Q}_0, \boldsymbol{P}_{n,0})$, eq 1.67, vanishes as $\hbar \to 0$, so eq 1.68 reduces to the averaging over the time correlation of the classical forces, $\delta F(\boldsymbol{Q}_0)\delta F(\boldsymbol{Q}_t^{(Cl)})$.

3. There are three main ways by which the quantum effects are taken into account in the LHA-LSC approximation:

(a) The initial positions are sampled based on the exact quantum probability density

$$Prob(\boldsymbol{Q}_0) = \frac{\left\langle \boldsymbol{Q}_0 | e^{-\beta \hat{H}_b} | \boldsymbol{Q}_0 \right\rangle}{Z_b} = \frac{\left\langle \boldsymbol{Q}_0 | e^{-\beta \hat{H}_b} | \boldsymbol{Q}_0 \right\rangle}{\int d\boldsymbol{Q}_0 \left\langle \boldsymbol{Q}_0 | e^{-\beta \hat{H}_b} | \boldsymbol{Q}_0 \right\rangle} \tag{1.70}$$

(b) The initial (normal-mode) momenta are sampled based on a nonclassical probability density

$$Prob(\boldsymbol{P}_{n,0}) = \prod_{j=1}^{N} \left(\frac{1}{\alpha^{(j)} \pi \hbar^2} \right)^{1/2} exp \left[-\frac{(P_{n,0}^{(j)})^2}{\hbar^2 \alpha^{(j)}} \right] \tag{1.71}$$

Here, $\alpha^{(j)}$ and therefore Prob($\boldsymbol{P}_{n,0}$) depend parametrically on $\boldsymbol{Q}_0$.

(c) The term $D(\boldsymbol{Q}_0, \boldsymbol{P}_{n,0})$, eq 1.67, represents a purely quantum-mechanical effect originating from the fact that $\hat{F}$ does not commute with $\hat{H}_b$, such that $(\hat{F} e^{\beta \hat{H}_b})_W \neq (\hat{F})_W (e^{-\beta \hat{H}_b})_W$ and has no classical analogue.

4. It should be noted that the above-mentioned quantum effects include $\hbar$ to all orders. This should be contrasted with QCFs that are obtained by expanding the quantum-mechanical FFCF in powers of $\hbar$, to the first nonvanishing order.

5. It is important to note that the LHA-LSC FFCF in eq 1.68, is complex since $D(\boldsymbol{Q}_0, \boldsymbol{P}_{n,0})$, given in eq. 1.67 is complex. The LHA-LSC FFCF also satisfies the fundamental quantum-mechanical identity $C(-t) = C^*(t)$, implying that its

FT, $\tilde{C}(\omega)$, is real. At the same time, it does not rigorously satisfy the quantum-mechanical identity $\tilde{C}(-\omega) = e^{-\beta\hbar\omega}\tilde{C}(\omega)$. The reader is encouraged to ref (122) for a more detailed discussion of the various possible approximations arising from this result.

6. Lastly, it is important to note that, the LHA in eq 1.56 is used to specifically calculate the ratio of the off-diagonal and diagonal elements of the Boltzmann operator,

   $\left\langle \boldsymbol{Q}_0 + \Delta/2|e^{-\beta\hat{H}_b}|\boldsymbol{Q}_0 - \Delta/2\right\rangle / \left\langle \boldsymbol{Q}_0|e^{-\beta\hat{H}_b|\boldsymbol{Q}_0}\right\rangle$ (cf. eq 1.60). This is important to implement in order to yield the correct classical limit and coincide with the exact result at $t = 0$. It is important to note that the LHA involves a quadratic expansion only in terms of Δ, while any anharmonicity in terms of $\boldsymbol{Q}_0$ remains fully accounted for.

The LHA-LSC method has been successfully implemented in the calculation of the VER rate constant in several systems (87; 62; 86; 76; 54; 56). However, one of the major disadvantages of the method lies in the fact that, the calculation of the first and second derivatives of the bath-induced force with respect to the bath coordinates that are required as input for calculating the $D(\boldsymbol{Q}_0, \boldsymbol{P}_{n,0})$ term, given in eq 1.67, gets more and more computationally expensive with the increase in the complexity of the force fields. An alternate scheme of the LHA-LSC method, based on implementing the linearization approximation on the symmetrized FFCF, instead of the standard FFCF, has been devised by Geva and co-workers followed by successful applications to systems with various levels of complexities(78). This LHA-LSC scheme is described in the next subsection and the applications are discussed in chapters II, III and IV.

1.1.6 Vibrational Energy Relaxation Rate Constant using LSC Approximation without Force Derivatives

The force derivatives free LHA-LSC approximation, FDF-LHA-LSC,(63) is based on applying the linearized semiclassical approximation to the symmetrized FFCF, rather than the standard FFCF, as was done in the previous scheme (LHA-LSC method, discussed in subsection 1.1.5). In this subsection the derivation of the FDF-LHA-LSC method is outlined, primarily focusing on the differences of the new scheme(FDF-LHA-LSC method) with the last scheme(LHA-LSC method). To this end, considering the VER rate constant, in eq 1.47, based on the standard FFCF, given in eq 1.43, in the new scheme the VER rate constant is written in terms of symmetrized FFCF that has the following form:

$$C_s(t) = \frac{1}{Z} Tr[e^{-\beta\hat{H}/2}\delta\hat{F}e^{-\beta\hat{H}/2}e^{i\hat{H}t/\hbar}\delta\hat{F}e^{-i\hat{H}t/\hbar}] \tag{1.72}$$

The population relaxation rate constant in terms of $C_s(t)$ is of the following form:

$$k_{10} = \frac{1}{2\mu\hbar\omega_{10}} e^{\beta\hbar\omega_{10}/2}\tilde{C}_s(\omega_{10}) \tag{1.73}$$

where,

$$\tilde{C}(\omega_{10}) = e^{\beta\hbar\omega_{10}/2}\tilde{C}_s(\omega_{10}) \tag{1.74}$$

The LHA-LSC approximation of the symmetrized quantum-mechanical FFCF has the following form:

$$C_s^{LSC}(t) = \frac{1}{(2\pi\hbar)^N} \int d\boldsymbol{Q}_0 \int d\boldsymbol{P}_0 [e^{-\beta\hat{H}/2}\delta\hat{F}e^{-\beta\hat{H}/2}]_W(\boldsymbol{Q}_0, \boldsymbol{P}_0)\delta F(\boldsymbol{Q}_t^{(Cl)}) \tag{1.75}$$

Evaluating the Wigner transform in eq 1.75 in case of a many-body anharmonic

system is extremely challenging:

$$[e^{-\beta\hat{H}/2}\delta\hat{F}e^{-\beta\hat{H}/2}]_W(\boldsymbol{Q}_0\boldsymbol{P}_0) = \int d\Delta e^{-i\boldsymbol{P}_0\Delta/\hbar}\times \left\langle \boldsymbol{Q}_0 + \frac{\Delta}{2}|e^{-\beta\hat{H}/2}\delta\hat{F}e^{-\beta\hat{H}/2}|\boldsymbol{Q}_0 - \frac{\Delta}{2}\right\rangle \tag{1.76}$$

In the next step, the closure relation $\int d\boldsymbol{Q}'|\boldsymbol{Q}'\rangle\langle\boldsymbol{Q}'| = \hat{1}$ is used to rewrite the matrix element in the integrand in the following form:

$$\begin{aligned} &\left\langle \boldsymbol{Q}_0 + \frac{\Delta}{2}|e^{-\beta\hat{H}/2}\delta\hat{F}e^{-\beta\hat{H}/2}|\boldsymbol{Q}_0 - \frac{\Delta}{2}\right\rangle \\ &= \int d\boldsymbol{Q}\delta F(\boldsymbol{Q}')\left\langle \boldsymbol{Q}_0 + \frac{\Delta}{2}|e^{-\beta\hat{H}/2}|\boldsymbol{Q}'\right\rangle\left\langle \boldsymbol{Q}'|e^{-\beta\hat{H}/2}|\boldsymbol{Q}_0 - \frac{\Delta}{2}\right\rangle \\ &= \int d\boldsymbol{Q}\delta F(\boldsymbol{Q}')\left\langle \boldsymbol{Q}_0|e^{-\beta\hat{H}/2}|\boldsymbol{Q}'\right\rangle\left\langle \boldsymbol{Q}'|e^{-\beta\hat{H}/2}|\boldsymbol{Q}_0\right\rangle \\ &\quad \frac{\left\langle \boldsymbol{Q}_0 + \frac{\Delta}{2}|e^{-\beta\hat{H}/2}|\boldsymbol{Q}'\right\rangle\left\langle \boldsymbol{Q}'|e^{-\beta\hat{H}/2}|\boldsymbol{Q}_0 - \frac{\Delta}{2}\right\rangle}{\left\langle \boldsymbol{Q}_0|e^{-\beta\hat{H}/2}|\boldsymbol{Q}'\right\rangle\left\langle \boldsymbol{Q}'|e^{-\beta\hat{H}/2}|\boldsymbol{Q}_0\right\rangle} \end{aligned} \tag{1.77}$$

The LHA around $\boldsymbol{Q} = \boldsymbol{Q}^*$ is then applied to the ratio in the integrand in eq 1.77, and the LHA-LSC approximation of $C_s(t)$ is finally obtained by analytically solving the resulting Gaussian integral over Δ:

$$\begin{aligned} &C_s^{LHA-LSC}(t) = \int d\boldsymbol{Q}_0 \int d\boldsymbol{Q}' \frac{\left\langle \boldsymbol{Q}_0|e^{-\beta\hat{H}/2}|\boldsymbol{Q}'\right\rangle\left\langle \boldsymbol{Q}'|e^{-\beta\hat{H}/2}|\boldsymbol{Q}_0\right\rangle}{Z} \\ &\int d\boldsymbol{P}_n \prod_{j=1}^{N}\left(\frac{1}{\alpha^{(j)}\pi\hbar^2}\right)^{1/2} exp\left[\frac{(P_n^{(j)})^2}{\hbar^2\alpha^{(j)}}\right]\delta F(\boldsymbol{Q}')\delta F(\boldsymbol{Q}_t^{(Cl)}[\boldsymbol{Q}_0,\boldsymbol{P}_0]) \end{aligned} \tag{1.78}$$

Here, $\boldsymbol{P}_n = \boldsymbol{P}_n(\boldsymbol{Q}^*) = (P_n^{(1)}(\boldsymbol{Q}^*), ..., P_n^{(N)}(\boldsymbol{Q}^*))$ are the normal mode momenta that emergee from diagonalizing the Hessian matrix underlying the quadratic expansion of the bath potential energy around $\boldsymbol{Q} = \boldsymbol{Q}^*$ and $\{\alpha^{(j)}\}$ are given in eq. 1.62,

where $\{(\Omega^{(k)})^2\}$ are the eigenvalues of the Hessian matrix.

Eq 1.78 represents that FDF-LHA-LSC approximation of the quantum-mechanical FFCF. The computational feasibility and the accuracy of the method has been tested in several applications, for example, calculation of VER rate constant in neat liquid HCl and in cyanide ion in aqueous solution. Before delving into the applications, we discuss the prominent features of the FDF-LHA-LSC method:

1. One of the advantages of using the FDF-LHA-LSC method is the fact that, calculation of eq 1.78 does not require force derivatives as input, as was the case in the last scheme, eq 1.68. One consequence of this is that the term $D(\boldsymbol{Q}_0, \boldsymbol{P}_{n,0})$, given in eq 1.67, vanishes in the new scheme. As a result, the nonclassical behavior of the symmetrized FFCF is accounted for by the following attributes:

   (a) Nonclassical sampling of the bath coordinates and momenta.

   (b) The initial force is not calculated at the initial position used to generate the classical trajectory leading to the force at a later time t.

   (c) The factor $e^{\beta\hbar\omega_{10}/2}$, in eq 1.73, which coincides with the Schofield QCF.

2. It should also be noted that the correlation function given in eq 1.78 is in fact less approximate than the correlation function using the previous scheme, given in eq 1.68, on account of the fact that, in deriving eq. 1.78 it was not needed to perform the expansion of $\delta F(\boldsymbol{Q'})$ to second order around any point, including $\boldsymbol{Q_0}$, as was done in the previous scheme, (cf. eq 1.63).

3. The correlation function in eq 1.78 reduces to the classical FFCF in the classical limit, similar to the previous scheme, eq 1.68. However, it should be noted that the high frequency FT of the standard and symmetryzed FFCFs are expected to be highly nonclassical and hence may differ from each other significantly.

4. Lastly, it should be noted that the point $\boldsymbol{Q}^*$ around which the LHA is performed can be chosen to be either $\boldsymbol{Q_0}$, corresponding to the initial configuration for the classical trajectory that generates the force at time t, $\delta F(Q_t^{(Cl)})$, or, $\boldsymbol{Q'}$, corresponding to the configuration used to calculate the initial force, $\delta F(\boldsymbol{Q'})$, or a combination of the two. In the applications of the FDF-LHA-LSC method, the LHA is usually performed around $\boldsymbol{Q'}$, to obtain a better comparison with experiment, and to get results close to those obtained using eq 1.68.

This subsection concludes the section 1.1, where the theoretical background in the study of VER is outlined. The applications based on the theory given in section 1.1 are discussed in chapters II, III, IV. In the next section, the theoretical background for studying barrier crossing processes using classical dynamics is outlined, the application based on which is discussed in chapter V.

1.2 Classical Dynamics in Condensed Phase: Barrier Crossing Processes

Among the conventional reactive rate theories, transition state theory(235), reactive flux theory(228; 229; 230; 231; 232; 233) and Kramers' theory(211; 212) have been predominantly implemented for the analysis of barrier crossing processes in condensed phases for the last few decades. Reactive flux theory (RFT) provides a route for calculating the *exact* isomerization rate constant from MD simulations (provided of course that the dynamics can be described by classical mechanics and that the force fields are accurate). More specifically, the only assumption underlying RFT is that the rate of barrier crossing is slower than the rates of all other dynamical processes that take place in the reactant and product wells, so that the reaction dynamics can be described by a rate constant. RFT also allows the calculation of the rate constant by using trajectories that start at the barrier top, thereby bypassing convergence

problems associated with rare event statistics.(234) The popular transition-state theory (TST) can be obtained from RFT in the limit where barrier *recrossing* events are negligible. Finally, it should be noted that Kramers' theory, which is often invoked to describe solvent effects on reaction rate constants, is based on describing the underlying dynamics in terms of a Langevin equation. The latter avoids a molecularly detailed description of the solvent and accounts for solvent effects in terms of the dependence of the rate of recrossing on the solvent viscosity. A detailed mathematical derivation of the RFT and TST is provided in subsections 1.2.3 and 1.2.4, respectively.

1.2.1 Free Energy Calculations

An important part of studying barrier crossing processes using MD simulations is the molecular level understanding of the free energy profile of the process. During the investigation of solvent effects in the single bond *cZt-tZt* isomerization reaction of 1,3,5-cis-hexatriene using MD simulations, the free energy calculations proved to be a primary tool for the understanding of the isomerization reaction. In this subsection the theoretical detail of free energy calculations is outlined, and the application to the single bond *cZt-tZt* isomerization reaction of 1,3,5-cis-hexatriene is discussed in chapter V.

- Umbrella Sampling

  Umbrella sampling is one of the methods to study free energy changes associated with barrier crossing processes like chemical reactions and/or phase changes. The underlying idea behind umbrella sampling is that, in order to estimate the free energy difference between two states of a system, one needs to sample the configuration space accessible to both the states. In a single simulation, sampling configuration space spanning all the states of the system is prevented by the difficulty of sampling configurations at and near the local and/or global

maxima. In umbrella sampling, this is achieved by modifying the Markov chain that governs the sampling of configuration space which in turn is attained by replacing the Boltzmann factor of the system by a nonnegative weight function, or bias(26). To this end, consider two N-particle systems, 0 and 1, with partition functions Q_0 and Q_1. The free energy difference between the systems, $\Delta F = F_1 - F_0$, can be expressed as:

$$\Delta F = -k_B T ln \frac{Q_1}{Q_0} = -k_B T ln \left(\frac{\int d\boldsymbol{r}^N e^{-\beta U_1(\boldsymbol{r}^N)}}{\int d\boldsymbol{r}^N e^{-\beta U_0(\boldsymbol{r}^N)}} \right) \tag{1.79}$$

where, $U_0(\boldsymbol{r}^N)$ and $U_1(\boldsymbol{r}^N)$ represent the potential energy of N-dimensional systems 0 and 1, with coordinates represented by $\boldsymbol{r}$. As a result of replacing the Boltzmann factor of the system by a nonnegative weight function (or bias) $\pi(\boldsymbol{r}^N)$(26), the expression for $\left\langle e^{-\beta \Delta U} \right\rangle_0$ becomes the following:

$$\left\langle e^{-\beta \Delta U} \right\rangle_0 = \frac{\int d\boldsymbol{r}^N \pi(\boldsymbol{r}^N) e^{-\beta U_1(\boldsymbol{r}^N)} / \pi(\boldsymbol{r}^N)}{\int d\boldsymbol{r}^N \pi(\boldsymbol{r}^N) e^{-\beta U_0(\boldsymbol{r}^N)} / \pi(\boldsymbol{r}^N)} \tag{1.80}$$

In the next step, the notation $\langle ... \rangle_\pi$ is introduced to denote an average over probability distribution proportional to $\pi(\boldsymbol{r}^N)$, such that, eq 1.80 can be written as following:

$$\left\langle e^{-\beta \Delta U} \right\rangle_0 = \frac{\left\langle e^{-\beta U_1} / \pi \right\rangle_\pi}{\left\langle e^{-\beta U_0} / \pi \right\rangle_\pi} \tag{1.81}$$

In order for the numerator and the denominator in eq 1.81 to be non-zero, there needs to be enough overlap in $\pi(\boldsymbol{r}^N)$ between the regions of configuration space sampled by system 0 and system 1. In general, a number of MD simulations with the bias $\pi(\boldsymbol{r}^N)$, referred to as *umbrella sampling* runs, are carried out

in windows of configuration space with slight overlap among each other. After enough umbrella sampling runs have been carried out, such that the whole configuration space has been sampled, the potential energy sampled for all the windows are combined and the bias is removed, to obtain the *potential of mean force*. Weighted Histogram Analysis Method (WHAM)(27) is one of the methods employed in order to combine the umbrella sampling windows and obtaining the potential of mean force.

1.2.2 Preliminaries for quantitative study of barrier crossing processes

In this subsection, RFT for an isomerization reaction is formulated, as well as its TST limit, with emphasis on the underlying assumptions and the conditions for their validity. To this end, we restrict ourselves to the case of a unimolecular reaction, which is appropriate for the isomerization reaction under study here.

Consider a *classical* system with the following generic Hamiltonian:

$$H\left(s,\dot{s},\mathbf{Q},\dot{\mathbf{Q}}\right)=T\left(\dot{s},\dot{\mathbf{Q}}\right)+V\left(s,\mathbf{Q}\right)\ . \tag{1.82}$$

Here, s and $\dot{s}$ are the reaction coordinate and corresponding velocity, respectively; $\mathbf{Q}=(Q_1,Q_2,\ldots)$ and $\dot{\mathbf{Q}}=\left(\dot{Q}_1,\dot{Q}_2,\ldots\right)$ are the non-reactive coordinates and corresponding velocities, respectively; $T\left(\dot{s},\dot{\mathbf{Q}}\right)$ is the overall kinetic energy and $V\left(s,\mathbf{Q}\right)$ is the overall potential energy.

Next, let $s=s^{\ddagger}$ define the transition state (TS), such that $s<s^{\ddagger}$ and $s>s^{\ddagger}$ correspond to *reactant* and *product*, respectively. The heaviside function is defined as,

$$h(s)=\begin{cases}1 & s>s^{\ddagger}(\text{product})\\ 0 & s\leq s^{\ddagger}(\text{reactant})\end{cases}\ , \tag{1.83}$$

so that the product mole fraction at time t is given by:

$$x_P(t) = \int ds \int d\dot{s} \int \mathbf{dQ} \int \mathbf{d\dot{Q}} \rho \left(s, \dot{s}, \mathbf{Q}, \dot{\mathbf{Q}}; t \right) h(s) \equiv \langle h(s) \rangle_t \ . \tag{1.84}$$

Here, $\rho \left(s, \dot{s}, \mathbf{Q}, \dot{\mathbf{Q}}; t \right)$ is the (nonequilibrium) phase-space density at time t. It should be noted that the reactant mole fraction at time t is given by:

$$x_R(t) = 1 - x_P(t) = \int ds \int d\dot{s} \int \mathbf{dQ} \int \mathbf{d}\rho \left(s, p, \mathbf{Q}, \dot{\mathbf{P}}; t \right) [1 - h(s)] \equiv 1 - \langle h(s) \rangle_t \ . \tag{1.85}$$

In the absence of external perturbation,

$$\rho \left(s, \dot{s}, \mathbf{Q}, \dot{\mathbf{Q}}; t \right) \stackrel{t \to \infty}{\longrightarrow} \rho_{eq} \left(s, \dot{s}, \mathbf{Q}, \dot{\mathbf{Q}} \right) \equiv \frac{\exp \left[-H \left(s, \dot{s}, \mathbf{Q}, \dot{\mathbf{Q}} \right) / k_B T \right]}{\int ds \int d\dot{s} \int \mathbf{dQ} \int \mathbf{d\dot{Q}} \exp \left[-H \left(s, \dot{s}, \mathbf{Q}, \dot{\mathbf{Q}} \right) / k_B T \right]} \ , \tag{1.86}$$

such that

$$x_P(t) \stackrel{t \to \infty}{\longrightarrow} x_{P,eq} \equiv \int ds \int d\dot{s} \int \mathbf{dQ} \int \mathbf{d\dot{Q}} \rho_{eq} \left(s, \dot{s}, \mathbf{Q}, \dot{\mathbf{Q}} \right) h(s) \equiv \langle h(s) \rangle_{eq} \tag{1.87}$$

$$x_R(t) \stackrel{t \to \infty}{\longrightarrow} x_{R,eq} \equiv \int ds \int d\dot{s} \int \mathbf{dQ} \int \mathbf{d\dot{Q}} \rho_{eq} \left(s, \dot{s}, \mathbf{Q}, \dot{\mathbf{Q}} \right) [1 - h(s)]$$

$$\equiv 1 - \langle h(s) \rangle_{eq} \ . \tag{1.88}$$

The concept of the *reaction rate constant* is based on assuming that the reaction dynamics can be described by a simple kinetic rate equation of the following form:

$$\dot{x}_P(t) = -\dot{x}_R(t) = -k_{RP} x_P(t) + k_{PR} x_R(t) \ , \tag{1.89}$$

where k_{PR} and k_{RP} are reactant-to-product and product-to-reactant reaction rate constants, respectively. Equivalently,

$$\delta \dot{x}_i(t) = -k \delta x_i(t) \ . \tag{1.90}$$

Here $i = P$ or R, $k = k_{PR} + k_{RP}$, $\delta x_i(t) = x_i(t) - x_i^{eq}$, $x_P^{eq} = k_{PR}/k$ and $x_R^{eq} = k_{RP}/k$.

It should be noted that relaxation processes are generally characterized by many relaxation times, not one. In order for reaction kinetics to be described by a single rate constant as in eq 1.90, the activation energy has to be much higher than k_BT, which results in the reaction rate constant being much slower on the time scale of all remaining nonreactive processes.(236; 237; 233) Under these circumstances, the reaction dynamics can be described by eq 1.90 (after a short transient time during which the reaction does not make significant progress)(233; 238).

Eq 1.90 can be easily solved to give $\delta x_i(t) = \delta x_i(0) \exp(-kt)$. Thus, the actual reaction rate constant can be obtained from the following expression:

$$k = \lim_{t \to t_p} k(t) = -\lim_{t \to t_p} \delta \dot{x}_i(t)/\delta x_i(0) \tag{1.91}$$

Here, $k(t)$ is explicitly time-dependent during an initial transient period, $0 < t < t_p (\ll 1/k)$, following which it will reach the "plateau region", where it acquires a fixed value (provided that $t \ll 1/k$). (233; 238) This fixed value corresponds to the reaction rate constant, k.

1.2.3 The reaction rate constant from linear response theory

Since activated processes follow *rare-event statistics*, direct evaluation of the reaction rate constant from eq 1.91 would typically require prohibitively long *non-equilibrium* MD simulations. Linear response theory (LRT)(228; 239) provides an alternative route for calculating reaction rate constants that can bypass this obstacle. To this end, one needs to take advantage of the fact that since *the reaction rate constant is independent of the choice of initial condition, one is free to choose an initial state which is in the close vicinity of thermal equilibrium.*(228; 240) It is this assumption that makes it possible to calculate the reaction rate constant via LRT.

The derivation of an expression for the reaction rate constant from LRT starts out by considering a classical system with the total Hamiltonian $H\left(\mathbf{R},\dot{\mathbf{R}}\right)+fA\left(\mathbf{R}\right)$ at $t<0$ and $H\left(\mathbf{R},\dot{\mathbf{R}}\right)$ at $t\geq 0$ ($\mathbf{R}\equiv(s,\mathbf{Q})$ in the context of the current derivation). Here, f is a scalar coefficient, and $A\left(\mathbf{R}\right)$ is any perturbation that can shift the system from its unperturbed thermal equilibrium phase-space density

$$\rho_{eq}\left(\mathbf{R},\dot{\mathbf{R}}\right)=\frac{e^{-H\left[\mathbf{R},\dot{\mathbf{R}}\right]/k_BT}}{\int\mathbf{dR}\int\mathbf{d}\dot{\mathbf{R}}e^{-H\left[\mathbf{R},\dot{\mathbf{R}}\right]/k_BT}}\ . \tag{1.92}$$

At $t=0$, the system is assumed to be in thermal equilibrium with respect to the perturbed Hamiltonian, so that its initial phase-space density is given by:

$$\rho(\mathbf{R},\dot{\mathbf{R}};t=0)=\frac{e^{-[H(\mathbf{R},\dot{\mathbf{R}})+fA(\mathbf{R})]/k_BT}}{\int\mathbf{dR}\int\mathbf{d}\dot{\mathbf{R}}e^{-[H(\mathbf{R},\dot{\mathbf{R}})+fA(\mathbf{R})]/k_BT}}\ . \tag{1.93}$$

Thus, the ensemble-averaged value of a dynamical variable $B(\mathbf{R})$ at time $t\geq 0$ is given by

$$\langle B\rangle_{eq}(t)=\frac{\int\mathbf{dR}_0\int\mathbf{d}\dot{\mathbf{R}}_0e^{-[H(\mathbf{R}_0,\dot{\mathbf{R}}_0)+fA(\mathbf{R}_0)]/k_BT}B(\mathbf{R}_t)}{\int\mathbf{dR}_0\int\mathbf{d}\dot{\mathbf{R}}_0e^{-[H(\mathbf{R}_0,\dot{\mathbf{R}}_0)+fA(\mathbf{R}_0)]/k_BT}}\ . \tag{1.94}$$

Here $\mathbf{R}_t$ is obtained by solving the classical equation of motion under the Hamiltonian $H(\mathbf{R},\dot{\mathbf{R}})$, with the initial conditions $\left\{\mathbf{R}_0,\dot{\mathbf{R}}_0\right\}$, to obtain $\left\{\mathbf{R}_t,\dot{\mathbf{R}}_t\right\}$ at time t.

Assuming that the initial phase-space density is close enough to the unperturbed equilibrium phase-space density, $\rho_{eq}\left(s,\dot{s},\mathbf{Q},\dot{\mathbf{Q}}\right)$, for the linear response limit, $f\ll 1$, to be valid, one may replace eq 1.94 by its expansion to first order in powers of f. This then results in the following expression for $\langle\delta B\rangle_{eq}(t)$ in terms of an equilibrium two-time correlation function:

$$\langle\delta B\rangle_{eq}(t)=\frac{f}{k_BT}\langle\delta A(\mathbf{R}_0)\delta B(\mathbf{R}_t)\rangle_{eq}\ , \tag{1.95}$$

where $\delta A(\mathbf{R})=A(\mathbf{R})-\langle A\rangle_{eq}$ and $\delta B(\mathbf{R})=B(\mathbf{R})-\langle B\rangle_{eq}$.

Now, assuming that $A = B = h(s)$, eq 1.95 reduces to:

$$\langle \delta h \rangle_{eq}(t) \equiv \delta x_P(t) = \frac{f}{k_B T} \langle \delta h(s_0) \delta h(s_t) \rangle_{eq} \ . \tag{1.96}$$

Substituting eq 1.96 into eq 1.91 then yields:

$$k = -\lim_{t \to t_p} \frac{\langle \delta h(s_0) \delta \dot{h}(s_t) \rangle_{eq}}{\langle [\delta h(s_0)]^2 \rangle_{eq}} = \lim_{t \to t_p} \frac{\langle \delta \dot{h}(s_0) \delta h(s_t) \rangle_{eq}}{x_{R,eq} x_{P,eq}} \ . \tag{1.97}$$

Noting that $\delta \dot{h} = \dot{h} = \delta \left[s - s^{\ddagger} \right] \dot{s}$ is the *reactive flux*, we obtain the following expression for the reaction rate constant:

$$k = \lim_{t \to t_p} \frac{1}{x_{R,eq} x_{P,eq}} \langle \delta \left[s_0 - s^{\ddagger} \right] \dot{s}_0 h(s_t) \rangle_{eq} \ . \tag{1.98}$$

It should be noted that $k_{PR} = k x_{P,eq}$ and $k_{RP} = k x_{R,eq}$. eq 1.98 is the RFT expression for the reaction rate constant. Importantly, it represents an *exact* expression for the rate constant, provided that classical mechanics is valid and the force fields are accurate.

1.2.4 Transition state theory

TST can be obtained from eq 1.98 by replacing $h\left[s_t\right]$ by $h\left[\dot{s}_0\right]$. This assumption is equivalent to neglecting barrier *recrossing*, that is assuming that starting at a TS configuration with a positive velocity along the reaction coordinate ($\dot{s} > 0$) guarantees barrier crossing, that is $h(s_t) = 1$. This then leads to the following expression for the reaction rate constant:

$$k_{TST} = \frac{1}{x_{R,eq} x_{P,eq}} \langle \delta \left(s - s^{\ddagger} \right) \dot{s} h(\dot{s}) \rangle_{eq} = \langle \dot{s} h(\dot{s}) \rangle_{eq} \langle \delta \left(s - s^{\ddagger} \right) \rangle_{eq} \ . \tag{1.99}$$

Importantly, the TST reaction rate constant is given in terms of an *equilibrium* ensem-

ble average, as opposed to an equilibrium two-time correlation function within RFT. As a result the $\dot{s}$-dependent and s-dependent factors can be averaged separately.

The s-dependent factor in eq 1.99 can be put in the Arrhenius form:

$$\begin{aligned}
&\frac{1}{x_{R,eq}}\langle\delta\left(s-s^{\ddagger}\right)\rangle_{eq} \\
&= \frac{\int \mathbf{dQ}\exp\left[-V(\mathbf{Q},s^{\ddagger}/k_BT\right]}{\int \mathbf{dQ}\int_{s\leq s^{\ddagger}} ds\exp\left[-V(\mathbf{Q},s)/k_BT\right]} \\
&= \exp\left[-\Delta G^{\ddagger}/k_BT\right] = \exp\left[\Delta S^{\ddagger}/k_B\right]\exp\left[-\Delta H^{\ddagger}/k_BT\right] \ . \qquad (1.100)
\end{aligned}$$

Here, $\Delta G^{\ddagger} = G^{\ddagger} - G^R$, $\Delta S^{\ddagger} = S^{\ddagger} - S^R$ and $\Delta H^{\ddagger} = H^{\ddagger} - H^R$ are the Gibbs free energy, entropy and enthalpy difference between the TS and the reactant state (assuming that the reaction takes place under constant temperature and pressure). Thus, the reactant-to-product rate reaction rate constant is given by:

$$k_{PR}^{TST} = A\exp\left[-\Delta H^{\ddagger}/k_BT\right] \ , \qquad (1.101)$$

with

$$A = \langle\dot{s}h(\dot{s})\rangle_{eq}\exp\left[\Delta S^{\ddagger}/k_B\right] \qquad (1.102)$$

Finally, comparison to eq 1.98 reveals that

$$k_{PR} = \kappa k_{PR}^{TST} \ , \qquad (1.103)$$

where κ is the so-called *transmission coefficient*, which is explicitly given by:

$$\kappa = \lim_{t\to t_p}\frac{\langle\dot{s}_0\delta\left[s_0-s^{\ddagger}\right]h(s_t)\rangle_{eq}}{\langle\dot{s}h(\dot{s})\rangle_{eq}} \ . \qquad (1.104)$$

It should be noted that $\kappa < 1$ due to recrossing and that as a result, k_{TST} corresponds to an upper bound on the actual rate constant, $k \leq k_{TST}$.

This subsection concludes the section 1.2, where the theoretical background of studying barrier crossing processes using classical dynamics is outlined, the application based on the theory discussed in this section is detailed in chapter V.

CHAPTER II

Vibrational Lifetimes of Cyanide Ion in Aqueous Solution From Molecular Dynamics Simulations: Intermolecular vs. Intramolecular Accepting Modes

2.1 Introduction

Understanding the time scale and mechanism of vibrational energy relaxation (VER) in condensed phase systems at the molecular level is key for understanding chemical reactivity.(36; 37; 38; 39; 40; 41; 42; 43; 44; 45) Over the last several decades, VER has been studied extensively in variety of condensed phase systems, using experimental (46; 159; 48; 48; 49; 50; 51; 52; 53) and computational (54; 55; 56; 57; 58; 59; 60; 61; 62; 63; 64; 65; 66; 67; 68; 69; 70; 71; 72; 73; 74; 75; 76; 77; 78) techniques. Those studies have demonstrated that VER can occur over a wide range of time scales and via different mechanisms, depending on the frequency of the relaxing and accepting modes and the nature of the interaction between them.

The majority of computational studies of VER were based on the Landau-Teller (LT) formula.(40; 155) The latter is based on assuming weak coupling between the relaxing mode (the system) and the remaining degrees of freedom (the bath), and

leads to a description of VER in terms of rate kinetics. The rate constant for VER from the first excited to the ground vibrational state of the relaxing mode, whose inverse corresponds to the first excited state VER lifetime, is given in terms of the Fourier transform (FT), at the vibrational transition frequency, of the free-bath two-time autocorrelation function of the force exerted on the relaxing mode by the bath. When the frequency mismatch between the relaxing and accepting modes is smaller than $k_BT/\hbar$, where T is the temperature and k_B is the Boltzmann constant, one expects the *classical* force-force correlation function (FFCF) to yield a reasonable approximation to the quantum FFCF.(80; 81; 66; 82; 83; 84; 85) However, quantum effects must be accounted for when this condition is not met. Since exact quantum molecular dynamics simulations are not feasible for most many-body anharmonic condensed phase systems of practical interest, such as molecular liquid solutions, accounting for quantum effects is usually done via approximate methods that range from using rigorous, yet computationally costly, semiclassical approximations(62; 86; 87; 56; 54; 76; 78) to employing heuristic quantum correction factors (QCFs).(64; 53; 67; 60; 88; 67; 60; 64; 59; 55; 89)

The cyanide ion in aqueous solution has been established over the last two decades as an important model system for understanding VER in polar liquid solutions. As such, it has been extensively studied using experimental and computational methods.(65; 58; 68; 70; 59; 72; 66; 75; 61; 46; 52; 71; 73). In particular, Hamm *et al.*(52) reported measuring VER lifetimes of different isotopomers of CN^- in liquid H_2O and D_2O via IR-pump-IR-probe spectroscopy. The experimental VER lifetimes for all the isotopomers range between 20 ps to 130 ps, depending on the isotopomer combination. Two interesting trends that emerged from the experimental measurement are:

- The VER lifetimes are considerably shorter in H_2O in comparison to D_2O.
- While the VER lifetime is insensitive to the C−N stretch frequency in the case of H_2O, there is a pronounced *decrease* in the VER lifetime with *increasing*

frequency of the C−N stretch in the case of D_2O.

Several previous computational studies attempted to reproduce the experimentally observed VER lifetimes and shed light on the molecular mechanism underlying them.(65; 58; 68; 70; 59; 72; 66; 75; 61; 46; 71; 73) An early paper by Rey and Hynes (59) reported a calculation of the VER lifetime of one isotopomer combination, $^{12}C^{14}N^{-}/H_2O$, based on the LT formula, using a *classical* force autocorrelation function and the standard QCF.(67; 60; 90) The FFCF was obtained from classical MD simulations that employed the *rigid* TIP4P water model and a four site charge model for CN^{-},(91) where the site charges were modified in order to obtain better agreement with the experimental VER lifetime. This resulted in a calculated VER lifetime of 58 ps, which is in reasonable agreement with the experimental value of 28±7 ps.(52) The calculations also suggested that electrostatic forces, as opposed to Lennard-Jones (LJ) forces, dominate VER in this system. However, the sensitivity of these results to the choice of site charges was later pointed out in Ref. (66) that reported a lifetime of 138 ps based on a calculation that employed the original site charges for CN^{-} from Ref. (91) and the same rigid TIP4P water model.

Okazaki and co-workers (66; 82; 68) later reported a series of calculations of the VER lifetime for the same isotopomer combination ($^{12}C^{14}N^{-}/H_2O$) via their mean-field mixed quantum classical method (MF/MQC) and a fully quantum-mechanical treatment based on a combination of instantaneous normal mode analysis of the solvent with either the Feynmann path integral influence functional (PI/IF) or Fermi's golden rule (PI/FGR). The MF/MQC method, which was based on treating the C−N stretch quantum-mechanically and the remaining degrees of freedom (DOF) classically, and employed a rigid TIP4P water model, yielded a VER lifetime of 110 ps. The PI/FGR method yielded a VER lifetime of 200 ps.(82) Those authors then repeated the calculations with a flexible SPC/E(92) water model, to obtain VER lifetimes of 24 ps and 30 ps(68) using MF/MQC and PI/FGR, respectively. Based

on those results, the authors concluded that the accepting modes in this system are intramolecular. However, it should be noted that their mixed quantum-classical approach treats the accepting modes as classical and as such may not be able to properly account for quantum effects.(39)

In another computational study that focused on the quantum effects in the same system, Bastida *et al.*(71; 73) have used the Ehrenfest method with quantum corrections to calculate the VER lifetime in the same isotopomer combination, ($^{12}C^{14}N^{-}/H_2O$). Their calculations yielded a lifetime of 150 ps when using the CN^{-} model used by Rey and Hynes (59) and 55 ps when using the CN^{-} model used by Okazaki,(82) (both with the rigid TIP4P water model). Further studies by the same authors focused on treating the CN^{-} stretch and the water vibrational modes quantum mechanically within their quantum-corrected Ehrenfest method(73) and yielded a bi-exponential VER that was attributed to the two types of accepting modes. The faster relaxation (20 ps lifetime) was assigned to bending water modes as accepting modes and accounted for 82% of the VER. A slower relaxation (180 ps lifetime) was assigned to translational and rotational solvent modes as accepting modes.

Jang *et al.* (61) have used centroid molecular dynamics(93; 94) (CMD) to study the VER in $^{12}C^{14}N^{-}/H_2O$. With this method, and using the flexible SPC/F_2(95) water model, they obtained a VER lifetime of 15 ps. However, the nature of the accepting modes was not reported in this study.

More recently, Lee *et al.*(75) used a classical nonequilibrium simulation of $^{12}C^{14}N^{-}$ dissolved in H_2O, D_2O and T_2O described by the rigid TIP3P water model(96) and the flexible KKY water model(97). The electrostatic interactions in this case were described by state-of-the-art distributed multiple moments obtained from ab-initio calculations. Within this framework, and using the flexible water model, calculated VER lifetimes of 19 and 34 ps were obtained in H_2O and D_2O, respectively (the corresponding experimental values of are (28±7)ps and (71±3)ps). Those authors

also showed that the agreement with experiment can be improved by modifying the van der Waals parameters by ∼20%.

The above mentioned previous studies suggest that at least two types of accepting modes can play a role in the VER of cyanide ion in aqueous solutions, namely:(73; 66)

- *Intermolecular accepting modes* that involve translational and rotational DOF of water.

- *Intramolecular accepting modes* that involve intramolecular vibrational DOF of water;

While most studies seem to point to the intramolecular accepting modes as being dominant, this conclusion has been reached based on assuming that the solvent can be treated as classical. Furthermore, the lifetimes are observed to be highly sensitive to the model parameters, which in some cases needed to be adjusted in order to obtain agreement with experiment. In addition, while those previous computational studies shed light on the molecular picture underlying VER of cyanide in aqueous solution, several important aspects of this system have not yet been addressed:

- Most previous studies have focused on $^{12}C^{14}N^{-}/H_2O$ and did not address the aforementioned experimentally observed considerable variation of VER lifetime with respect to the cyanide and water isotopomers.(52)

- While quantum effects have been considered, their relative importance when the accepting modes are either intermolecular or intramolecular have not been addressed. It should be noted that since the frequency mismatch between the relaxing and accepting modes is larger when the accepting modes are intermolecular, one expects quantum effects to be more important relative to the case where the accepting modes are intramolecular.

- The fact that the cyanide ion is electron rich suggest that it should be described

by a polarizable force field. However, most previous studies have been based on site charge models.

- All previous computational studies have assumed that the system is at infinite dilution with one cyanide ion in the simulation box, which correspond to concentrations lower than the experimental ones. Furthermore, it was usually assumed that the effect of counter ions need not be taken into account. It is therefore desirable to perform the simulations at concentrations that are consistent with experiment in order to incorporate the effect of interactions with neighboring cyanide ions and their counter ions.

Our objective in this research is to address the above mentioned aspects of the cyanide ion in aqueous solution system. We have attempted this in the following way:

- We present results for four different isotopomer combinations: $^{12}C^{14}N^-/H_2O$, $^{12}C^{14}N^-/D_2O$, $^{13}C^{15}N^-/H_2O$ and $^{13}C^{15}N^-/D_2O$.

- We account for quantum effects via QCFs that depend on the type of accepting modes.

- We describe the cyanide ion in terms of a polrizable force field.

- We base the calculations on MD simulations performed at concentrations comparable to the ones used in the experimental measurements in Ref. (52) and with explicit counter ions.

The remainder of this chapter is organized as follows. The theory underlying VER lifetime calculations within the framework of LT formula with classical FFCF and QCFs is outlined in Sec. 2.2. Computational techniques and force field parameters are discussed in Sec. 2.3. The results are presented and discussed in Sec. 2.4. A summary of the main results and outlook are provided in Sec. 2.5.

2.2 Theory

Consider a vibrational mode linearly coupled to a bath, so that the overall fully quantum-mechanical Hamiltonian is given by

$$\hat{H}_{tot} = \frac{\hat{p}^2}{2\mu} + v(\hat{q}) + \sum_{j=1}^{N} \frac{(\hat{P}^{(j)})^2}{2M^{(j)}} + V(\hat{\mathbf{Q}}) - \hat{q}F(\hat{\mathbf{Q}}) \ . \tag{2.1}$$

Here, $\hat{q}$, $\hat{p}$, μ and $v(\hat{q})$ are the relaxing mode coordinate, momentum, reduced mass, and bath-free vibrational potential, respectively; $\hat{\mathbf{Q}} = \left(\hat{Q}_1, \hat{Q}_2, \ldots \hat{Q}_N\right)$, $\hat{\mathbf{P}} = \left(\hat{P}_1, \hat{P}_2, \ldots \hat{P}_N\right)$, $M^{(1)}, ..., M^{(N)}$, and $V(\hat{\mathbf{Q}})$ are the coordinates, momenta, masses, and potential energy of the bath DOF; $F(\hat{\mathbf{Q}})$ is the force exerted by the bath on the relaxing mode *when the relaxing mode is frozen at its equilibrium configuration.*

The rate constant for population relaxation from the first-excited to the ground vibrational states is given by the fully-quantum mechanical LT formula:(40; 155)

$$k_{01} = \frac{1}{2\mu\hbar\omega_{10}} \tilde{C}(\omega_{10}) \ . \tag{2.2}$$

Here,

$$\tilde{C}(\omega) = \int_{-\infty}^{\infty} dt e^{i\omega t} C(t) \tag{2.3}$$

is the FT of the *free-bath quantum-mechanical FFCF*,

$$C(t) = \langle \delta\hat{F}(t)\delta\hat{F} \rangle \ , \tag{2.4}$$

where $\langle \hat{A} \rangle = Tr[e^{-\beta\hat{H}_b}\hat{A}]/Z_b$, $Z_b = Tr[e^{-\beta\hat{H}_b}]$, $\delta\hat{F} = \hat{F} - \langle\hat{F}\rangle$, $\beta = (k_B T)^{-1}$,

$$\delta\hat{F}(t) = e^{i\hat{H}_b t/\hbar}\delta\hat{F}e^{-i\hat{H}_b t/\hbar} \tag{2.5}$$

and

$$\hat{H}_b = \sum_{j=1}^{N} \frac{(\hat{P}^{(j)})^2}{2M^{(j)}} + V(\hat{\mathbf{Q}}) \ . \tag{2.6}$$

One fundamental difficulty encountered in practical applications of Eq. (2.2) is associated with the fact that the required input consists of the *quantum-mechanical* FFCF, rather than the *classical* FFCF. Unfortunately, the exact calculation of real-time quantum-mechanical correlation functions for general many-body anharmonic systems remains far beyond the reach of currently available computer resources, due to the exponential scaling of the computational effort with the number of DOF.(98) The most popular approach for dealing with this difficulty in the context of VER is to first evaluate the FT of the classical FFCF, and then multiply the result by a frequency-dependent QCF, $Q(\omega)$: (90; 99; 39; 60; 100; 67; 101; 102; 103; 104; 105; 106; 107; 108; 88; 109; 110)

$$\tilde{C}(\omega) \approx Q(\omega)\tilde{C}^{Cl}(\omega) \ . \tag{2.7}$$

Here, $\tilde{C}^{Cl}(\omega) = \int_{-\infty}^{\infty} dt e^{i\omega t} C^{Cl}(t)$, where $C^{Cl}(t) = \langle \delta F(t) \delta F \rangle^{Cl}$ is the *classical* FFCF ($\langle \cdots \rangle^{Cl}$ corresponds to averaging over the classical Boltzmann phase-space distribution and the time evolution of $\delta F(t)$ is governed by classical mechanics). Importantly, $C^{Cl}(t)$ can be evaluated with relative ease from classical MD simulations.

The QCF, $Q(\omega)$, is obtained based on the general properties of quantum correlation functions (e.g., detailed balance) and/or the knowledge of what $Q(\omega)$ looks like in the very few cases where it can be obtained explicitly.(64; 53; 67; 60; 88) In the case of rigid water, we follow the prescription proposed by Skinner and co-workers for choosing the QCF based on the nature of the accepting modes.(67; 60) More specifically, since in this case the accepting modes are *intermolecular* (i.e. solute vibration

to solvent translation/rotation VER) we employed the *harmonic/Schofield QCF*

$$Q_{HS}(\omega) = e^{\beta\hbar\omega/4}\left(\frac{\beta\hbar\omega}{1-e^{-\beta\hbar\omega}}\right)^{1/2} . \tag{2.8}$$

The nature of the accepting modes in the case of flexible water is less well defined due to significant coupling between the intramolecular and intermolecular DOF, which leads to broadening of resonances associated with intramolecular vibrational modes of water by hundreds of cm^{-1} (see Sec. 2.4). Thus, in the lack of a clear choice of QCF in this case, we opt for what one may argue is the simplest choice, namely the *standard QCF*,(67; 60; 90)

$$Q_{st}(\omega) = \frac{2}{1+e^{-\beta\hbar\omega}} . \tag{2.9}$$

As we will see in Sec. 2.4, this choice also happens to be consistent with the experimental vibrational lifetimes, whereas other choices, like the harmonic QCF or mixtures of the harmonic QCF and the harmonic/Schofield QCF (67) lead to vibrational lifetimes which are significantly shorter than the experimental ones.

It should be noted that $Q_{st}(\omega) \sim 2$ when $\beta\hbar\omega \gg 1$, which is the case for the C−N stretch at 300K, and therefore much smaller than the harmonic/Schofield QCF (Q_{HS} 38.53 and 34.25 for C−N stretch at 300K in $^{12}C^{14}N^-$ and $^{13}C^{15}N^-$, respectively). Thus, the quantum enhancement of VER into intermolecular accepting modes is significantly larger than that of VER into intramolecular accepting modes, which is to be expected in light of the larger frequency mismatch between relaxing and accepting modes in the case of *intermolecular* relative to *intramolecular* accepting modes.

2.3 Computational Methods

The interaction between cyanide and water were modeled in terms of the AMBER polarizable force field *ff02*.(111) Importantly, the force field parameters were

used as given rather than as adjustable parameters whose values are set so as to obtain agreement with experiment. The partial charges for CN^- were assigned using the restrained electrostatic potential (RESP)(112; 243; 242) method where the electrostatic potential is generated via Gaussian 09, at the HF/6-31G* level. The partial charges for C and N thus obtained are δ_C=-0.216698 and δ_N=-0.783302, respectively. The atomic polarizabilities for the C, N and K atoms were set as 0.36 $\mathring{A}^3$, 0.53 $\mathring{A}^3$, and 1.06 $\mathring{A}^3$ respectively. The SHAKE algorithm(247) was used to constrain the C−N bond length to its equilibrium value (1.177Å). Results obtained with the following two different water force fields were compared:

- The SPC/E force field(116) for modeling *rigid* water intermolecular accepting modes, where the rigidity was imposed by the SHAKE algorithm(247)
- The SPC/Fw force field(117) for modeling *flexible* water intramolecular accepting modes.

MD simulations were performed using the AMBER 10 software package for four different isotopomer combinations: $^{12}C^{14}N^-/H_2O$, $^{13}C^{15}N^-/H_2O$, $^{12}C^{14}N^-/D_2O$, $^{13}C^{15}N^-/D_2O$.

For each isotopomer combination, separate simulations were performed with either the rigid SPC/E or flexible SPC/Fw water force fields (8 independent simulated systems overall).

Simulations were performed using a cubical simulation box with periodic boundary conditions, containing 9 CN^- anions and 9 K^+ cations dissolved in either 605 rigid SPC/E water molecules or 753 flexible SPC/Fw water molecules, at a temperature of 300K and pressure of 1.0atm. Equilibration was carried out via the Andersen temperature coupling scheme.(246) In the case of rigid SPC/E water, the systems were equilibrated for 150 ps at constant pressure with a time step of 1.5 fs, resulting in a solution with 0.802M KCN concentration. In the case of flexible SPC/Fw water, the systems were equilibrated for 500 ps at constant pressure with a time step of

1.0 fs, resulting with 0.658M KCN concentration. It should be noted that these concentrations are comparable to the experimental concentrations (0.22-0.90M).(52)

All the reported VER rate constants were calculated from the corresponding FFCFs, obtained by averaging over 3.2×10^5 trajectories.

The statistical error associated with the VER lifetimes was given as the standard deviation calculated after dividing the trajectories in 10 blocks, with 3.9×10^4 trajectories per block, each of length 3.15 ps, for rigid SPC/E water, and 3.2×10^4 trajectories per block, each of length 2.1 ps, for flexible SPC/Fw water, respectively.

2.4 Results

2.4.1 Rigid SPC/E water

$\tilde{C}_{Cl}(\omega)$ for the aforementioned four isotopomer combinations, is shown in Fig. 2.1 for rigid SPC/E water. The corresponding VER lifetimes as obtained with and without the harmonic/Schofield QCF are compared with the corresponding experimental lifetimes(52) in Table 2.1. In the case of rigid SPC/E water, $\tilde{C}_{Cl}(\omega)$ is observed to be monotonically decreasing at high frequencies. Such behavior is characteristic of VER into *intermolecular* accepting modes (i.e. vibration to rotation/translation energy transfer). The VER lifetimes calculated with *rigid SPC/E water* are seen to be in good quantitative agreement with the experimental values for both H_2O and D_2O *when the harmonic/Schofield QCF is used*. In contrast, the lifetimes calculated with *rigid SPC/E water* for both H_2O and D_2O are seen to be an order of magnitude longer than the corresponding experimental values *when no QCF is used* (i.e. when the QCF is set to unity). Those results are consistent with previous studies showing that quantum effects can significantly enhance VER rates in the case of intermolecular accepting modes.(103; 62; 86; 76; 54; 56; 78)

One interesting experimentally observed trend is that the VER lifetimes in H_2O are

Table 2.1: VER lifetimes calculated at 300K using rigid SPC/E water model.

Solvent	Frequency (cm^{-1})	τ_{10} /ps Classical	τ_{10} /ps harmonic/Schofield QCF	τ_{10} /ps Experiment
$^{13}C^{15}N^-$ in D_2O	2004	4275 ± 1968	125 ± 57	120 ± 6
$^{12}C^{14}N^-$ in D_2O	2079	3723 ± 1714	97 ± 45	71 ± 3
$^{13}C^{15}N^-$ in H_2O	2004	876 ± 403	26 ± 12	31 ± 7
$^{12}C^{14}N^-$ in H_2O	2079	1054 ± 485	27 ± 12	28 ± 7

considerably shorter than in D_2O. This trend is reproduced by our rigid SPC/E water simulation results. Since, for a given cyanide isotopomer, the QCF is independent of the water isotopomer, the origin of this trend must be classical. This trend also cannot be attributed to the difference in the frequencies of the intramolecular modes of H_2O and D_2O(75) since the water molecules are treated as rigid. Although an explanation of the underlying mechanism will require a more detailed analysis, the difference is likely related to faster rotational and/or librational motions of H_2O compared to D_2O due to the lighter hydrogen isotope, which may give rise to larger values of $\tilde{C}_{Cl}(\omega)$ at the same C−N stretch frequency.

Another interesting experimental trend is the relative insensitivity of the VER lifetime to the cyanide isotopomer in the case of H_2O, in contrast to the pronounced *decrease* in the lifetime with *increasing* frequency of the C−N stretch in the case of D_2O. Our calculated lifetimes seem to reproduce this trend. However, the fact that the accompanying error bars are larger than the difference in lifetimes between $^{12}C^{14}N^-/D_2O$ and $^{13}C^{15}N^-/D_2O$ make the difference statistically insignificant. Furthermore, it should be noted that since $\tilde{C}_{Cl}(\omega)$ is a monotonically decreasing function of frequency in the case of rigid SPC/E water, the origin of this effect cannot be classical and can therefore only be attributed to the QCF, which does indeed increase between the lower and higher C−N stretch frequencies by a factor of ∼1.2.

In order to gain insight into the role played by electrostatic forces in determining the VER lifetime in the case of rigid SPC/E water, we decomposed the force into its LJ and electrostatic contributions and considered the contributions of LJ-

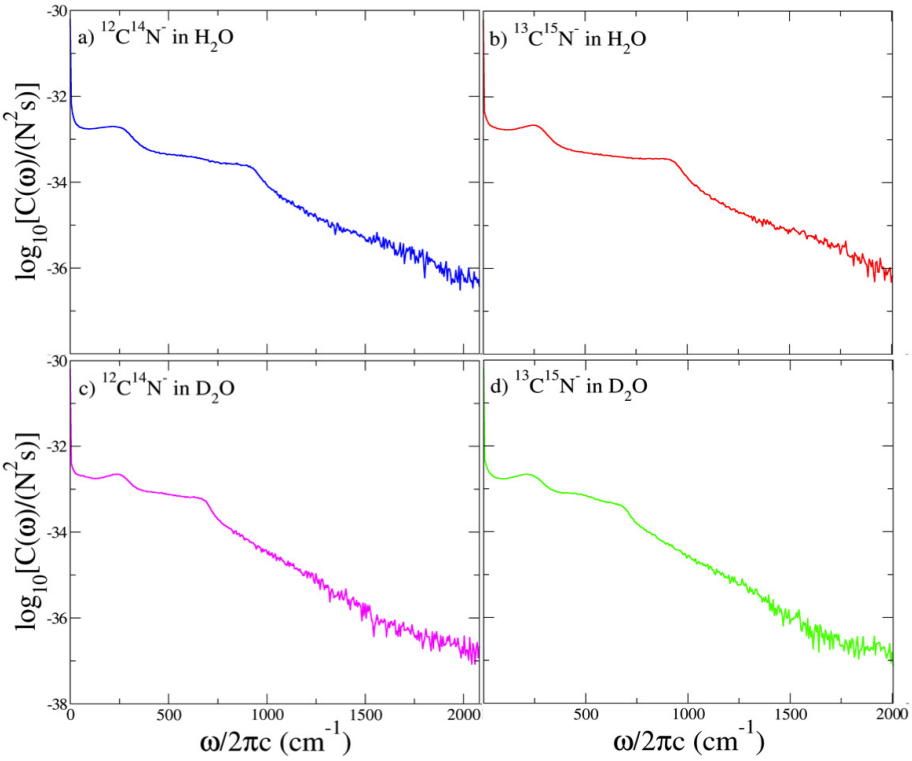

Figure 2.1: A semilog plot of $\tilde{C}^{Cl}(\omega)$ for *rigid SPC/E water* at 300K for all systems. (a) $^{12}C^{14}N^-/H_2O$, (b) $^{13}C^{15}N^-/H_2O$, (c) $^{12}C^{14}N^-/D_2O$, (d) $^{13}C^{15}N^-/D_2O$. The range of the frequency axis is between 0 and the corresponding C−N stretch frequency.

LJ, electrostatic-electrostatic, and LJ-electrostatic cross terms (see Fig. 2.2). At low frequencies, $\tilde{C}^{Cl}(\omega)$ is seen to be dominated by the LJ-LJ contributions for all isotopomer combinations. However, at high frequencies, the contributions of electrostatic-electrostatic and LJ-electrostatic cross terms increase and become either larger than (for H_2O) or comparable to (for D_2O) the LJ-LJ contributions.

The contribution of LJ forces is often attributed to *electrostriction*, which are often found to dominate VER in polar solution.(119) In this case, the attractive electrostatic forces play an indirect role of bringing the solute and solvent closer together, thereby amplifying the effect of LJ short-range repulsive forces to enhance the VER rate constant. While electrostriction does seem to dominate VER at low frequencies for the cyanide/water system, this is no longer true at high frequencies.

Since this trend is observed for a purely classical quantity, $\tilde{C}^{Cl}(\omega)$, its origin must be classical as well. The relatively large contribution of the electrostatic-electrostatic terms is likely due to the stronger electrostatic forces in ionic solutions in comparison to polar solvents.

2.4.2 Flexible SPC/Fw water

We next turn to the case of flexible SPC/Fw water. $\tilde{C}_{Cl}(\omega)$ for the two cyanide isotopomers ($^{12}C^{14}N^-$ and $^{13}C^{15}N^-$) in D_2O and H_2O are shown in Figs. 2.3 and 2.4, respectively. The corresponding VER lifetimes as obtained with and without the standard QCF are compared with the corresponding experimental lifetimes(52) in Table 2.2.

As expected, $\tilde{C}_{Cl}(\omega)$ is non-monotonic even at high frequencies in the case of flexible SPC/Fw water. The resonances in $\tilde{C}_{Cl}(\omega)$ correspond to the existence of *intramolecular* bending, and symmetrical and anti-symmetrical stretching modes of water that can serve as accepting modes. The intramolecular origin of those modes is also consistent with the fact that the frequencies of those resonances are *lower* in

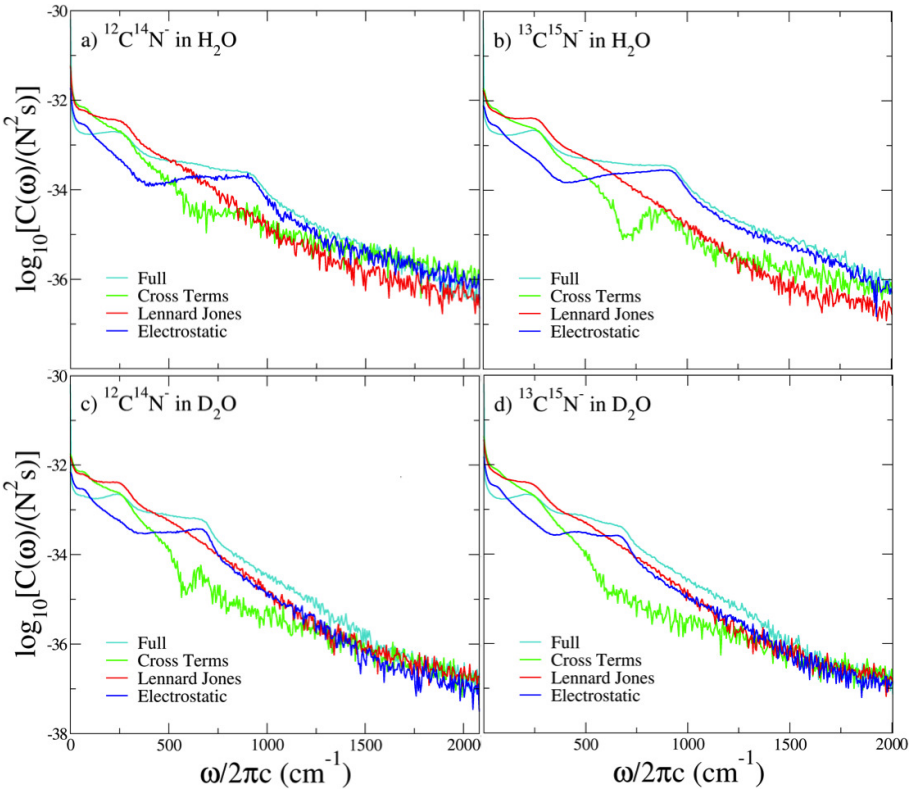

Figure 2.2: A semilog plot of the contributions of the electrostatic-electrostatic, LJ-LJ and LJ-electrostatic cross terms to $\tilde{C}^{Cl}(\omega)$ for *rigid SPC/E water* at 300K. (a) $^{12}C^{14}N^-/H_2O$, (b) $^{13}C^{15}N^-/H_2O$, (c) $^{12}C^{14}N^-/D_2O$, (d) $^{13}C^{15}N^-/D_2O$. The range of the frequency axis is between 0 and the corresponding C−N stretch frequency.

Table 2.2: VER lifetimes calculated at 300K using flexible SPC/Fw water model.

Solvent	Frequency (cm^{-1})	τ_{10} /ps Classical	τ_{10} /ps Standard QCF	τ_{10} /ps Experiment
$^{13}C^{15}N^-$ in D_2O	2004	291 ± 134	146 ± 67	120 ± 6
$^{12}C^{14}N^-$ in D_2O	2079	177 ± 82	88 ± 41	71 ± 3
$^{13}C^{15}N^-$ in H_2O	2004	116 ± 43	58 ± 21	31 ± 7
$^{12}C^{14}N^-$ in H_2O	2079	112 ± 44	56 ± 22	28 ± 7

D_2O than in H_2O. Importantly, these resonances are hundreds of cm^{-1} broad which is indicative of the strong coupling between the intramolecular and intermolecular DOF of water. This extensive broadening also implies that these resonances can still affect the VER of the relaxing mode even when its frequency does not coincide with the central frequency of the intramolecular accepting mode.

The VER lifetimes calculated with *flexible SPC/Fw water* are seen to be in good quantitative agreement with the experimental values in the case of D_2O *when the standard QCF is used*. It should be noted that the standard QCF is significantly smaller than the Harmonic/Schofield QCF, and that as a result quantum effects play a relatively small role in comparison to the case where the accepting modes are intramolecular. It should also be noted that in the case of D_2O, VER of the C−N stretch is seen to be most strongly influenced by the resonances associated with the water stretching modes, whose low frequency wings overlap with the C−N stretch frequency (see insert in Fig. 2.3). The larger overlap with these resonances with increasing C−N stretch frequency is also consistent with the corresponding experimental trend in D_2O.

The VER lifetimes calculated for *flexible SPC/Fw water* with the standard QCF are also in reasonable quantitative agreement with the corresponding experimental values in the case of H_2O. However, it should be noted that, in the case of H_2O, VER of the C−N stretch is seen to be most strongly influenced by the resonance associated with the water bending mode, whose high frequency wing overlaps with the C−N stretch frequency (see insert in Fig. 2.4). However, the water bending mode

resonance appears to be not as broad as the water stretching modes resonances. This is consistent with the experimentally observed insensitivity of the lifetime to the cyanide isotopomer in the case of H_2O as well as with the fact that the agreement between the calculated and experimental lifetimes is not as good as in the case of D_2O (the experimental lifetimes are observed to be shorter than the calculated ones by a factor of $\sim$2). More specifically, the lower overlap with the bending resonance implies that the standard QCF may not be able to fully account for the quantum enhancement of the VER rate, thereby leading to longer VER lifetimes. However, it should also be noted that using the the harmonic/Schofield QCF leads to lifetimes which are an order of magnitude shorter than the corresponding experimental values and therefore clearly overestimate those quantum effects.

The experimental trend according to which VER lifetimes are considerably shorter in H_2O in comparison to D_2O is also reproduced with *flexible SPC/Fw water*. However, its likely origin in this case is the higher efficiency of the water bending mode as an accepting mode in comparison to that of the water stretching modes as accepting modes. This is consistent with the fact that the stretching modes are *higher* in energy than the C$-$N stretch, and would therefore require an *uphill* energy transfer. The latter is less likely than the *downhill* energy transfer associated with VER into the water bending mode whose frequency is *lower* than that of the C$-$N stretch.

2.5 Summary

The cyanide ion in aqueous solution has been established over the last two decades as an important model system for understanding liquid phase VER. Previous computational studies considered either intermolecular or intramolecular accepting modes. Based on treating the solvent classically, most of those studies pointed to VER into intramolecular accepting modes as the dominant pathway. However, the fact that the importance of quantum effects is expected to become larger with increasing frequency

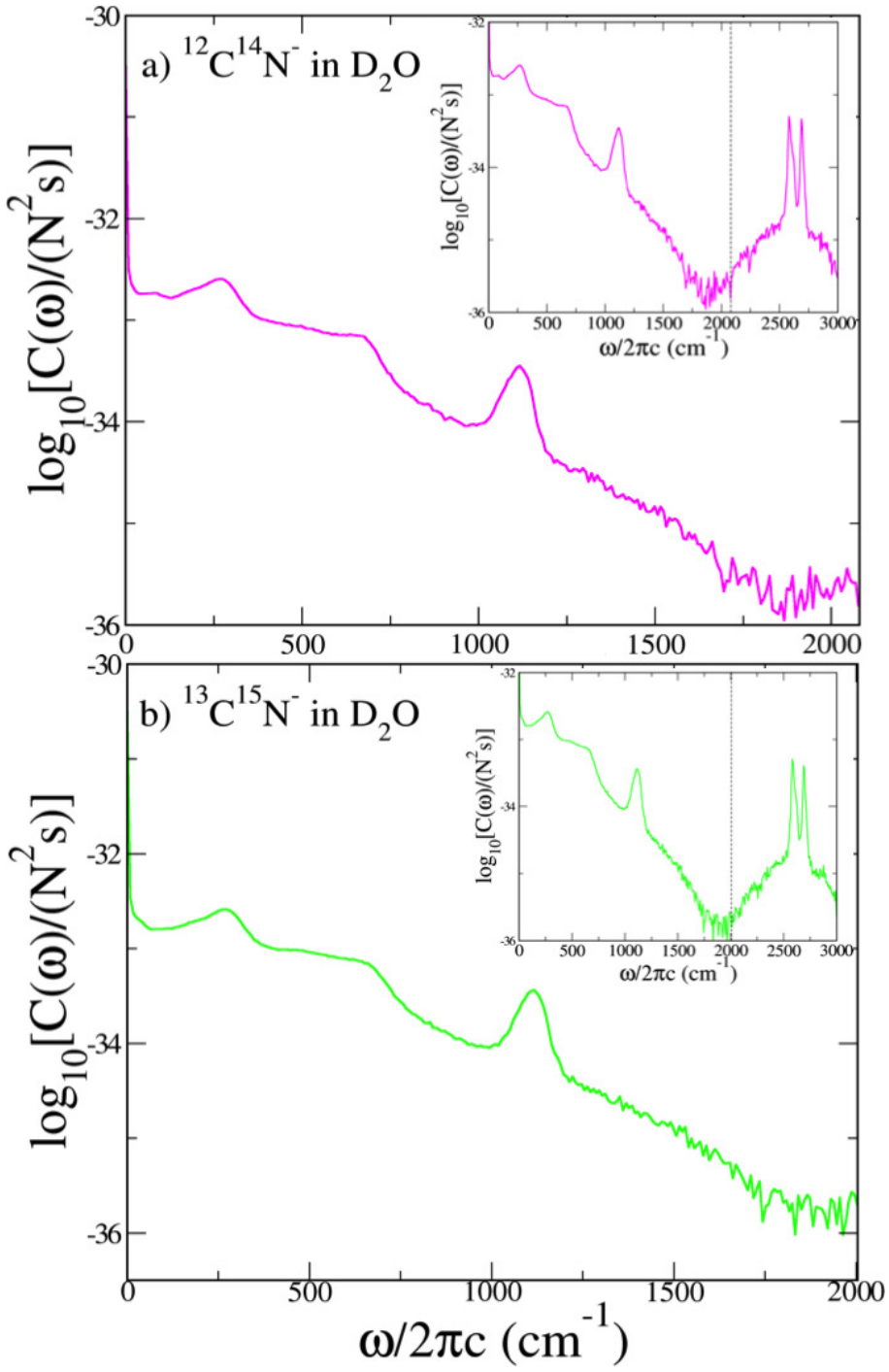

Figure 2.3: A semilog plot of $\tilde{C}^{Cl}(\omega)$ for *flexible SPC/Fw* D_2O at 300K. (a) $^{12}C^{14}N^-/D_2O$, (b) $^{13}C^{15}N^-/D_2O$. The range of the frequency axis is between 0 and the corresponding C−N stretch frequency. The inserts show semilog plots of $\tilde{C}^{Cl}(\omega)$ on a wider frequency range (the vertical dashed lines correspond to the C−N stretch frequency).

mismatch between the relaxing and accepting modes suggests that these effects should be larger in the case of intermolecular accepting modes. Since such quantum effects typically enhance the rate of VER, accounting for them is expected to increase the efficiency of the intermolecular accepting modes relative to that of the intramolecular ones, thereby making their relative efficiencies more comparable. The results reported in this chapter suggest that this is indeed the case.

More specifically, in our research we have shown that whereas a purely classical treatment yields negligibly slow VER rates in the case of a rigid SPC/E water model, accounting for quantum effects via the harmonic/Schofield QCF leads to VER rate constants that are in good agreement with experiment. In addition, we also addressed other aspects of this problem that were either not or partially addressed by previous studies, namely the variation in the VER rate constants with cyanide and water isotopomers, the description of the cyanide ion by a polarizable force field and performing the simulations at concentrations that are comparable to the experimental ones.

It should be noted that our results do not suggest that intramolecular water modes do not play the role of accepting modes, but rather that the intermolecular modes are as likely to play the role of accepting modes. In other words, the picture that emerges is that rather than having one type of accepting modes dominate the other, both types of accepting modes are at play simultaneously. This is particularly relevant for the interpretation of the experimental observation that the VER lifetime becomes shorter when the C−N stretch frequency is increased by changing from $^{13}C^{15}N^-$ to $^{12}C^{14}N^-$ in D_2O. This observation may indeed be explained by invoking the water intramolecular stretches as accepting modes. However, it is enough to have only part of the VER directed to intramolecular accepting modes for this observation to emerge. Our results suggest that intermolecular accepting modes may be as likely.

It should be noted that previous calculations of the VER lifetime of cyanide in

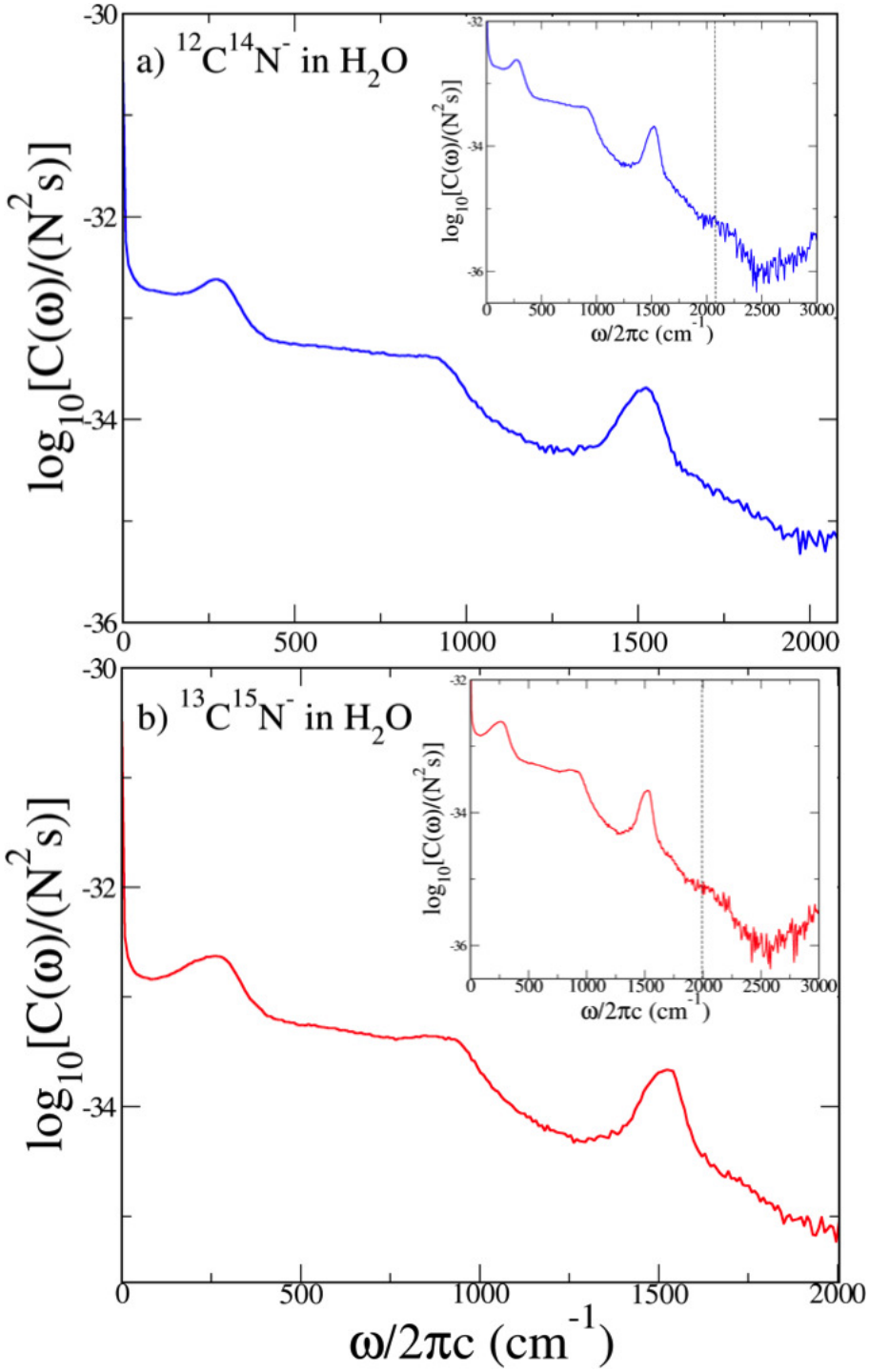

Figure 2.4: A semilog plot of $\tilde{C}^{Cl}(\omega)$ for *flexible SPC/Fw* H_2O at 300K. (a) $^{12}C^{14}N^-/H_2O$, (b) $^{13}C^{15}N^-/H_2O$, The range of the frequency axis is between 0 and the corresponding C−N stretch frequency. The inserts show semilog plots of $\tilde{C}^{Cl}(\omega)$ on a wider frequency range (the vertical dashed lines correspond to the C−N stretch frequency).

aqueous solution relied on the standard QCF, regardless of whether rigid or flexible water models have been used.(59; 71; 73; 68; 66) Furthermore, in cases where rigid water models have been used with the standard QCF, the force fields were often modified in order to achieve agreement with experiment. In contrast, our research shows that the choice of QCF may play an important role in determining the VER lifetime than previously appreciated. More specifically, the quantitative agreement with the experimental values in the present research relies on employing the harmonic/Schofield QCF in the case of intermolecular accepting modes (rigid SPC/E water) and the standard QCF in the case of intramolecular accepting modes (flexible SPC/Fw water). Importantly, the harmonic/Schofield QCF is significantly larger than the standard QCF at the C−N stretch frequency. Thus, whereas a pure classical calculation would suggest that the intramolecular accepting modes are significantly more efficient than the intermolecular accepting modes, the larger QCF associated with the intermolecular accepting modes compensates for the difference, thereby making the intermolecular accepting modes essentially as efficient as the intramolecular ones.

Interestingly, a similar observation can be made for other examples of VER in aqueous solution. For example, the 160 ps VER lifetime of the amide I mode of deuterated *N*-methylacetamide (NMAD) in D_2O, calculated based on a rigid water model and the standard QCF,(120) is significantly longer than the corresponding experimental 5.1 ps lifetime.(121) This result led the authors to conclude that VER occurs via intramolecular vibrational redistribution(120). However, replacing the standard QCF with the harmonic/Schofield QCF reduces the VER lifetime via the intermolecular pathway from 160 ps to 7.63 ps, which is comparable to the experimental value.

The main shortcoming of the present analysis has to do with the fact that accounting for quantum effects by using QCFs is somewhat *ad hoc*. It would therefore

be desirable to confirm the results of our research by employing a more rigorous approach that can account for such quantum effects. Our linearized semiclassical (LSC) method for calculating VER rate constants in condensed phase systems provides such an approach.(122; 86; 62; 56; 54; 76; 78) Preliminary calculations of the VER rate constants for cyanide in water via the LSC method confirm the results based on the harmonic/Schofield QCF presented herein. A complete account of those results are reported in chapter III.

CHAPTER III

Vibrational Energy Relaxation of The Cyanide Ion in Aqueous Solution via the Linearized Semiclassical Method

3.1 Introduction

The cyanide ion in aqueous solution has been established over the last two decades as an important model system(52; 65; 58; 68; 70; 59; 72; 66; 75; 61; 46; 71; 73) for understanding vibrational energy relaxation (VER) in liquid solution.(36; 37; 38; 39; 40; 41; 42; 43; 44; 45; 46; 159; 48; 49; 50; 51; 52; 53; 54; 55; 56; 57; 58; 59; 60; 61; 62; 63; 64; 65; 66; 67; 68; 69; 70; 71; 72; 73; 74; 75; 76; 77; 78) Previous studies suggest that at least two types of accepting modes can play a role in this system, namely: (1) Intermolecular accepting modes, involving translational and rotational degrees of freedom (DOF) of water; (2) Intramolecular accepting modes, involving intramolecular vibrational (bending and stretching) DOF of water. While most studies point to the intramolecular accepting modes as being dominant, this conclusion was reached based on assuming that the solvent can be treated as classical. However, quantum effects are expected to increase in importance with increasing frequency mismatch between the relaxing and accepting modes, thereby suggesting that these effects should be larger in the case of intermolecular accepting modes. Since such quantum effects

typically enhance the rate of VER, accounting for them is expected to increase the efficiency of the intermolecular accepting modes relative to that of the intramolecular ones, thereby potentially making the intermolecular VER pathway into a more viable alternative to the intramolecular one.

In the previous chapter (chapter II, also reported in (123)), we showed that accounting for quantum effects in the case of a rigid SPC/E water model(116) via the harmonic/Schofield quantum-correction factor (QCF)(67; 60) leads to VER lifetimes that are in quantitative agreement with experiment(52) for different cyanide/water isotopomer combinations. It should be noted that the results reported in Ref. (123) do not imply that *intramolecular* water modes cannot play the role of accepting modes. In fact, we also found that the experimental lifetimes can be reproduced equally well by combining a flexible SPC/Fw water model with the standard QCF(123). However, the smaller mismatch between the relaxing and accepting modes in the case of intramolecular accepting modes implies smaller quantum enhancement of VER rates, which is manifested by choice of the standard QCF for intramolecular accepting modes and the harmonic/Schofield QCF for intermolecular accepting modes. In other words, quantum effects are expected to have a much weaker impact on VER rates associated with intramolecular accepting modes in comparison to its effect on VER rates associated with intermolecular accepting modes. Thus, when it comes for understanding quantum effects on VER in this system, one expects the largest impact to be on the intermolecular accepting modes.

The main shortcoming of the analysis in Ref. (123) (or chapter II) has to do with the fact that accounting for quantum effects by using the harmonic/Schofield QCF is somewhat *ad hoc*. Therefore, **our objective in this research is to confirm the results of Ref. (123) (also chapter II) in the case of a rigid water model, where quantum effects are expected to be the strongest, via a more rigorous method for estimating quantum effects**. In a series of recent papers

(87; 62; 86; 76; 54; 56; 63; 78), Geva and co-workers have pursued a rigorous approach for calculating VER rate constants which can account for quantum effects within the framework of the linearized semiclassical (LSC) approximation. This approximation amounts to linearizing the forward-backward action in the exact path-integral expression for the quantum-mechanical force-force correlation function (FFCF) with respect to the difference between the forward and backward paths.(122; 87; 63) The resulting expression for the VER rate constant within the LSC approximation involves a Wigner transform(156) which we proposed can be calculated in a liquid solution by employing a local harmonic approximation (LHA),(122; 63) which amounts to calculating the Fourier transform (FT) underlying the Wigner transform within the instantaneous normal mode approximation.

In this chapter, the results obtained by calculating the lifetimes of the first-excited vibrational state of the cyanide ion isotopomers $^{12}C^{14}N^-$ and $^{13}C^{15}N^-$, dissolved in H_2O or D_2O,within the framework of the Landau-Teller (LT) formula, via the LSC method, are presented. The LSC-based lifetimes are found to be in excellent agreement with the experimental lifetimes for all cyanide/water isotopomer combinations, thereby providing strong support to the view that intermolecular accepting modes do in fact play an important role in the VER of the cyanide ion in water.

The remainder of this chapter is organized as follows. The theory underlying VER lifetime calculations within the framework of LT formula via the LSC method is outlined in Sec. 3.2. Computational techniques and force field parameters are discussed in Sec. 3.3. The results are presented and discussed in Sec. 3.4. A summary of the main results and outlook are provided in Sec. 3.5.

3.2 Theory

In this section a brief outline of the LSC method for calculating VER rate constants (a more detailed discussion is provided in Ref. (63)) is presented. We consider

the following general quantum-mechanical Hamiltonian of a vibrational mode linearly coupled to a bath:

$$\hat{H}_{tot} = \frac{\hat{p}^2}{2\mu} + v(\hat{q}) + \sum_{j=1}^{N} \frac{(\hat{P}^{(j)})^2}{2M^{(j)}} + V(\hat{\boldsymbol{Q}}) - \hat{q}F(\hat{\boldsymbol{Q}}) \ . \tag{3.1}$$

Here, $\hat{q}$, $\hat{p}$, μ, and $v(\hat{q})$ are the relaxing mode coordinate, momentum, reduced mass, and bath-free vibrational potential; $\hat{\boldsymbol{Q}} = \left(\hat{Q}_1, ..., \hat{Q}_N\right)$, $\hat{\boldsymbol{P}} = \left(\hat{P}_1, ..., \hat{P}_N\right)$, $M^{(1)}, ..., M^{(N)}$, and $V(\hat{\boldsymbol{Q}})$ are the coordinates, momenta, masses, and potential energy of the bath DOF; and $F(\hat{\boldsymbol{Q}})$ is the force exerted by the bath on the relaxing mode (quantum operators are designated by $\hat{}$).

The rate constant for population relaxation from the first-excited vibrational state of the relaxing mode to its ground vibrational state, k_{01}, is assumed to be given by the fully quantum-mechanical LT formula.(40; 155) When cast in terms of the fully quantum-mechanical *symmetrized* FFCF,

$$C_s(t) = \frac{1}{Z} Tr\left[e^{-\beta\hat{H}/2}\delta\hat{F}e^{-\beta\hat{H}/2}e^{i\hat{H}t/\hbar}\delta\hat{F}e^{-i\hat{H}t/\hbar}\right] \ , \tag{3.2}$$

the above mentioned population relaxation rate constant is given by

$$k_{01} = \frac{1}{2\mu\hbar\omega_{10}} e^{\beta\hbar\omega_{10}/2}\tilde{C}_s(\omega_{10}) \ . \tag{3.3}$$

Here, $\hat{H} = \sum_{j=1}^{N}\left[(\hat{p}^{(j)})^2/2M^{(j)}\right] + V(\hat{\boldsymbol{Q}})$ is the free bath Hamiltonian, $Z = Tr\left(e^{-\beta\hat{H}}\right)$, $\delta\hat{F} = \hat{F} - Tr\left[e^{-\beta\hat{H}}\hat{F}\right]/Z$, ω_{10} is the transition frequency (i.e. energy gap between the ground and first-excited states divided by $\hbar$) and

$$\tilde{C}_s(\omega) = \int_{-\infty}^{\infty} dt e^{i\omega t} C_s(t) \tag{3.4}$$

is the FT of the symmetrized FFCF.

We also note that in the classical limit, $e^{\beta\hbar\omega_{10}/2}\tilde{C}_s\left(\omega_{10}\right)$ reduces into the FT of the classical FFCF, $\tilde{C}^{Cl}\left(\omega_{10}\right)$, so that Eq. (3.3) reduces into

$$k_{01}^{Cl} = \frac{1}{2\mu\hbar\omega_{10}}\tilde{C}^{Cl}(\omega_{10}) \ . \tag{3.5}$$

Here, $\tilde{C}^{Cl}(\omega) = \int_{-\infty}^{\infty} dt e^{i\omega t} C^{Cl}(t)$, where

$$C^{Cl}(t) = \frac{1}{Z_{cl}} \int\int \mathbf{dQ}_0\mathbf{dP}_0 \exp\left[-\beta H(\mathbf{Q}_0,\mathbf{P}_0)\right] \delta F(\mathbf{Q}_0)\delta F(\mathbf{Q}_t) \tag{3.6}$$

is the *classical* FFCF, with $Z_{cl} = \int\int \mathbf{dQ}_0\mathbf{dP}_0 \exp\left[-\beta H(\mathbf{Q}_0,\mathbf{P}_0)\right]$ and $\mathbf{Q}_t$ is obtained by classical dynamics starting at $(\mathbf{Q}_0,\mathbf{P}_0)$.

A popular approach for accounting for quantum effects is by multiplying the FT of the classical FFCF, by a frequency-dependent quantum correction factor (QCF), $Q(\omega)$ (90; 99; 39; 60; 100; 67; 101; 102; 103; 104; 105; 106; 107; 108; 88; 109; 110):

$$\tilde{C}(\omega) \approx Q(\omega)\tilde{C}^{Cl}(\omega) \ . \tag{3.7}$$

Here, $\tilde{C}(\omega)$ is the FT of the regular (i.e. non-symmetrized) fully quantum-mechanical FFCF:

$$C\left(t\right) = \frac{1}{Z} Tr\left[e^{-\beta\hat{H}}\delta\hat{F}e^{i\hat{H}t/\hbar}\delta\hat{F}e^{-i\hat{H}t/\hbar}\right] \ . \tag{3.8}$$

It should be noted that $\tilde{C}(\omega) = e^{\beta\hbar\omega/2}\tilde{C}_s(\omega)$.

Following a prescription proposed by Skinner and co-workers for choosing the QCF based on the nature of the accepting modes,(67; 60) we previously employed the *harmonic/Schofield QCF* when using a rigid water model for which the accepting modes are *intermolecular* (i.e. solvent translation/rotation DOF) (123):

$$Q_{HS}\left(\omega\right) = e^{\beta\hbar\omega/4}\left(\frac{\beta\hbar\omega}{1-e^{-\beta\hbar\omega}}\right)^{1/2} \ . \tag{3.9}$$

The LSC approximation for $C_s(t)$ is given by(78)

$$C_s^{LSC}(t) = \frac{1}{(2\pi\hbar)^N}\frac{1}{Z}\int d\boldsymbol{Q}_0 \int d\boldsymbol{P}_0 \left[e^{-\beta\hat{H}/2}\delta\hat{F}e^{-\beta\hat{H}/2}\right]_W (\boldsymbol{Q}_0, \boldsymbol{P}_0)\, \delta F\left(\boldsymbol{Q}_t^{Cl}\right) \ . \tag{3.10}$$

Here,

$$A_W(\mathbf{Q},\mathbf{P}) = \int \mathbf{d\Delta} e^{-i\mathbf{P\Delta}/\hbar}\langle \mathbf{Q}+\mathbf{\Delta}/2|\hat{A}|\mathbf{Q}-\mathbf{\Delta}/2\rangle \tag{3.11}$$

is the Wigner transform of the operator $\hat{A}$,(156) and $\mathbf{Q}_t^{(Cl)} = \mathbf{Q}_t^{(Cl)}(\mathbf{Q_0},\mathbf{P_0})$ and $\mathbf{P}_t^{(Cl)} = \mathbf{P}_t^{(Cl)}(\mathbf{Q_0},\mathbf{P_0})$ are propagated *classically* with the initial conditions $\mathbf{Q_0}$ and $\mathbf{P_0}$.

The LSC approximation is known to be *exact* at $t = 0$, at the classical limit, and for harmonic systems. At the same time, it also provides a convenient starting point for introducing computationally feasible schemes to calculate quantum-mechanical time correlation functions. The main disadvantage of the LSC approximation is that it can only capture quantum effects at short times.(124) However, it should be noted that in condensed phase systems in general, and in the case of high-frequency VER in particular, the quantities of interest are often dominated by the behavior of correlation functions at relatively short times.

The main challenge in calculating $C_s^{LSC}(t)$ lies in the evaluating the following Wigner transform:

$$\left[e^{-\beta\hat{H}/2}\delta\hat{F}e^{-\beta\hat{H}/2}\right]_W (\boldsymbol{Q}_0,\boldsymbol{P}_0) = \int d\Delta e^{-iP_0\Delta/\hbar}\left\langle \boldsymbol{Q}_0 + \frac{\Delta}{2}\left|e^{-\beta\hat{H}/2}\delta\hat{F}e^{-\beta\hat{H}/2}\right|\boldsymbol{Q}_0 - \frac{\Delta}{2}\right\rangle \tag{3.12}$$

Evaluating the latter within the LHA as shown in Ref. (63) leads to the following

LHA-LSC working expression for $C_s(t)$:

$$C_s^{LHA-LSC}(t) = \int d\boldsymbol{Q}_0 \int d\boldsymbol{Q}' \frac{\left\langle \boldsymbol{Q}_0 \mid e^{-\beta\hat{H}/2} \mid \boldsymbol{Q}' \right\rangle \left\langle \boldsymbol{Q}' \mid e^{-\beta\hat{H}/2} \mid \boldsymbol{Q}_0 \right\rangle}{Z}$$
$$\int d\boldsymbol{P}_n \prod_{j=1}^{N} \left(\frac{1}{\alpha^{(j)} \pi \hbar^2} \right)^{1/2} \exp\left[-\frac{\left(P_n^{(j)}\right)^2}{\hbar^2 \alpha^{(j)}} \right] \times \delta F\left(\boldsymbol{Q}'\right) \delta F\left(\boldsymbol{Q}_t^{Cl}\left[\boldsymbol{Q}_0, \boldsymbol{P}_0\right]\right) \tag{3.13}$$

Here, $P_n = P_n\left(Q'\right)$ are the normal mode momenta that emerge from diagonalizing the Hessian matrix underlying the quadratic expansion of the free bath potential energy around $Q = Q'$ and

$$\alpha^{(j)} = \alpha^{(j)}\left(Q'\right) = \frac{\Omega^{(j)}\left(Q'\right)}{\hbar} \coth\left[\frac{\beta\hbar\Omega^{(j)}\left(Q'\right)}{2} \right] , \tag{3.14}$$

where $(\Omega^{(k)})^2(Q')$ are the eigenvalues of the Hessian matrix.

It should also be noted that quantum effects are accounted for in several ways within the LHA-LSC method:

1. Nonclassical sampling of bath coordinates and momenta.

2. The initial force, $\delta F(\mathbf{Q}')$, is not calculated at the initial position, $\mathbf{Q}_0$, used to generate the classical trajectory leading to the force at a later time t, $\delta F(\mathbf{Q}_t^{Cl}[\mathbf{Q_0},\mathbf{P_0}])$.

3. The factor $e^{\beta\hbar\omega_{10}/2}$ (see Eq. (3.3)), which actually coincides with the so-called Schofield QCF.(88)

3.3 Computational Methods

MD simulations were performed using the AMBER 10 software package for four different isotopomer combinations: $^{12}C^{14}N^-/H_2O$, $^{13}C^{15}N^-/H_2O$, $^{12}C^{14}N^-/D_2O$, $^{13}C^{15}N^-/D_2O$. Simulations were performed using a cubical simulation box with periodic boundary

conditions, containing 9 CN^- anions and 9 K^+ cations dissolved in 605 rigid water molecules, at a temperature of 300K and pressure of 1.0atm. The time step was set to 1.0fs. It should be noted that these concentrations are comparable to the experimental concentrations (0.22-0.90M) (52).

The force fields used were the same as those employed in Ref. (123), where the classical and harmonic/Schofield QCF results for the same model systems were reported. Briefly, the interaction between cyanide and water were modeled in terms of the AMBER polarizable force field *ff02*.(111) The partial charges for CN^- were assigned using the restrained electrostatic potential (RESP)(112; 243; 242) method where the electrostatic potential is generated via Gaussian 09, at the HF/6-31G* level. The partial charges for C and N thus obtained are q_C=-0.216698 and q_N=-0.783302, respectively. The atomic polarizabilities for the C, N and K atoms were set as 0.36 A^3, 0.53 A^3, and 1.06 A^3 respectively. The SPC/E force field(116) was employed for modeling *rigid* water intermolecular accepting modes, where the rigidity was imposed by the SHAKE algorithm.(247)

The calculation of $C_s^{LHA-LSC}(t)$, Eq. (3.13), starts out by performing an imaginary-time path integral molecular-dynamics (PIMD) simulation(157; 158) in order to sample the initial configuration, $\boldsymbol{Q}_0$, and the configuration at which the initial force is calculated, $\boldsymbol{Q}^{'}$. It should be noted that within the context of a PIMD simulation, each atom is represented by a ring polymer that consists of P beads labeled $0, 1, 2, ..., P-1$. Assuming that P is even, $\boldsymbol{Q}_0$ is identified with the configuration of the beads labeled 0, while $\boldsymbol{Q}^{'}$ is identified with the configuration of the beads labeled $P/2$ (i.e. half a ring away). In the next step, a local harmonic expansion is performed around $\boldsymbol{Q}^{'}$, to obtain the normal-mode frequencies, $\Omega^{(k)}$, and $\alpha^{(k)}$, required for sampling the initial (normal-mode) momenta, $P_n^{(k)}$. Once the initial positions and momenta are determined, $\boldsymbol{Q}_t^{Cl}$ is calculated via a classical MD simulation for each sampled initial configuration $\boldsymbol{Q}_0$ and normal mode momenta $\boldsymbol{P}_{n,0}$. Finally, the LHA-LSC FFCF is

obtained by correlating $\delta F(\boldsymbol{Q}_t^{Cl})$ with $\delta F(\boldsymbol{Q}^{'})$. PIMD simulations were performed with 32 beads per degree of freedom. Each FFCF is averaged over $\sim 400,000$ trajectories of 4 ps length each.

In the absence of resonance with other vibrations, one expects $\tilde{C}_s^{LHA-LSC}(\omega)$ to follow an exponential gap law, i.e. decay asymptotically with frequency in an exponential manner. As a result, it is not computationally feasible to average out the statistical noise in order to calculate the increasingly small value of $\tilde{C}_s^{LHA-LSC}(\omega)$ at the actual frequency of the C-N stretch. We therefore resort to estimating $\tilde{C}_s^{LHA-LSC}(\omega)$ at high frequencies by extrapolation of the exponential gap law that emerges at lower frequencies.(172; 173)

The total number of trajectories over which the rate constant was averaged varies from 384,600 to 705,100 (each trajectory being 4 ps long). The error associated with the rate constant was calculated by dividing the total number of trajectories into 6 to 11 equal blocks, and calculating the standard deviation associated with the data.

3.4 Results

$\tilde{C}_s^{LHA-LSC}(\omega)$ for the aforementioned four isotopomer combinations, are shown in Fig. 3.1. The corresponding VER lifetimes obtained either purely classical (Eq. (3.5)),(123) with harmonic/Schofield QCF (Eqs. (3.7)(123) and (3.9)) and via LSC (Eqs. (3.3) and (3.13)) are compared with the corresponding experimental lifetimes(52) in Table 3.1.

Table 3.1: VER lifetimes calculated at 300K using rigid SPC/E water model. Classical and harmonic/Schofield QCF results are adopted from Ref. (123). Experimental results are taken from Ref. (52).

Solute/ Solvent	Frequency (cm^{-1})	τ_{10} /ps Classical	τ_{10} /ps harmonic/ Schofield QCF	τ_{10} /ps LHA-LSC	τ_{10} /ps Experiment
$^{13}C^{15}N^-/D_2O$	2004	4275 ± 1968	125 ± 57	110 ± 13	120 ± 6
$^{12}C^{14}N^-/D_2O$	2079	3723 ± 1714	97 ± 45	67 ± 9	71 ± 3
$^{13}C^{15}N^-/H_2O$	2004	876 ± 403	26 ± 12	29 ± 3	31 ± 7
$^{12}C^{14}N^-/H_2O$	2079	1054 ± 485	27 ± 12	28 ± 3	28 ± 7

The VER lifetimes calculated via LHA-LSC are seen to be in very good quantitative agreement with the experimental values for both H_2O and D_2O. The LHA-LSC-based VER lifetimes are also seen to be in good agreement with the lifetimes obtained by using the harmonic/Schofield QCF. This should be contrasted with the corresponding classical lifetimes, which are seen to be an order of magnitude longer than the corresponding experimental values. Those results are consistent with previous studies and support the view that quantum effects can significantly enhance VER rates in the case of intermolecular accepting modes.(103; 62; 86; 76; 54; 56; 78)

One interesting experimentally observed trend is that the VER lifetimes in H_2O are considerably shorter than in D_2O. This trend is reproduced by the LHA-LSC-based lifetimes, and can be traced back to the fact that $\tilde{C}_s^{LHA-LSC}(\omega)$ in D_2O is smaller than that in H_2O. It should also be noted that the fact that the fully classical result show the same trend and the harmonic/Schofield or Schofield QCFs are insensitive to whether the solvent is H_2O or D_2O, it is likely that the origin of this trend is classical.

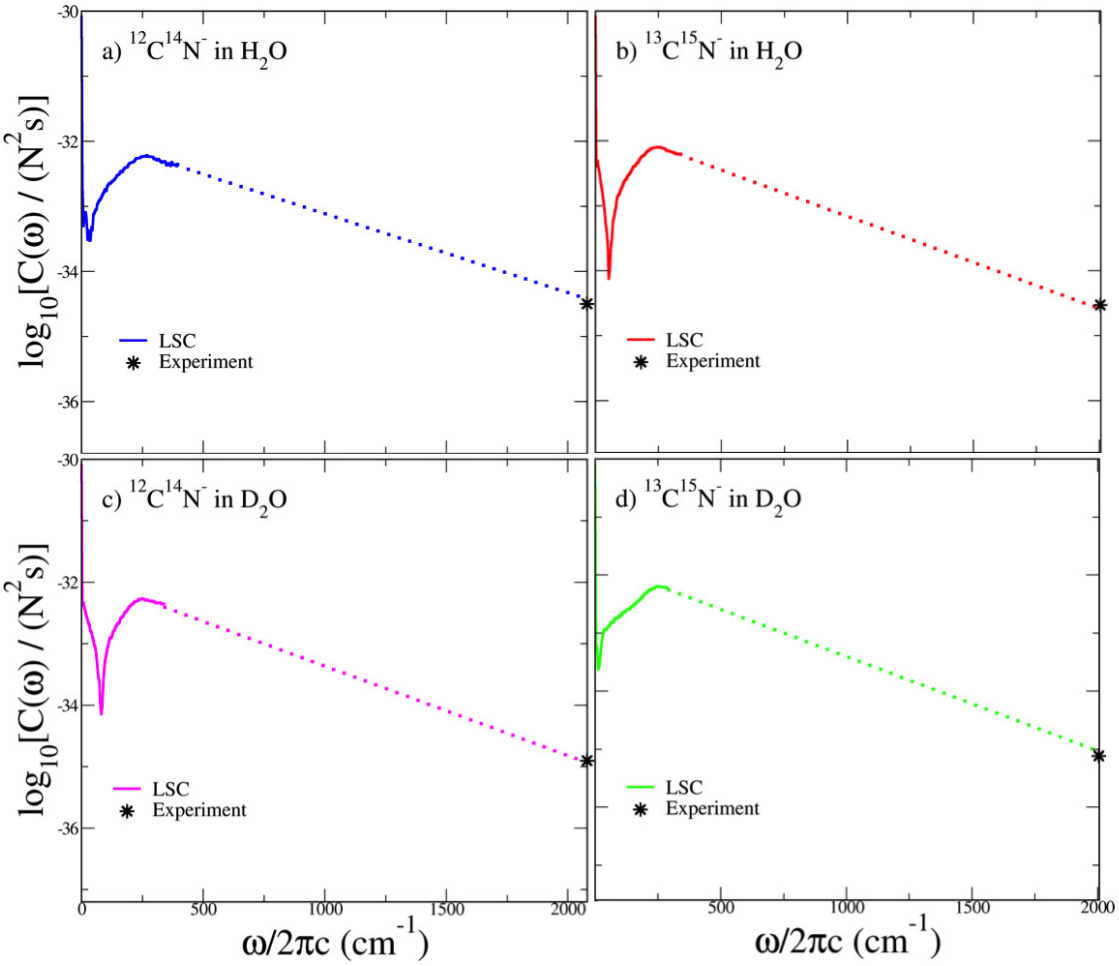

Figure 3.1: A semilog plot of $\tilde{C}_s^{LHA-LSC}(\omega)$ for *rigid SPC/E water* at 300K. (a) $^{12}C^{14}N^-/H_2O$, (b) $^{13}C^{15}N^-/H_2O$, (c) $^{12}C^{14}N^-/D_2O$, (d) $^{13}C^{15}N^-/D_2O$. The range of the frequency axis is between 0 and the corresponding C−N stretch frequency. Solid lines correspond to simulation data and dotted lines to extrapolations. The star indicate the experimental corresponding value.

Another interesting experimental trend is the relative insensitivity of the VER lifetime to the cyanide isotopomer in the case of H_2O, in contrast to the pronounced *decrease* in the lifetime with *increasing* frequency of the C−N stretch in the case of D_2O. The LHA-LSC-based lifetimes reproduce this trend rather well. The origin of this trend in the calculated lifetimes can be traced back to the $\exp(\beta\hbar\omega/2)$ factor (see Eq. (3.3)), which increase between the lower and higher C−N stretch frequencies by a factor of $\sim$1.2.

In order to gain insight into the role played by electrostatic forces in determining the VER lifetime, we decomposed the force into its LJ and electrostatic contributions and considered the contributions of LJ-LJ, electrostatic-electrostatic, and LJ-electrostatic cross terms (see Fig. 3.2). At low frequencies, $\tilde{C}_s^{LHA-LSC}(\omega)$ is seen to be dominated by the LJ-LJ contributions for all isotopomer combinations. However, while the LJ-electrostatic cross terms drops until its becomes negligibly small at high frequencies, the contributions of electrostatic-electrostatic terms increase and become more comparable to the LJ-LJ contributions.

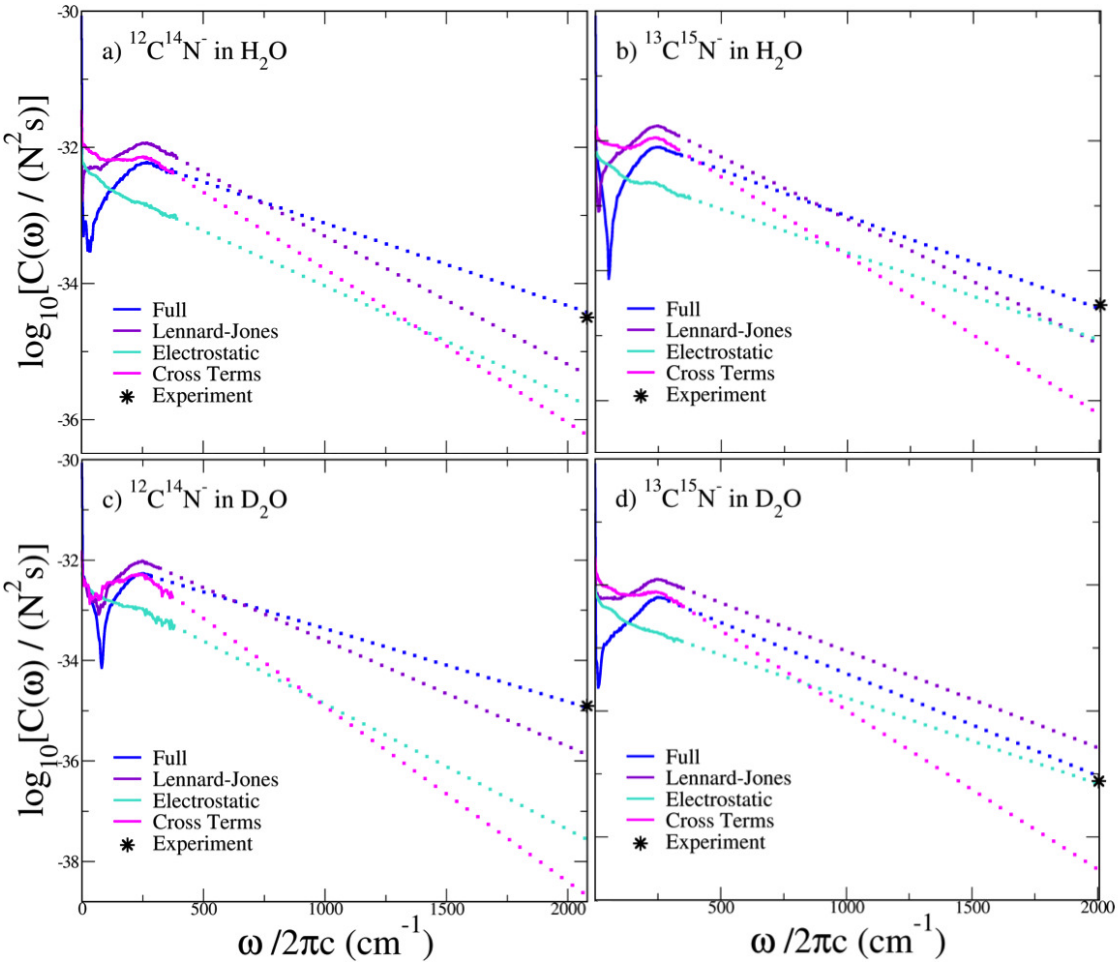

Figure 3.2: A semilog plot of the contributions of the electrostatic-electrostatic, LJ-LJ and LJ-electrostatic cross terms to $\tilde{C}_s^{LHA-LSC}(\omega)$ for *rigid SPC/E water* at 300K for all systems studied. (a) $^{12}C^{14}N^-/H_2O$, (b) $^{13}C^{15}N^-/H_2O$, (c) $^{12}C^{14}N^-/D_2O$, (d) $^{13}C^{15}N^-/D_2O$. The range of the frequency axis is between 0 and the corresponding C−N stretch frequency. Solid lines correspond to simulation data and dotted lines to extrapolations. The star indicate the experimental corresponding value.

The contribution of LJ forces is often attributed to *electrostriction*, which are often found to dominate VER in polar solution.(119) In this case, the attractive electrostatic forces play an indirect role of bringing the solute and solvent closer together, thereby amplifying the effect of LJ short-range repulsive forces to enhance the VER rate constant. While electrostriction dominate VER at low frequencies for the cyanide/water system under consideration here, this appears to be no longer the case at high frequencies. Since this trend is also observed for a purely classical quantity, $\tilde{C}^{Cl}(\omega)$, its likely origin is classical and due to the stronger electrostatic forces in ionic solutions in comparison to polar solvents.

3.5 Summary

The cyanide ion in aqueous solution has been established over the last two decades as an important model system for understanding liquid phase VER. In a previous paper(123) (also discussed in chapter II) we showed that whereas a purely classical treatment yields negligibly slow VER rates in the case of a rigid SPC/E water model, accounting for quantum effects via the harmonic/Schofield QCF led to VER rate constants that are in good agreement with experiment. However, the fact that accounting for quantum effects by using QCFs is somewhat *ad hoc* made it desirable to confirm the results of Ref. (123) via a more rigorous approach which is capable of accounting for quantum effects. In this study we have used our LHA-LSC to this end. Our results show that the LSC-LHA-based VER lifetimes are consistent with those based on using harmonic/Schofield QCF, and that both reproduce the experimental lifetimes as well as their dependence on the cyanide and water isotopomers.

It should be noted that while the the point charge model for cyanide and the nonpolarizable water model used in this study and in Ref. (123) may be somewhat oversimplified, the quantum enhancement of VER lifetimes appears to have a bigger effect on the VER lifetimes than a variation of force fields would typically

have. Thus, our main result that accounting for quantum effects, either via QCFs or LSC-LHA, significantly shortens the VER lifetimes associated with intermolecular accepting modes, can be considered to be independent of the choice of force fields. Nevertheless, a natural next step would be to combine the LHA-LSC method with an electrostatic model of the kind described in Ref. (75) and a polarizable water model in order to obtain further insight into VER in this system.

CHAPTER IV

Vibrational energy relaxation in liquid HCl and DCl via the linearized semiclassical method: Electrostriction vs. quantum delocalization

4.1 Introduction

Virtually all chemical phenomena involve vibrational energy relaxation (VER) processes. As a result, the measurement and calculation of VER rates have received much attention over the last few decades.(127; 128; 90; 129; 130; 131; 132; 36; 37; 133; 134; 135; 43; 40; 38; 136; 137; 138; 46; 139; 49; 140; 141; 50; 142; 143; 144; 145; 146; 147; 41; 42; 148; 149; 150; 151; 152; 153; 69; 52; 64; 44; 45; 154) Recent theoretical and computational studies of VER have been mostly based on the Landau-Teller (LT) formula,(40; 155) which gives the VER rate constant in terms of the Fourier transform (FT), at the vibrational transition frequency, of the *quantum-mechanical* autocorrelation function of the fluctuating force exerted on the relaxing mode by the other degrees of freedom (DOF), i.e. the bath.

Importantly, replacing the quantum-mechanical force-force correlation function (FFCF) by its classical counterpart can only be justified in cases where the vibrational transition frequency is significantly smaller than $k_B T/\hbar$. (66; 82; 83; 81; 80) In a series of recent papers,(87; 62; 86; 76; 54; 56) we have pursued a rigorous approach

for calculating VER rate constants which can account for quantum effects within the framework of the linearized semiclassical (LSC) approximation. This approximation amounts to linearizing the forward-backward action in the exact path-integral expression for the quantum-mechanical FFCF with respect to the difference between the forward and backward paths.(122) The resulting expression for the VER rate constant within the LSC approximation involves a Wigner transform(156) of the form $\left(\exp[-\beta\hat{H}]\hat{F}\right)_W(\mathbf{Q},\mathbf{P})$, where $\beta = 1/k_BT$, $\hat{H}$ is the bath Hamiltonian operator, $\hat{F}$ is the bath-induced force operator and $(\mathbf{Q},\mathbf{P})$ are the classical-like bath positions and momenta. The calculation of this Wigner transform is highly challenging in the case of a many-body anharmonic system like a molecular liquid. Thus, in practice, we have calculated it by employing a local harmonic approximation (LHA), which amounted to calculating the FT underlying the Wigner transform within the instantaneous normal mode approximation. Importantly, our implementation of the LHA only affects the sampling of bath initial momenta while the sampling of bath initial positions is still done in a quantum-mechanically exact manner via imaginary-time path-integral simulations(157; 158) which are based on the exact anharmonic force-fields.

The applicability and reliability of the resulting LHA-LSC method have been previously demonstrated on a variety of nonpolar systems, including liquid O_2(62; 86), liquid N_2,(62; 86) O_2/Ar liquid mixtures,(86) H_2 dissolved in liquid Ar(56) and CX_2 (X=O,S,Se) dissolved on liquid Ar and Ne.(76; 54) However, extending the range of applicability to more complex systems has proven cumbersome due to the fact that calculating the standard FFCF within LHA-LSC requires force derivatives as input. In an effort to overcome this obstacle, we have recently introduced a new force-derivative-free computational scheme for calculating VER rate constants within LHA-LSC.(63) The new scheme is based on applying the LSC approximation to the *symmetrized* FFCF. Unlike the previous scheme(122) which was based on applying LSC to the standard FFCF, the new scheme does not involve a power expansion

of the initial force in terms of the Wigner transform integration variable $\mathbf{\Delta}$ and as a result is more accurate and does not require force derivatives as input (for more details see Sec. 4.2).(63) In Ref. (63), we have tested the new scheme by using it to calculate VER rates in the case of liquid O_2 and liquid N_2 and comparing them to the experimental rates as well as the rates obtained within the original scheme. Avoiding the calculation of force derivatives would be particularly advantageous in applications to more complex systems governed by various types of force fields. In our research, we take a first step in this direction by presenting the first ever application of the LHA-LSC method to a polar liquid.

VER rates in polar solutions have received much attention over the last several decades. The central role played by electrostatic interactions in enhancing VER rates has already been demonstrated in early measurements performed on neat heteronuclear diatomic liquids.(48; 159) For example, the VER life-time for neat liquid HCl, which is a few nanoseconds long,(48) becomes as long as $1.3\mu s$ when HCl is diluted in a nonpolar solvent like Xenon.(142) A related class of systems that received much attention corresponds to molecular ions in polar solvents. For example, the VER life-time of CN^- infinitely diluted in aqueous solutionwas found to be as short as $\sim 30ps$.(46; 52)

The wealth of detailed experimental information on VER in polar liquid solutions has motivated many theoretical studies that attempted to provide a molecular interpretation of the VER rate enhancement.(64; 154; 160; 161; 84; 162; 85; 163; 55; 53; 164; 165; 59; 166; 167; 168) However, most of those theoretical studies were based on classical molecular dynamics (MD) simulations, although a few have also attempted to account for quantum-mechanical effects by using quantum corrections factors (QCFs).(64; 67; 53) The first computational study of VER in a polar solution was carried out by Whitnell et al. on CH_3Cl (treated as an effective diatom with a frequency of $\sim 680cm^{-1}$) in water.(160; 161) The calculated VER life-time of $5ps$, as

obtained from either nonequilibrium classical MD simulations or via the LT formula, is similar to the experimentally observed VER rates in polar solutions. It was also found that the calculated VER rate decreased by at least one order of magnitude in the absence of electrostatic interactions, which is consistent with the view that strong electrostatic interactions can significantly enhance the VER rate. Similar classical calculations of VER rates were performed on many other systems, including I_2^- in water and ethanol(84), a hydrogen bonded complex (A-H $\cdots$ B) in an aprotic dipolar liquid,(162) HgI in ethanol,(85) OClO in water,(163) HOD in D_2O,(55; 64; 53), CN^- in water(59), azide in water,(164; 165) neat liquid chloroform,(154) neat liquid methanol,(166; 167) and HF in water.(168)

Several different arguments have been invoked for explaining the enhancement of VER rates in polar solutions. For example, in the case of aqueous solutions, it appears that the VER rate acceleration is at least partially due to the high density of states in the (700-800) cm^{-1} frequency range, which is attributed to collective librational modes. This leads to rapid VER in cases where the frequency of the relaxing mode overlaps this range (e.g. in the case of CH_3Cl)(160; 161). At the same time, the enhanced VER rate in the case of I_2^- in water is believed to be due to the significantly lower vibrational frequency of I_2^- (in comparison to I_2), rather than the stronger solute-solvent interactions.(84; 169; 170)

However, such arguments cannot explain the relatively rapid VER rates in a system like liquid HCl where VER presumably occurs by energy exchange between a high-frequency H-Cl stretch ($2783cm^{-1}$) and a multitude of low frequency rotational and translational accepting modes. Ladanyi and Stratt have argued, based on classical MD simulations involving a dipolar solute in aprotic polar solvents, that the enhancement of the VER rate by electrostatic forces in such cases can be attributed to a phenomenon they referred to as *electrostriction*.(119) More specifically, the attractive Coulombic forces bring the solute and solvent closer together, thereby amplifying the

effect of non-Coulombic short-range repulsive forces. The fact that these repulsive forces are sharply varying can then lead to a rather dramatic enhancement of the VER rate.

As mentioned above, treating VER within the framework of classical mechanics is reasonable in cases like I_2^- and HgI, where $\beta\hbar\omega \leq 1$. Indeed, the VER life-time of 1.3ps measured for I_2^- in water(143) compares relatively well with the 0.6ps life-time predicted from classical simulations.(84) The same is true in the case of HgI in ethanol where the experimental VER life-time of 3ps(145) compares well with the classical prediction of 2ps.(85) However, for the intermediate frequency molecule ClO^- ($\sim$ 700 cm^{-1}), one starts observing significant deviations between the measured VER life-time of $(1-7)$ps(171) and the classical predictions of $(0.2-0.6)$ps(171; 169) The reliability of the classical treatment becomes even more questionable in cases such as HCl and CN^-, where $\beta\hbar\omega \gg 1$. Furthermore, our previous work has shown that a major contribution to the quantum enhancement of the VER rate in nonpolar solutions comes from the fact that quantum delocalization allows the system to sample regions of configuration space where the repulsive forces are stronger.(87; 62; 86) At the same time, classical MD simulations suggests that the enhancement of the VER rate by electrostatic forces results from electrostriction, which also leads to enhanced sampling in regions of configuration space where non-electrostatic repulsive forces are stronger.(169; 119)

Thus, **our goal in this research is to elucidate the intriguing interplay between quantum delocalization and electrostriction in the case of liquid HCl, which has been chosen because of its high frequency (2783 cm^{-1}) and the fact that experimental VER rates are available for it(48).**

The remainder of this chapter is organized as follows. The force-derivative-free LHA-LSC method is briefly outlined in Sec. 4.2. The model for liquid HCl and simulation techniques are outlined in Sec. 4.3. The results are reported and discussed

in Sec. 4.4. The main conclusions are summarized in Sec. 4.5.

4.2 The force-derivative-free LHA-LSC method

In this section we provide a brief outline of the force-derivative-free LHA-LSC method (see Ref. (63) for a more detailed discussion). To this end, we consider the following general quantum-mechanical Hamiltonian of a vibrational mode linearly coupled to a bath:

$$\hat{H}_{tot} = \frac{\hat{p}^2}{2\mu} + v\left(\hat{q}\right) + \sum_{j=1}^{N} \frac{(\hat{P}^{(j)})^2}{2M^{(j)}} + V\left(\hat{\mathbf{Q}}\right) - \hat{q}F\left(\hat{\mathbf{Q}}\right) \ . \tag{4.1}$$

Here, $\hat{q}$, $\hat{p}$, μ and $v\left(\hat{q}\right)$ are the relaxing mode coordinate, momentum, reduced mass and bath-free vibrational potential; $\hat{\mathbf{Q}}$, $\hat{\mathbf{P}}$, $\left\{M^{(1)}, ..., M^{(N)}\right\}$ and $V\left(\hat{\mathbf{Q}}\right)$ are the coordinates, momenta, masses and potential energy of the bath DOF and $F\left(\hat{\mathbf{Q}}\right)$ is the potential force exerted by the bath on the relaxing mode.

The LT formula for the population relaxation rate constant between the first-excited and ground vibrational states can then be given by the following expression:(63)

$$k_{10} = \frac{1}{2\mu\hbar\omega_{10}} e^{\beta\hbar\omega_{10}/2} \tilde{C}_s(\omega_{10}) \ . \tag{4.2}$$

Here, ω_{10} is the transition frequency and

$$\tilde{C}_s(\omega) = \int_{-\infty}^{\infty} dt e^{i\omega t} C_s(t) \tag{4.3}$$

is the FT of the *symmetrized* quantum-mechanical FFCF

$$C_s(t) = \frac{1}{Z} Tr\left[e^{-\beta\hat{H}/2}\delta\hat{F}e^{-\beta\hat{H}/2}e^{i\hat{H}t/\hbar}\delta\hat{F}e^{-i\hat{H}t/\hbar}\right] \ , \tag{4.4}$$

where $\hat{H} = \sum_{j=1}^{N} \frac{(\hat{P}^{(j)})^2}{2M^{(j)}} + V\left(\hat{\mathbf{Q}}\right)$ is the bath Hamiltonian, $Z = Tr\left(e^{-\beta\hat{H}}\right)$ is the canonical bath partition function and $\delta\hat{F} = \hat{F} - Tr\left[e^{-\beta\hat{H}}\hat{F}\right]/Z$. We also note that in the classical limit, $e^{\beta\hbar\omega_{10}/2}\tilde{C}_s(\omega_{10})$ reduces into the FT of the classical FFCF, $\tilde{C}^{Cl}(\omega_{10})$, so that Eq. (4.2) reduces into:

$$k_{10}^{Cl} = \frac{1}{2\mu\hbar\omega_{10}}\tilde{C}^{Cl}(\omega_{10})\ g. \tag{4.5}$$

The LSC approximation for $C_s(t)$ is given by:(87; 63)

$$C_s^{LSC}(t) = \frac{1}{(2\pi\hbar)^N}\frac{1}{Z}\int \mathbf{dQ_0}\int \mathbf{dP_0}\left[e^{-\beta\hat{H}/2}\delta\hat{F}e^{-\beta\hat{H}/2}\right]_W(\mathbf{Q_0},\mathbf{P_0})\,\delta F\left(\mathbf{Q}_t^{Cl}\right)\ , \tag{4.6}$$

where $\mathbf{Q}_t^{Cl}$ is obtained by classical dynamics with $\mathbf{Q}_0$ and $\mathbf{P}_0$ as the initial conditions. It should be noted that the LSC approximation only accounts for quantum effects in the initial sampling and not the subsequent dynamics. The accuracy of the LSC approximation, despite its inability to account for the quantum nature of the underlying dynamics, is attributed to the fact that the high frequency FT of the FFCF is dominated by the short time behavior of the correlation function, which is in turn dominated by the initial sampling.

The main challenge in calculating $C_s^{LSC}(t)$ lies in evaluating the following Wigner transform:

$$\begin{aligned}&\left[e^{-\beta\hat{H}/2}\delta\hat{F}e^{-\beta\hat{H}/2}\right]_W(\mathbf{Q_0},\mathbf{P_0})\\ =\ &\int d\mathbf{\Delta}e^{-i\mathbf{P}_0\mathbf{\Delta}/\hbar}\left\langle \mathbf{Q}_0+\frac{\mathbf{\Delta}}{2}\right|e^{-\beta\hat{H}/2}\delta\hat{F}e^{-\beta\hat{H}/2}\left|\mathbf{Q}_0-\frac{\mathbf{\Delta}}{2}\right\rangle.\end{aligned} \tag{4.7}$$

Evaluating the latter within the LHA as shown in Ref. (63) leads to the following LHA-LSC approximation for $C_s(t)$:

$$C_s^{LHA-LSC}(t) = \int d\mathbf{Q_0} \int d\mathbf{Q}' \frac{\langle \mathbf{Q}_0 | \, e^{-\beta \hat{H}/2} \, | \mathbf{Q}' \rangle \, \langle \mathbf{Q}' | \, e^{-\beta \hat{H}/2} \, | \mathbf{Q}_0 \rangle}{Z}$$
$$\int d\mathbf{P_n} \prod_{j=1}^{N} \left(\frac{1}{\alpha^{(j)} \pi \hbar^2} \right)^{1/2} \exp \left[- \frac{(P_n^{(j)})^2}{\hbar^2 \alpha^{(j)}} \right] \times$$
$$\delta F(\mathbf{Q}') \delta F(\mathbf{Q}_t^{Cl}[\mathbf{Q_0}, \mathbf{P_0}]) \tag{4.8}$$

Here, $\mathbf{P}_n = \mathbf{P}_n(\mathbf{Q}')$ are the normal mode momenta that emerge from diagonalizing the Hessian matrix underlying the quadratic expansion of the bath potential energy around $\mathbf{Q} = \mathbf{Q}'$ and

$$\alpha^{(j)} = \alpha^{(j)}(\mathbf{Q}') = \frac{\Omega^{(j)}(\mathbf{Q}')}{\hbar} \coth \left[\frac{\beta \hbar \Omega^{(j)}(\mathbf{Q}')}{2} \right] , \tag{4.9}$$

where $\{(\Omega^{(k)})^2(\mathbf{Q}')\}$ are the eigenvalues of the Hessian matrix.

It should be noted that unlike the original LHA-LSC scheme for calculating the FFCF,(62) calculating Eq. (4.8) does not require force derivatives as input. It should also be noted that Eq. (4.8) reduces to the classical FFCF in the classical limit and that nonclassical behavior of the symmetrized FFCF is accounted for in several ways:

1. Nonclassical sampling of bath coordinates and momenta.

2. The initial force, $\delta F(\mathbf{Q}')$, is not calculated at the initial position, $\mathbf{Q}_0$, used to generate the classical trajectory leading to the force at a later time t, $\delta F(\mathbf{Q}_t^{Cl}[\mathbf{Q_0}, \mathbf{P_0}])$.

3. The factor $e^{\beta \hbar \omega_{10}/2}$, which actually coincides with the so-called Schofield QCF.(88)

4.3 Model parameters and simulation techniques

The calculations of $C_s^{LHA-LSC}(t)$ reported below were based on Eq. (4.8) and carried out following the algorithm outlined below:

1. Perform an imaginary-time path integral molecular-dynamics (PIMD) simulation (157; 158) in order to sample the initial configuration, $\mathbf{Q_0}$, and the configuration at which the initial force is calculated, $\mathbf{Q'}$. To this end, it should be noted that within the context of a PIMD simulation, each DOF is represented by a cyclic polymer of P beads labeled $0, 1, 2, ..., P-1$. Assuming that P is even, $\mathbf{Q}_0$ is identified with the configuration of the beads labeled 0, while $\mathbf{Q'}$ is identified with the configuration of the beads labeled $P/2$.

2. Perform a LHA around $\mathbf{Q'}$, find the normal mode frequencies, $\{\Omega^{(k)}\}$, and corresponding transformation matrix, $\{T_{l,k}\}$, and use it to calculate $\{\alpha^{(k)}\}$ and sample the initial (normal-mode) momenta, $\{P_n^{(k)}\}$.

3. Calculate $\mathbf{Q}_t^{Cl}$ via a classical MD simulation for each sampled initial configuration $\mathbf{Q_0}$ and normal mode momenta $\mathbf{P_{n,0}}$, and time correlate $\delta F(\mathbf{Q}_t^{Cl})$ with $\delta F(\mathbf{Q'})$.

4. Repeat steps 1-3 and average over the results until reaching the desired convergence.

Simulations were performed on a liquid consisting of rigid HCl molecules. Energy relaxation via resonant vibrational energy transfer between HCl molecules, as opposed to nonresonant energy relaxation via transfer of vibrational energy into non-vibrational DOF (i.e. translations and rotations), is not considered because it does not affect the ensemble-averaged vibrational energy. More specifically, if one HCl molecule transfers in excess vibrational energy to another HCl molecule the overall ensemble-averaged vibrational energy does not change, whereas transferring it to non-vibrational DOF clearly decrease the ensemble-averaged vibrational energy. Intermolecular interactions were modeled in terms of Lennard-Jones (LJ) and electrostatic site-site pair interactions. Lennard-Jones parameters were adopted from the general AMBER force field (GAFF)(241), and partial charges were assigned

using a HF/6-31G* restrained electrostatic potential (RESP) and were given by $\delta_H = -\delta_{Cl} = 0.171593$e.The quantum mechanical calculations were done using Gaussian 03. Calculations were preformed using the AMBER molecular dynamics software package on a liquid at 188 K, with a density of 19.671 nm^{-3}, for which the experimental VER rate constant is available.(48) All calculations were preformed with 500 molecules contained in a cubic cell with periodic boundary conditions. PIMD simulations were preformed with 32 beads per atom. Each FFCF was averaged over 180,000 trajectories, each of length 4 ps.

In the absence of resonance with other vibrations, $\tilde{C}_s(\omega)$ was observed to decay asymptotically with frequency in an exponential manner. As a result, it becomes increasingly more difficult to average out the statistical noise accompanying any real-life simulation which is needed in order to calculate the increasingly small value of $\tilde{C}_s(\omega)$ at high frequencies. The results reported below were obtained by following the common practice of obtaining $\tilde{C}_s(\omega)$ at high frequencies by extrapolating the exponential gap law, that emerged at significantly lower frequencies.(172; 173; 101) It should be noted that strictly speaking, the exponential gap law has only been rigorously derived in the case of exponential repulsion interaction.(173) However, it was observed to be valid for the system under discussion in our research.

4.4 Results and discussion

In Fig. 4.1 we compare $e^{\beta\hbar\omega/2}\tilde{C}_s^{LHA-LSC}(\omega)$ and $\tilde{C}_s^{LHA-LSC}(\omega)$, as obtained via Eq. (4.8), with the corresponding classical $\tilde{C}^{Cl}(\omega)$ and $e^{\beta\hbar\omega/2}\tilde{C}^{Cl}(\omega)$. The corresponding predictions for the VER rate constants are shown in Table 4.1. The VER rate constant obtained from LHA-LSC via Eq. (4.8) is in excellent agreement with the experimental result. At the same time, the corresponding classical VER rate is two orders of magnitude slower than the experimental result, which is consistent with the expectation of strong quantum effects in a system that involves a transition frequency

which is about 20 times larger than $k_BT/\hbar$.

	$k_{0\leftarrow1}(\mathrm{HCl})/\mathrm{ns}^{-1}$	$k_{0\leftarrow1}(\mathrm{DCl})/\mathrm{ns}^{-1}$	$k_{0\leftarrow1}(\mathrm{HCl})/k_{0\leftarrow1}(\mathrm{DCl})$
Experiment	1.3	-	-
LHA-LSC	1.3 ± 0.9	0.7 ± 0.3	2 ± 1
Classical	0.055 ± 0.009	0.06 ± 0.01	0.9 ± 0.2
Schofield QCF	$(14 \pm 4) \times 10$	8 ± 1	17 ± 6

Table 4.1: k_{10}/ns^{-1} for neat liquid HCl and DCl at 188K. The experimental result for HCl was adopted from Ref. (48).

It should also be noted that $\tilde{C}_s^{LHA-LSC}(\omega) < \tilde{C}^{Cl}(\omega)$ throughout the entire range of frequencies. Thus, the combined effect of nonclassical initial sampling and the fact that the initial force is calculated at $\mathbf{Q}'$, rather than at $\mathbf{Q}_0$, is to *diminish* the value of $\tilde{C}_s^{LHA-LSC}(\omega)$ relative to its classical counterpart. However, it should be remembered that a more meaningful comparison is between $\tilde{C}^{Cl}(\omega)$ and $e^{\beta\hbar\omega/2}\tilde{C}_s^{LHA-LSC}(\omega)$. Indeed, $e^{\beta\hbar\omega/2}\tilde{C}_s^{LHA-LSC}(\omega)$ is significantly larger than $\tilde{C}^{Cl}(\omega)$, and more so with increasing frequency. Finally, it should also be noted that applying the Schofield QCF to the classical result, i.e. $e^{\beta\hbar\omega/2}\tilde{C}^{Cl}(\omega)$, leads to an overestimation of the VER rate constant by a factor of ~ 50 (see Fig. 4.1).

In order to gain insight into the role played by electrostatic forces in determining the VER rate in this system, we decomposed the force into its LJ and electrostatic contributions and considered the LJ-LJ, electrostatic-electrostatic, and LJ-electrostatic cross terms contributions to the FFCF. In Fig. 4.2, we compare these individual contributions in the classical case. The results clearly show that $\tilde{C}^{Cl}(\omega)$ is completely dominated by the nonpolar LJ-LJ contribution, which is consistent with the view that the electrostatic forces only play an indirect role through electrostriction, by allowing the liquid to access otherwise forbidden regions higher on the LJ repulsive walls.

In Fig. 4.3, we compare the LJ-LJ, electrostatic-electrostatic, and LJ-electrostatic cross terms contributions to $e^{\beta\hbar\omega/2}\tilde{C}_s^{LSC-LHA}(\omega)$. Similarly to the classical case, we find that the LJ and electrostatic forces are uncorrelated and that as a result the

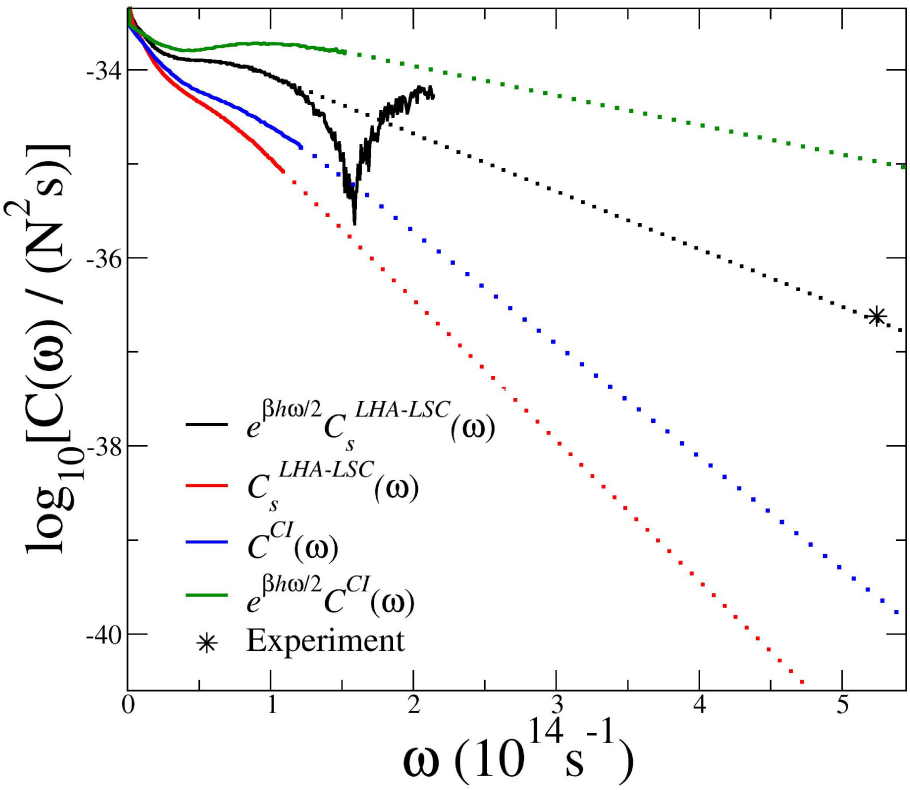

Figure 4.1: A semilog plot of $e^{\beta\hbar\omega/2}\tilde{C}_s^{LHA-LSC}(\omega)$, $\tilde{C}_s^{LHA-LSC}(\omega)$, $\tilde{C}^{Cl}(\omega)$ and $e^{\beta\hbar\omega/2}\tilde{C}^{Cl}(\omega)$ (Schofield QCF) for neat liquid HCl (T=188K, ρ =19.671 nm^{-3}). Solid lines were obtained from calculations and dashed lines correspond to extrapolations. The star corresponds to the experimental value at the transition frequency.

cross terms do not contribute significantly to the VER rate. However, in contrast to the classical case, the electrostatic-electrostatic term is seen to make a significant contribution to the VER rate so that the LHA-LSC VER rate constant is no longer dominated by the LJ-LJ term. In fact, by extrapolation, it appears that the relative contribution of the electrostatic-electrostatic term becomes increasingly more dominant with increasing frequency.

This result is surprising in light of the fact that the *classical* treatment points to electrostriction as the mechanism underlying VER in this system. Instead, we find that at least within the LHA-LSC treatment, the FT of the electrostatic-electrostatic FFCF decays more slowly with frequency, thereby making its contribution to the

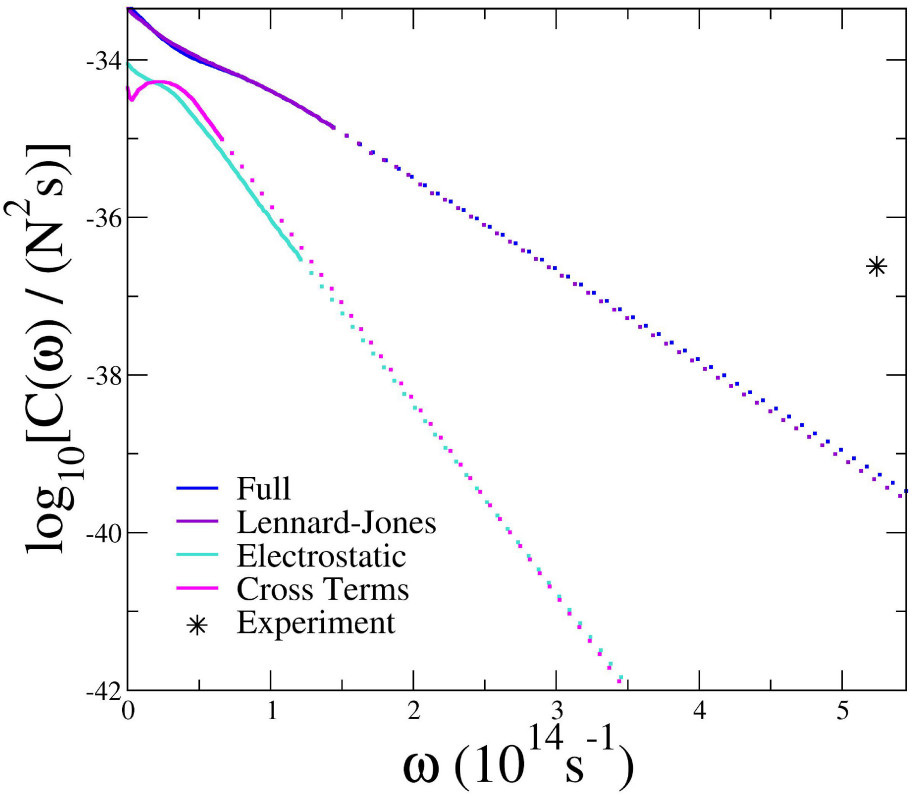

Figure 4.2: A semilog plot of the electrostatic-electrostatic, LJ-LJ and electrostatic-LJ cross term contributions to $\tilde{C}^{Cl}(\omega)$ for neat HCl (T=188K, ρ =19.671 nm^{-3}).

VER rate constant more important with increasing frequency. The origin for this qualitatively different behavior may be traced back to the fact that quantum delocalization allows the system to access nonclassical regions of configuration space where the electrostatic repulsive forces between the hydrogens are larger than in the classical case. Thus, instead of electrostriction where the attractive Coulombic forces bring the solute and solvent closer together, thereby amplifying the effect of non-Coulombic short-range repulsive forces, quantum delocalization brings the hydrogens closer than they would have been classically, thereby amplifying the contribution of repulsive Coulombic forces to the VER rate.

Further support for this interpretation comes from a similar calculation of the VER rate constant in the case of DCl (see Table 4.1 and Figs. 4.4 - 4.6). The substitution of the hydrogen by the heavier deuterium is seen to manifest itself by a

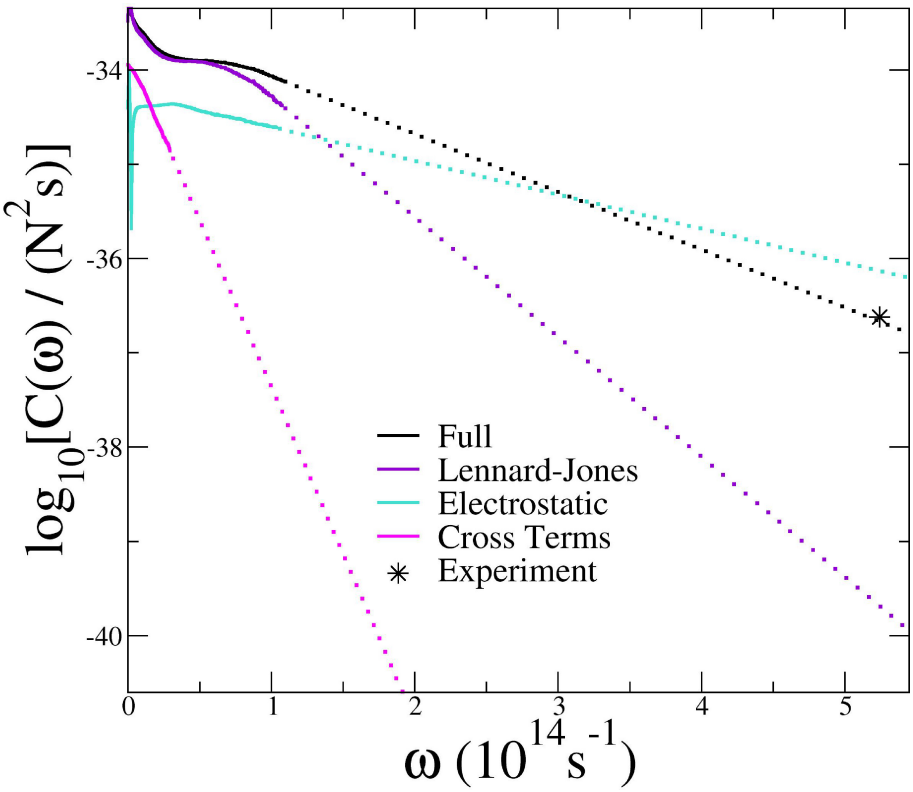

Figure 4.3: A semilog plot of the electrostatic-electrostatic, LJ-LJ and electrostatic-LJ cross term contributions to $e^{\beta\hbar\omega/2}\tilde{C}_s^{LSC-LHA}(\omega)$ for neat HCl (T=188K, ρ =19.671 nm^{-3}).

dramatically smaller quantum enhancement (by less than a factor of four as opposed to two orders of magnitude). This results in trend reversal in the dependence of the VER rate constant on isotope substitution. More specifically, whereas the *classical* VER rate constant of DCl is *faster* than that of HCl by a factor of ~ 3, the LHA-LSC-based VER rate constant of DCl is *slower* than that of HCl by a factor of ~ 5. Furthermore, the VER rate constant of DCl is seen to be completely dominated by the LJ forces within either classical and LHA-LSC treatments. This should be contrasted with the VER rate constant of HCl which is dominated by the LJ forces only within the classical treatment, This suggests that VER in HCl and DCl occurs via a different mechanism, namely electrostriction in DCl and quantum delocalization in HCl.

It is interesting to note that a similar argument was recently invoked to explain the isotope effect in the case of H_2/D_2 in liquid Ar.(56) In this case, the experimental

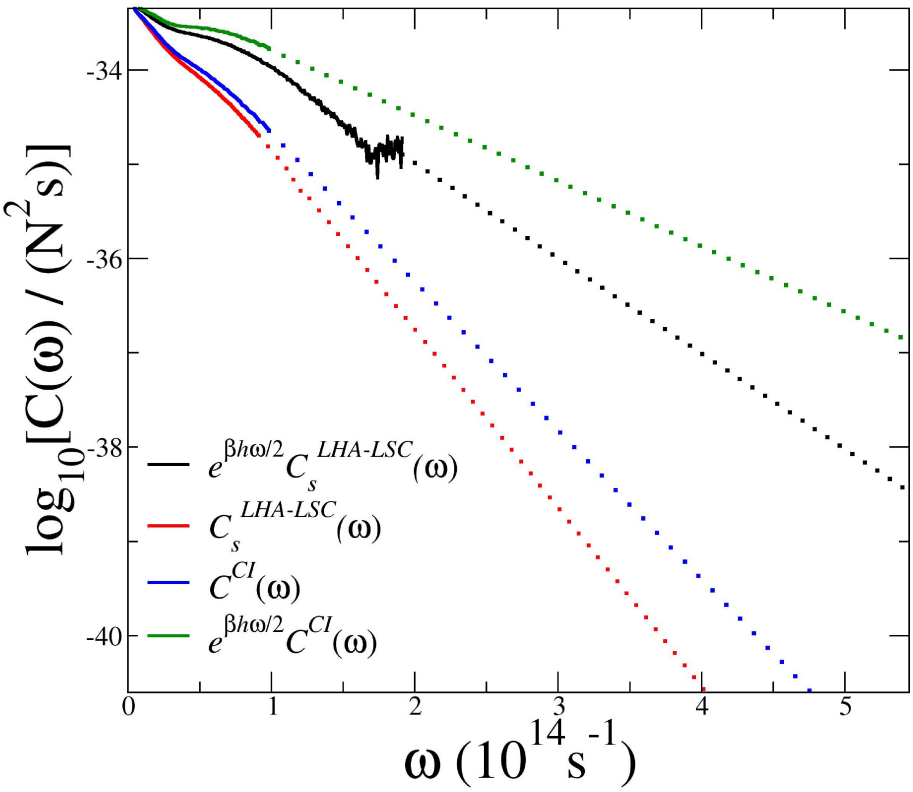

Figure 4.4: A semilog plot of $e^{\beta\hbar\omega/2}\tilde{C}_s^{LHA-LSC}(\omega)$, $\tilde{C}_s^{LHA-LSC}(\omega)$, $\tilde{C}^{Cl}(\omega)$ and $e^{\beta\hbar\omega/2}\tilde{C}^{Cl}(\omega)$ (Schofield QCF) for neat liquid DCl (T=188K, ρ =19.671 nm^{-3}). Solid lines were obtained from calculations and dashed lines correspond to extrapolations.

VER rate constant of H_2 is about an order of magnitude larger than that of D_2 despite the fact that $\omega_{10}(H_2)$ is larger than ω_{10} (D_2) by a factor of $\sqrt{2}$. Here too, a classical treatment was unable to account for this trend. However, the LHA-LSC method was able to capture the isotope effect quantitatively, thereby suggesting that its origin is purely quantum-mechanical. More specifically, the smaller mass of H_2 allowed it to penetrate more deeply into classically-forbidden regions, thereby sampling stronger repulsive forces which lead to the enhancement of the VER rate of H_2 relative to that of D_2. The key difference between H_2/D_2 in liquid Ar and liquid HCl/DCl being that the former is a nonpolar system while the latter is polar. Thus, in the case of HCl/DCl, the fact that the Coulombic repulsive wall is actually not as steep as the LJ repulsive wall allows the hydrogen to sample deeper into the region of classically-

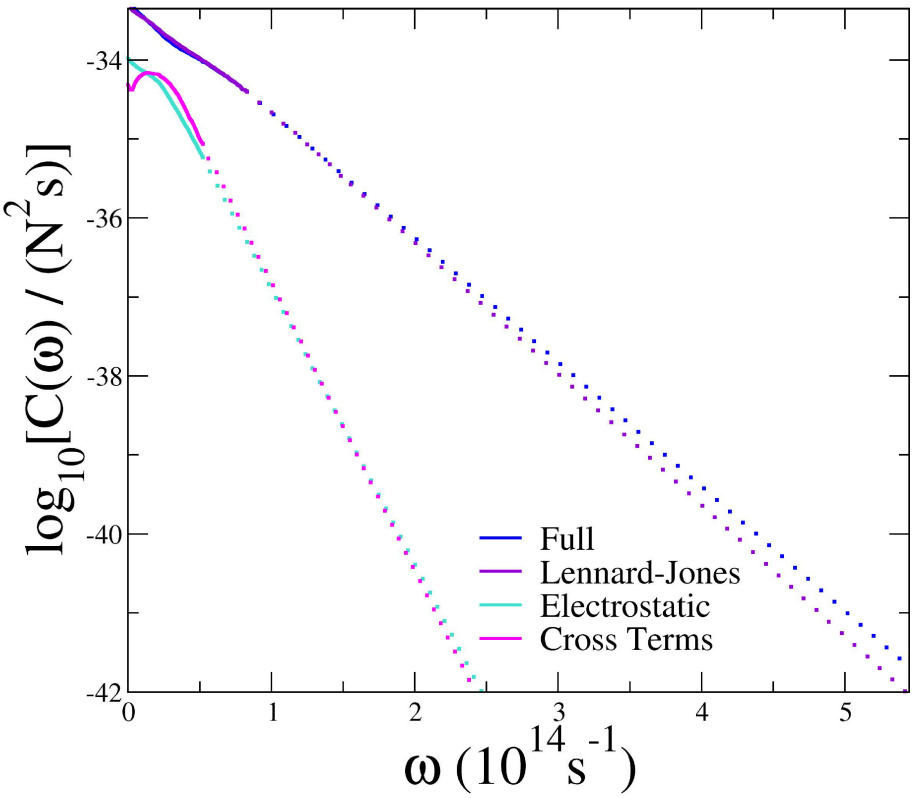

Figure 4.5: A semilog plot of the electrostatic-electrostatic, LJ-LJ and electrostatic-LJ cross term contributions to $\tilde{C}^{Cl}(\omega)$ for neat DCl (T=188K, ρ =19.671 nm^{-3}).

forbidden electrostatic forces, thereby enhancing their contribution relative to that of the LJ forces.

4.5 Summary

In our research, we have reported the first ever application of the LHA-LSC method to calculating the VER rate constant in a polar liquid. Carrying out this calculation was made easier by the introduction of the force-derivative-free LHA-LSC.(63) The choice of liquid HCl was motivated by the expectation of large quantum effects and the availability of experimental VER rates to compare with. The results indeed confirmed that a classical treatment can be misleading in systems of this type, both quantitatively and qualitatively. From the quantitative point of view,

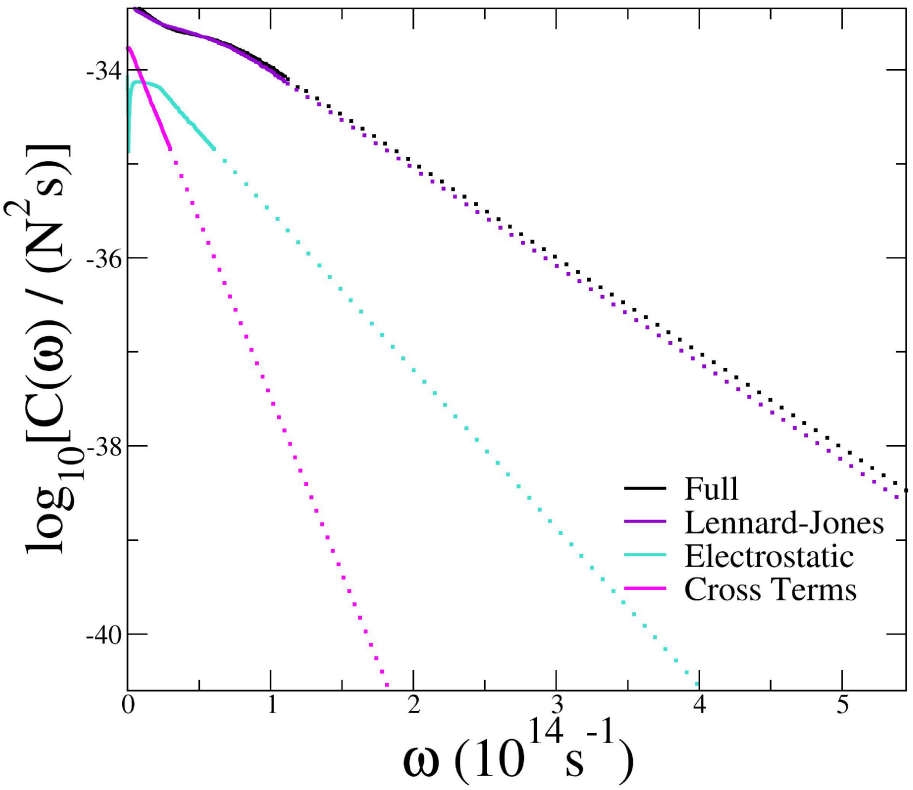

Figure 4.6: A semilog plot of the electrostatic-electrostatic, LJ-LJ and electrostatic-LJ cross term contributions to $e^{\beta\hbar\omega/2}\tilde{C}_s^{LSC-LHA}(\omega)$ for neat DCl (T=188K, ρ =19.671 nm^{-3}).

we find that the classical VER rate constant of HCl is two orders of magnitude slower than the experimental result. At the same time, the VER rate constant predicted via LHA-LSC was found to be in excellent agreement with experiment. From the qualitative point of view, we found that while nonpolar forces dominate the classical FFCF, electrostatic forces make a sizable contribution to the FFCF in the case of LHA-LSC. We also found a trend reversal with respect to the effect of isotope substitution on the VER rate constant and underlying mechanism. These results suggest that a classical treatment of VER may not be reliable in predicting VER rates as well as the mechanism underlying them in the case of hydrogen stretches in polar solutions. Further studies on other systems such as CN^-/H_2O(46; 52) and HOD/D_2O,(151; 174; 175; 176; 177; 178; 179; 180; 181) where similar effects can be expected and high quality experimental data are available will be necessary in order

to establish how general these trends are.

CHAPTER V

The Entropic Origin of Solvent Effects on The Single Bond *cZt-tZt* Isomerization Rate Constant of 1,3,5-*cis*-Hexatriene in Alkane and Alcohol Solvents: A Molecular Dynamics Study

5.1 Introduction

The ultrafast photoinduced ring opening reaction of 1,3-cyclohexadiene (CHD) has received much experimental and theoretical attention over the last several decades(182; 183; 184; 185; 186; 187; 188; 189; 190; 191; 192; 193; 194; 195; 196; 197; 198; 199; 200; 201; 202; 203; 204; 205). One reason for this attention is the similarity to the photoreaction of 7-dehydrocholesterol resulting in vitamin D formation(206; 207; 208; 209; 193). Another is the fact that the photoinduced ring opening reaction of 1,3-cyclohexadiene (CHD) provides an excellent model system for understanding solvent effects on isomerization rates, as well as the rates of related non-reactive relaxation processes such as cooling of a vibrationally hot state following electronic relaxation from a photoexcited electronic state to the ground electronic state.

Experimental studies have shown that CHD undergoes an electrocyclic ring opening reaction upon UV excitation to produce vibrationally hot *cis*-1,3,5-hexatriene

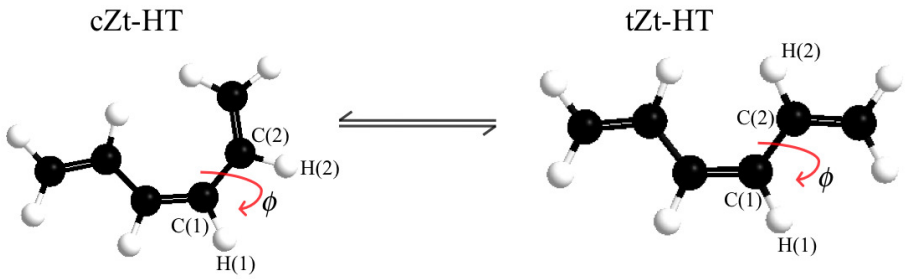

Figure 5.1: A schematic view of the cZt-HT (left) → tZt-HT (right) isomerization reaction. The atoms associated with the dihedral angle, ϕ, that serve as the reaction coordinate are labeled.

(Z-HT) with 40% quantum yield(210; 193; 187; 194; 192; 191). This is followed by vibrational cooling of Z-HT, on a picosecond timescale, resulting in a mixture of three rotational isomers, or rotatomers, that differ with respect to the degree of rotation around the single bond, namely , cZc-HT, cZt-HT and tZt-HT.

A small nonequilibrium subpopulation of the cZt-HT rotatomer is trapped at the end of this vibrational cooling step. (194; 193; 191; 190; 187; 192) Since the trapped subpopulation of cZt-HT is larger than its chemical equilibrium value, the subsequent equilibration involves the net reaction cZt-HT→tZt-HT, which occurs on a nanosecond timescale.(187) Monitoring the subpopulations of cZt-HT and tZt-HT in real time via time-resolved optical spectroscopy can then be used to measure the cZt-HT→tZt-HT reaction rate constant as well as its temperature and solvent dependence. Such measurements have been reported by Sension and coworkers in the temperature range of ∼(280-320)K and on a series of alkane (cyclohexane, *n*-hexadecane) and alcohol (ethanol, methanol and *n*-propanol) solvents(191; 190; 193; 194; 187; 192).

The main observations that emerged from these measurements can be summarized as follows:

- The measured rate constants are relatively insensitive to the specific alcohol or alkane, and in particular to variations in shear viscosity among alcohols and

alkanes.

- The measured rate constants are in general faster in alkane solvents than in alcohol solvents.

- The temperature dependence of the rate constants suggests that both activation energy and preexponential factor are solvent-dependent, with the preexponential factor in alkanes larger by an order of magnitude than that in alcohols, while the activation energy is larger in alkanes than that in alcohols.

It is important to note that the above mentioned differences between alcohol and alkane solvents *cannot* be explained based on Kramers theory,(211; 212) according to which the prefactor, and hence rate constant, should decrease with increasing viscosity.

Molecular dynamics (MD) simulations provide a useful way of shedding light on such questions.(213; 214; 215; 216; 217; 218; 219; 220; 221; 222; 223; 224; 225; 226)

For example, the photoisomerization reaction of *trans*-stilbene and the photochemical reactions leading to vitamin D synthesis are multistep reactions that are in many respects related to the photoinduced ring opening reaction of CHD. In both of these systems, MD simulations have been used for modeling and understanding the molecular level details behind the experimentally observed results(224; 225; 226; 227).

Reactive flux theory (RFT)(228; 229; 230; 231; 232; 233) provides a route for calculating the *exact* isomerization rate constant from such MD simulations (provided of course that the dynamics can be described by classical mechanics and that the force fields are accurate). More specifically, the only assumption underlying RFT is that the rate of barrier crossing is slower than the rates of all other dynamical processes that take place in the reactant and product wells, so that the reaction dynamics can be described by a rate constant. RFT also allows the calculation of the rate constant by using trajectories that start at the barrier top, thereby bypassing convergence

problems associated with rare event statistics.(234) The popular transition-state theory (TST)(235) can be obtained from RFT in the limit where barrier *recrossing* events are negligible. Finally, it should be noted that Kramers' theory,(211; 212) which is often invoked to describe solvent effects on reaction rate constants, is based on describing the underlying dynamics in terms of a Langevin equation. The latter avoids a molecularly detailed description of the solvent and accounts for solvent effects in terms of the dependence of the rate of recrossing on the solvent viscosity.

Our objective in this research is to shed light on the *molecular* origin of the above mentioned solvent effects by calculating the cZt-HT→tZt-HT isomerization rate constants via RFT, at different temperatures and for different explicit solvents. We do so for a series of different solvents (cyclohexane, cycloheptane, *n*-heptane, methanol, ethanol, *n*-propanol) on the temperature range (275-325)K.

The structure of the remainder of the chapter is as follows. Theoretical background and computational methods are outlined in Secs. 5.2 and 5.3, respectively. The results are presented and discussed in Sec. 5.4, followed by concluding remarks and outlook in Sec. 5.5.

5.2 Theory

5.2.1 Preliminaries

In this section, we formulate RFT for an isomerization reaction, as well as its TST limit, with emphasis on the underlying assumptions and the conditions for their validity. To this end, we restrict ourselves to the case of a unimolecular reaction, which is appropriate for the isomerization reaction under study here.

We start out by considering a *classical* system with the following generic Hamil-

tonian:

$$H\left(s,\dot{s},\mathbf{Q},\dot{\mathbf{Q}}\right)=T\left(\dot{s},\dot{\mathbf{Q}}\right)+V\left(s,\mathbf{Q}\right)\ . \tag{5.1}$$

Here, s and $\dot{s}$ are the reaction coordinate and corresponding velocity, respectively; $\mathbf{Q}=(Q_1,Q_2,\ldots)$ and $\dot{\mathbf{Q}}=\left(\dot{Q}_1,\dot{Q}_2,\ldots\right)$ are the non-reactive coordinates and corresponding velocities, respectively; $T\left(\dot{s},\dot{\mathbf{Q}}\right)$ is the overall kinetic energy and $V\left(s,\mathbf{Q}\right)$ is the overall potential energy.

Next, let $s=s^{\ddagger}$ define the transition state (TS), such that $s<s^{\ddagger}$ and $s>s^{\ddagger}$ correspond to *reactant* and *product*, respectively. We also define the heaviside function,

$$h(s)=\begin{cases}1 & s>s^{\ddagger}(\text{product})\\ 0 & s\leq s^{\ddagger}(\text{reactant})\end{cases}\ , \tag{5.2}$$

so that the product mole fraction at time t is given by:

$$x_P(t)=\int ds\int d\dot{s}\int\mathbf{dQ}\int\mathbf{d}\dot{\mathbf{Q}}\rho\left(s,\dot{s},\mathbf{Q},\dot{\mathbf{Q}};t\right)h(s)\equiv\langle h(s)\rangle_t\ . \tag{5.3}$$

Here, $\rho\left(s,\dot{s},\mathbf{Q},\dot{\mathbf{Q}};t\right)$ is the (nonequilibrium) phase-space density at time t. It should be noted that the reactant mole fraction at time t is given by:

$$x_R(t)=1-x_P(t)=\int ds\int d\dot{s}\int\mathbf{dQ}\int\mathbf{d}\rho\left(s,p,\mathbf{Q},\dot{\mathbf{P}};t\right)\left[1-h(s)\right]\equiv 1-\langle h(s)\rangle_t\ . \tag{5.4}$$

In the absence of external perturbation,

$$\rho\left(s,\dot{s},\mathbf{Q},\dot{\mathbf{Q}};t\right)\overset{t\to\infty}{\longrightarrow}\rho_{eq}\left(s,\dot{s},\mathbf{Q},\dot{\mathbf{Q}}\right)\equiv\frac{\exp\left[-H\left(s,\dot{s},\mathbf{Q},\dot{\mathbf{Q}}\right)/k_BT\right]}{\int ds\int d\dot{s}\int\mathbf{dQ}\int\mathbf{d}\dot{\mathbf{Q}}\exp\left[-H\left(s,\dot{s},\mathbf{Q},\dot{\mathbf{Q}}\right)/k_BT\right]}\ , \tag{5.5}$$

such that

$$x_P(t) \overset{t\to\infty}{\longrightarrow} x_{P,eq} \equiv \int ds \int d\dot{s} \int \mathbf{dQ} \int \mathbf{d\dot{Q}} \rho_{eq}\left(s, \dot{s}, \mathbf{Q}, \mathbf{\dot{Q}}\right) h(s) \equiv \langle h(s)\rangle_{eq}$$
$$x_R(t) \overset{t\to\infty}{\longrightarrow} x_{R,eq} \equiv \int ds \int d\dot{s} \int \mathbf{dQ} \int \mathbf{d\dot{Q}} \rho_{eq}\left(s, \dot{s}, \mathbf{Q}, \mathbf{\dot{Q}}\right) [1 - h(s)] \equiv 1 - \langle h(s)\rangle_{eq} \quad (5.6)$$

The concept of the *reaction rate constant* is based on assuming that the reaction dynamics can be described by a simple kinetic rate equation of the following form:

$$\dot{x}_P(t) = -\dot{x}_R(t) = -k_{RP}x_P(t) + k_{PR}x_R(t) \ , \quad (5.7)$$

where k_{PR} and k_{RP} are reactant-to-product and product-to-reactant reaction rate constants, respectively. Equivalently,

$$\delta\dot{x}_i(t) = -k\delta x_i(t) \ . \quad (5.8)$$

Here $i = P$ or R, $k = k_{PR} + k_{RP}$, $\delta x_i(t) = x_i(t) - x_i^{eq}$, $x_P^{eq} = k_{PR}/k$ and $x_R^{eq} = k_{RP}/k$.

It should be noted that relaxation processes are generally characterized by many relaxation times, not one. In order for reaction kinetics to be described by a single rate constant as in Eq. (5.8), the activation energy has to be much higher than k_BT, which results in the reaction rate constant being much slower on the time scale of all remaining nonreactive processes.(236; 237; 233) Under these circumstances, the reaction dynamics can be described by Eq. (5.8) (after a short transient time during which the reaction does not make significant progress).(233; 238)

Eq. (5.8) can be easily solved to give $\delta x_i(t) = \delta x_i(0)\exp(-kt)$. Thus, the actual reaction rate constant can be obtained from the following expression:

$$k = \lim_{t\to t_p} k(t) = -\lim_{t\to t_p} \delta\dot{x}_i(t)/\delta x_i(0) \quad (5.9)$$

Here, $k(t)$ is explicitly time-dependent during an initial transient period, $0 < t < t_p(\ll 1/k)$, following which it will reach the "plateau region", where it acquires a fixed value (provided that $t \ll 1/k$). (233; 238) This fixed value corresponds to the reaction rate constant, k.

5.2.2 The reaction rate constant from linear response theory

Since activated processes follow *rare-event statistics*, direct evaluation of the reaction rate constant from Eq. (5.9) would typically require prohibitively long *non-equilibrium* MD simulations. Linear response theory (LRT)(228; 239) provides an alternative route for calculating reaction rate constants that can bypass this obstacle. To this end, one needs to take advantage of the fact that since *the reaction rate constant is independent of the choice of initial condition, one is free to choose an initial state which is in the close vicinity of thermal equilibrium.*(228; 240) It is this assumption that makes it possible to calculate the reaction rate constant via LRT.

The derivation of an expression for the reaction rate constant from LRT starts out by considering a classical system with the total Hamiltonian $H\left(\mathbf{R},\dot{\mathbf{R}}\right)+fA\left(\mathbf{R}\right)$ at $t<0$ and $H\left(\mathbf{R},\dot{\mathbf{R}}\right)$ at $t\geq 0$ ($\mathbf{R}\equiv(s,\mathbf{Q})$ in the context of the current system). Here, f is a scalar coefficient, and $A\left(\mathbf{R}\right)$ is any perturbation that can shift the system from its unperturbed thermal equilibrium phase-space density

$$\rho_{eq}\left(\mathbf{R},\dot{\mathbf{R}}\right)=\frac{e^{-H\left[\mathbf{R},\dot{\mathbf{R}}\right]/k_BT}}{\int\mathbf{dR}\int\mathbf{d\dot{R}}e^{-H\left[\mathbf{R},\dot{\mathbf{R}}\right]/k_BT}}\ . \tag{5.10}$$

At $t=0$, the system is assumed to be in thermal equilibrium with respect to the perturbed Hamiltonian, so that its initial phase-space density is given by:

$$\rho(\mathbf{R},\dot{\mathbf{R}};t=0)=\frac{e^{-[H(\mathbf{R},\dot{\mathbf{R}})+fA(\mathbf{R})]/k_BT}}{\int\mathbf{dR}\int\mathbf{d\dot{R}}e^{-[H(\mathbf{R},\dot{\mathbf{R}})+fA(\mathbf{R})]/k_BT}}\ . \tag{5.11}$$

Thus, the ensemble-averaged value of a dynamical variable $B(\mathbf{R})$ at time $t\geq 0$ is

given by

$$\langle B\rangle_{eq}(t) = \frac{\int \mathbf{dR}_0 \int \mathbf{d\dot{R}}_0 e^{-[H(\mathbf{R}_0,\dot{\mathbf{R}}_0)+fA(\mathbf{R}_0)]/k_BT} B(\mathbf{R}_t)}{\int \mathbf{dR}_0 \int \mathbf{d\dot{R}}_0 e^{-[H(\mathbf{R}_0,\dot{\mathbf{R}}_0)+fA(\mathbf{R}_0)]/k_BT}} \ . \tag{5.12}$$

Here $\mathbf{R}_t$ is obtained by solving the classical equation of motion under the Hamiltonian $H(\mathbf{R},\dot{\mathbf{R}})$, with the initial conditions $\left\{\mathbf{R}_0,\dot{\mathbf{R}}_0\right\}$, to obtain $\left\{\mathbf{R}_t,\dot{\mathbf{R}}_t\right\}$ at time t.

Assuming that the initial phase-space density is close enough to the unperturbed equilibrium phase-space density, $\rho_{eq}\left(s,\dot{s},\mathbf{Q},\dot{\mathbf{Q}}\right)$, for the linear response limit, $f \ll 1$, to be valid, one may replace Eq. (5.12) by its expansion to first order in powers of f. This then results in the following expression for $\langle \delta B\rangle_{eq}(t)$ in terms of an equilibrium two-time correlation function:

$$\langle \delta B\rangle_{eq}(t) = \frac{f}{k_BT}\langle \delta A(\mathbf{R}_0)\delta B(\mathbf{R}_t)\rangle_{eq} \ , \tag{5.13}$$

where $\delta A(\mathbf{R}) = A(\mathbf{R}) - \langle A\rangle_{eq}$ and $\delta B(\mathbf{R}) = B(\mathbf{R}) - \langle B\rangle_{eq}$.

Now, assuming that $A = B = h(s)$, Eq. (5.13) reduces to:

$$\langle \delta h\rangle_{eq}(t) \equiv \delta x_P(t) = \frac{f}{k_BT}\langle \delta h(s_0)\delta h(s_t)\rangle_{eq} \ . \tag{5.14}$$

Substituting Eq. (5.14) into Eq. (5.9) then yields:

$$k = -\lim_{t\to t_p} \frac{\langle \delta h(s_0)\delta \dot{h}(s_t)\rangle_{eq}}{\langle [\delta h(s_0)]^2\rangle_{eq}} = \lim_{t\to t_p} \frac{\langle \delta \dot{h}(s_0)\delta h(s_t)\rangle_{eq}}{x_{R,eq}x_{P,eq}} \ . \tag{5.15}$$

Noting that $\delta\dot{h} = \dot{h} = \delta\left[s - s^{\ddagger}\right]\dot{s}$ is the *reactive flux*, we obtain the following expression for the reaction rate constant:

$$k = \lim_{t\to t_p} \frac{1}{x_{R,eq}x_{P,eq}} \langle \delta\left[s_0 - s^{\ddagger}\right]\dot{s}_0 h(s_t)\rangle_{eq} \ . \tag{5.16}$$

It should be noted that $k_{PR} = kx_{P,eq}$ and $k_{RP} = kx_{R,eq}$. Eq. (5.16) is the RFT expression for the reaction rate constant. Importantly, it represents an *exact* expression

for the rate constant, provided that classical mechanics is valid and the force fields are accurate.

5.2.3 Transition state theory

TST can be obtained from Eq. (5.16) by replacing $h\left[s_t\right]$ by $h\left[\dot{s}_0\right]$. This assumption is equivalent to neglecting barrier *recrossing*, that is assuming that starting at a TS configuration with a positive velocity along the reaction coordinate ($\dot{s} > 0$) guarantees barrier crossing, that is $h(s_t) = 1$. This then leads to the following expression for the reaction rate constant:

$$k_{TST} = \frac{1}{x_{R,eq} x_{P,eq}} \langle \delta\left(s - s^{\ddagger}\right) \dot{s} h(\dot{s}) \rangle_{eq} = \langle \dot{s} h(\dot{s}) \rangle_{eq} \langle \delta\left(s - s^{\ddagger}\right) \rangle_{eq} \ . \tag{5.17}$$

Importantly, the TST reaction rate constant is given in terms of an *equilibrium* ensemble average, as opposed to an equilibrium two-time correlation function within RFT. As a result the $\dot{s}$-dependent and s-dependent factors can be averaged separately.

The s-dependent factor in Eq. (5.17) can be put in the Arrhenius form:

$$\begin{aligned} &\frac{1}{x_{R,eq}} \langle \delta\left(s - s^{\ddagger}\right) \rangle_{eq} \\ &= \frac{\int \mathbf{dQ} \exp\left[-V(\mathbf{Q}, s^{\ddagger}/k_B T\right]}{\int \mathbf{dQ} \int_{s \leq s^{\ddagger}} ds \exp\left[-V(\mathbf{Q}, s)/k_B T\right]} \\ &= \exp\left[-\Delta G^{\ddagger}/k_B T\right] = \exp\left[\Delta S^{\ddagger}/k_B\right] \exp\left[-\Delta H^{\ddagger}/k_B T\right] \ . \end{aligned} \tag{5.18}$$

Here, $\Delta G^{\ddagger} = G^{\ddagger} - G^{R}$, $\Delta S^{\ddagger} = S^{\ddagger} - S^{R}$ and $\Delta H^{\ddagger} = H^{\ddagger} - H^{R}$ are the Gibbs free energy, entropy and enthalpy difference between the TS and the reactant state (assuming that the reaction takes place under constant temperature and pressure). Thus, the reactant-to-product rate reaction rate constant is given by:

$$k_{PR}^{TST} = A \exp\left[-\Delta H^{\ddagger}/k_B T\right] \ , \tag{5.19}$$

with

$$A = \langle \dot{s} h(\dot{s}) \rangle_{eq} \exp\left[\Delta S^{\ddagger}/k_B\right] \tag{5.20}$$

Finally, comparison to Eq. (5.16) reveals that

$$k_{PR} = \kappa k_{PR}^{TST} \ , \tag{5.21}$$

where κ is the so-called *transmission coefficient*, which is explicitly given by:

$$\kappa = \lim_{t \to t_p} \frac{\langle \dot{s}_0 \delta\left[s_0 - s^{\ddagger}\right] h(s_t) \rangle_{eq}}{\langle \dot{s} h(\dot{s}) \rangle_{eq}} \ . \tag{5.22}$$

It should be noted that $\kappa < 1$ due to recrossing and that as a result, k_{TST} corresponds to an upper bound on the actual rate constant, $k \leq k_{TST}$.

5.3 Computational Methods

MD simulations were performed on a system that consists of one HT molecule and 300-400 solvent molecules (depending on solvent), in a truncated octahedron box with standard periodic boundary conditions. The reaction coordinate is given by the dihedral angle, ϕ, along $H(1) - C(1) - C(2) - H(2)$ atoms of HT (see Fig. 5.1). The TS corresponds to $\phi^{\ddagger} = 90^o$, so that $\phi < \phi^{\ddagger}$ and $\phi > \phi^{\ddagger}$ correspond to reactant (cZt-HT) and product (tZt-HT), respectively.

Classical MD simulations were carried out via the AMBER10 software package, using the general AMBER force field (GAFF).(241) Lennard-Jones parameters were adopted from GAFF and atomic partial charges were obtained via the restrained electrostatic potential (RESP) method(242; 243; 244) after calculating the electrostatic potential via HF/6-31G* using the Gaussian 09 software package. All the simulations were carried out with a time step of 1.0fs. Gibbs free energy profiles as a function of ϕ were obtained from the corresponding potentials of mean force using umbrella

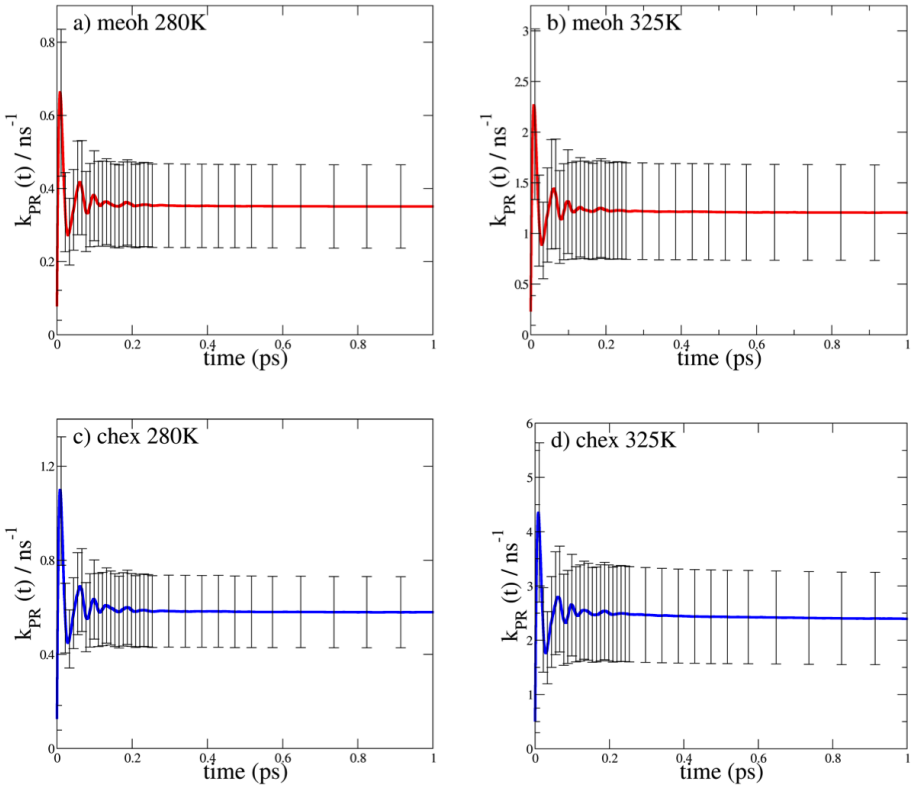

Figure 5.2: Demonstrative examples of calculations of the rate constant via RFT for methanol (meoh) at 280K (a) and 325K (b), and for cyclohexane (chex) at 280K (c) and 325K (d).

sampling with the weighted histogram analysis method (WHAM), via the WHAM software package.(245)

For the free energy calculations, the system was equilibrated for 450 ps at a constant pressure of 1.0atm and the desired temperature, following a simulated annealing for 100 ps, where the temperature was controlled using the Andersen temperature coupling scheme(246). The solute and the solvent intramolecular bond lengths were constrained to their equilibrium values using the SHAKE algorithm.(247). Umbrella sampling simulations were carried out with harmonic spring constant of 0.04 kcal/(mol deg^2) at different values of the $H(1)-C(1)-C(2)-H(2)$ dihedral angle, ϕ. To this end, we employed 181 bins, each of which 2^o wide, and ran a 250 ps long trajectory to sample the time series of the dihedral angles. WHAM was then used to generate the potential of mean force for each solvent at constant temperature and pressure conditions.

For the rate constant calculations using the TST method, the system was equilibrated for 40ps with the dihedral angle, ϕ, constrained to its TS value, $\phi^\ddagger = 90^o$, followed by a production run consisting of 1,000 200ps long trajectories during which the dihedral angle was constrained to its TS value. For the rate constant calculations using the RFT method, equilibration was performed similarly to the TST calculations. However, production runs were performed with an unconstrained dihedral angle. The RFT results reported here were obtained by averaging over 50,000 trajectories (each 1ps long). Error bars were calculated by dividing the trajectories into 10 blocks and calculating the standard-deviatio (100 200ps trajectories per block for TST and 5,000 1ps trajectories per block for RFT).

5.4 Results and Discussion

Examples of calculations of the rate constant via RFT, Eq. (5.16), for methanol (meoh) at 280K (a) and 325K (b), and for cyclohexane (chex) at 280K (c) and 325K

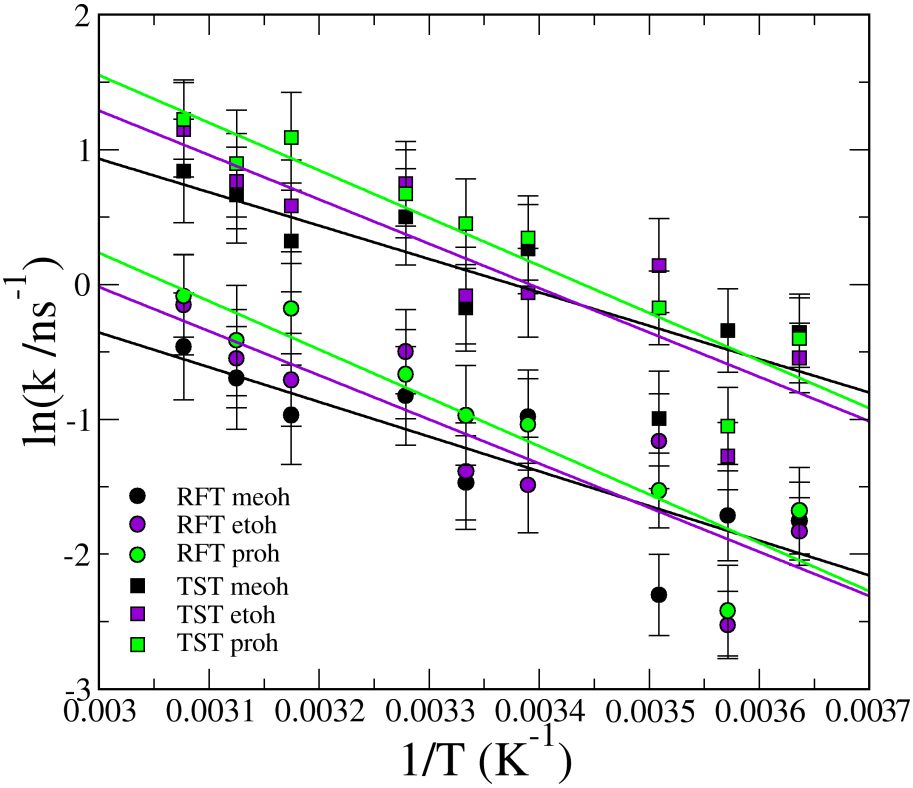

Figure 5.3: Arrhenius plot of the cZt-HT→tZt-HT isomerization rate constants obtained via RFT (circles) and TST (squares) in methanol (meoh), ethanol (etoh) and *n*-propanol (proh) solvents.

Table 5.1: cZt-HT to tZt-HT Isomerization Rate Constant Calculated using TST and RFT methods at 320 K

Solvent	Transition State Theory $k_{TST}(ns^{-1})$	Reactive Flux Theory $k_{RFT}(ns^{-1})$
Methanol	1.9 ± 0.7	0.5 ± 0.2
Ethanol	2.2 ± 0.8	0.6 ± 0.2
Propanol	2.4 ± 1.0	0.7 ± 0.3
Cyclohexane	3.2 ± 1.0	1.0 ± 0.3
Nheptane	3.4 ± 1.2	0.9 ± 0.3
Cycloheptane	4.9 ± 2.0	1.2 ± 0.5

(d), are shown in Fig. 5.2. As expected, the plateau region is reached within a few hundred femtoseconds, which is much shorter than $1/k_{PR}$ ($\sim$ ns), thereby justifying the assumptions underlying RFT. The RFT rate constants reported below for other solvents and/or at other temperatures were obtained from similar calculations (not shown). Arrhenius plots of the cZt-HT$\rightarrow$tZt-HT rate constants, as obtained via RFT and TST, in different alcohol solvents (methanol, ethanol and n-propanol) and alkane solvents (cyclohexane, cycloheptane and n-heptane), are shown in Figs. 5.3 and 5.4, respectively.

In addition, we also show the Arrhenius plots obtained by grouping all the alcohol solvents together and all the alkanes together, when the reaction rate constants are obtained via TST (Fig. 5.5) and RFT (Fig. 5.6). The following conclusions can be obtained based on Figs. 5.3 - 5.6:

- The rate constants obtained via both RFT and TST are consistent with the experimentally observed trend of faster isomerization rates in alkane solvents in comparison to alcohol solvents.(187)

- The rate constants calculated via TST are larger than the rate constants calculated via RFT by a factor of 3-4. This is consistent with the fact that TST rate constants correspond to an upper bound on RFT rate constants, since the former can be obtained from the latter by neglecting the effect of barrier recrossing

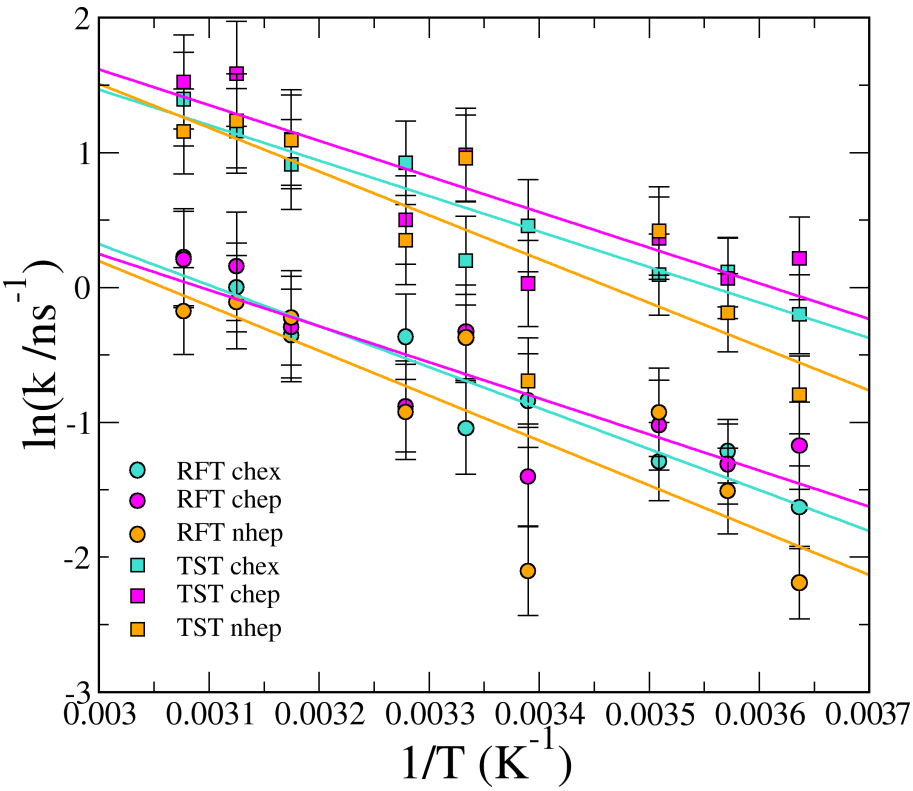

Figure 5.4: Arrhenius plot of the cZt-HT→tZt-HT isomerization rate constants obtained via RFT (circles) and TST (squares) in cyclohexane (chex), cycloheptane (chep) and *n*-heptane (nhep) solvents.

events.

- The rate constants calculated via RFT are somewhat slower than the experimental rate constants. We attribute this to the fact that the rate constant is exponentially sensitive to the activation free energy, which is in turn sensitive to inaccuracies in the force fields.

- The slopes of the calculated Arrhenius plots in alcohol and alkane solvents are comparable, implying that the activation enthalpy is insensitive to the solvent type. However, the intercepts are observed to be significantly higher in alkane solvents. Since the same behavior is observed when TST is used, one can conclude that the difference in intercept between alcohol and alkane solvents is *not* due to dynamical effects embodied by the transmission coefficient, and can

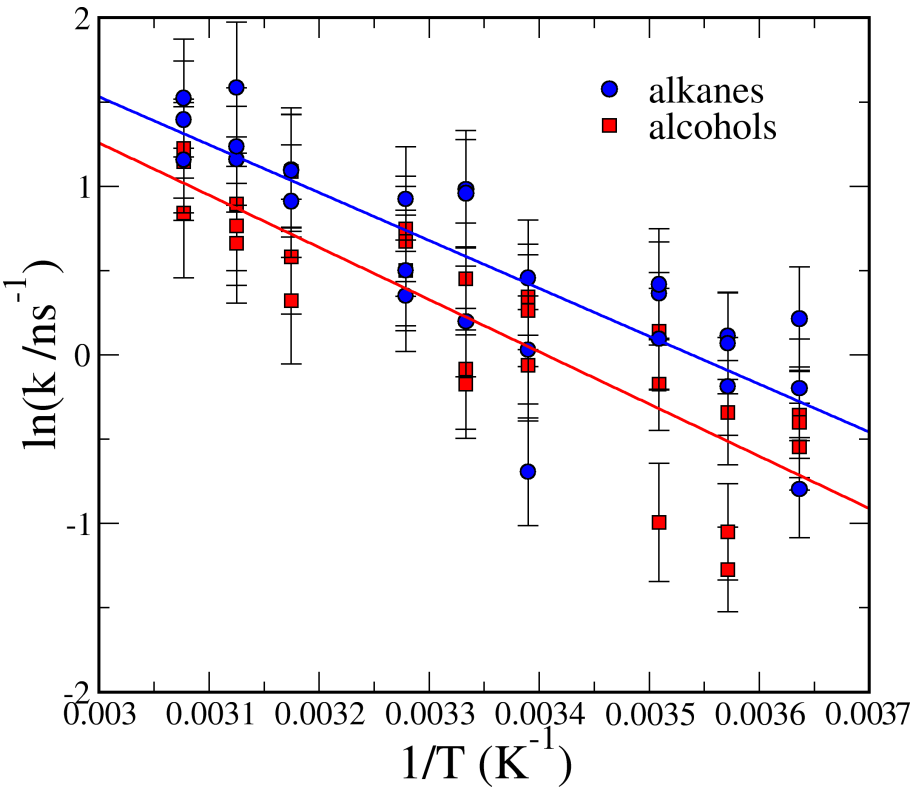

Figure 5.5: Arrhenius plot of the cZt-HT→tZt-HT isomerization rate constants obtained via TST in alcohols (methanol, ethanol and *n*-propanol grouped together) and alkanes (cyclohexane, cycloheptane, and *n*-heptane grouped together).

therefore be attributed to a larger entropy of the TS configurations relative to the reactant configurations in alkane solvents.

The entropic origin of the difference between the rate constants in alkanes and alcohols is further supported by Fig. 5.7, which shows the Gibbs energy profiles at 320K as a function of the dihedral angle, ϕ, for the different solvents. The activation Gibbs energy in alcohol solvents is observed to be systematically higher than that in alkane solvents. Since the activation enthalpy is similar for both solvent types, one can conclude that the origin of the difference is entropic.

On the molecular level, this difference can be traced back to the very different structures of the solvation shells in alcohol and alkane solvents. More specifically, Z-HT in alcohol solvents fits within a relatively rigid void formed by the hydrogen-

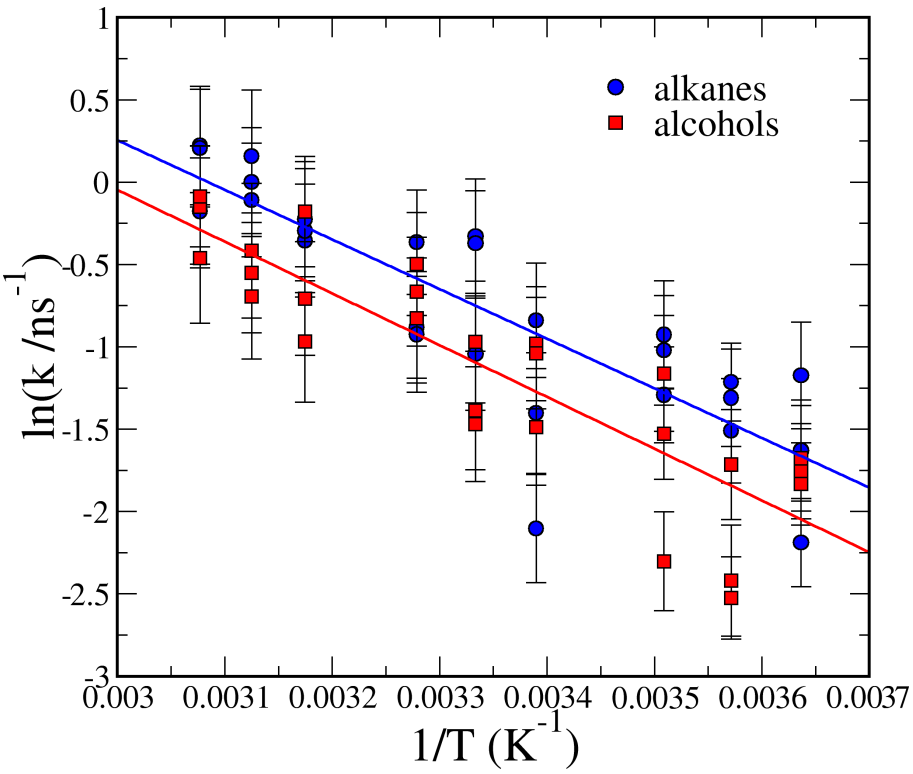

Figure 5.6: Arrhenius plot of the cZt-HT→tZt-HT isomerization rate constants obtained via RFT in alcohols (methanol, ethanol and *n*-propanol grouped together) and alkanes (cyclohexane, cycloheptane, and *n*-heptane grouped together).

bonded network, which is insensitive to conformational dynamics. At the same time, alkane solvents form a void whose shape can adjust to the instantaneous Z-HT conformation, thereby increasing the entropy of the TS and giving rise to faster isomerization. This difference in the structure of the first solvation shell is confirmed by the solute-solvent (center-of-mass to center-of-mass) radial distribution functions, which show a tighter packing in alkanes in comparison to alcohols when HT is in the TS configuration (see Fig. 5.8).

5.5 Concluding Remarks

cZt-HT→tZt-HT isomerization rate constants were calculated from classical MD simulations, with explicit solvents via TST and RFT in several alcohol and alkane sol-

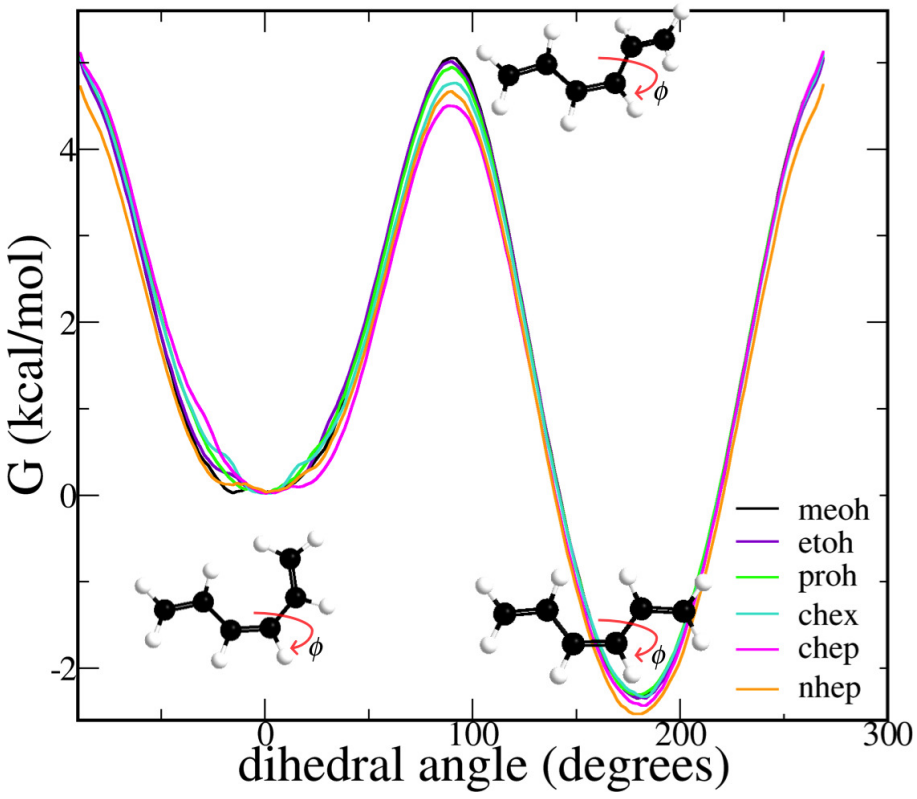

Figure 5.7: Free energy profiles as a function of dihedral angle for the cZt-HT→tZt-HT isomerization reaction, at 320K, in methanol (meoh), ethanol (etoh), *n*-propanol (proh), cyclohexane (chex), cycloheptane (chep), *n*-heptane (nhep) solvents.

vents and on a wide range of temperatures. The calculated rate constants were found to be consistent with the major experimentally observed trend of faster isomerization rate in alkane solvents in comparison to alcohol solvents. Analysis based on the shape of the Arrhenius plots, free energy profiles and solvent-solute radial distribution functions point to entropy as the origin of solvent effects in this system. The latter can be traced back to the fundamentally different structure of the first solvation shell in alcohol and alkane solvents. More specifically, while alkane solvents pack tightly around the solute and adjust to its conformational state as it moves through the TS, alcohol solvents form relatively open and rigid hydrogen-bonded cage structures which are relatively insensitive to HT conformational state.

It should be noted that while the above mentioned general trend between alkane

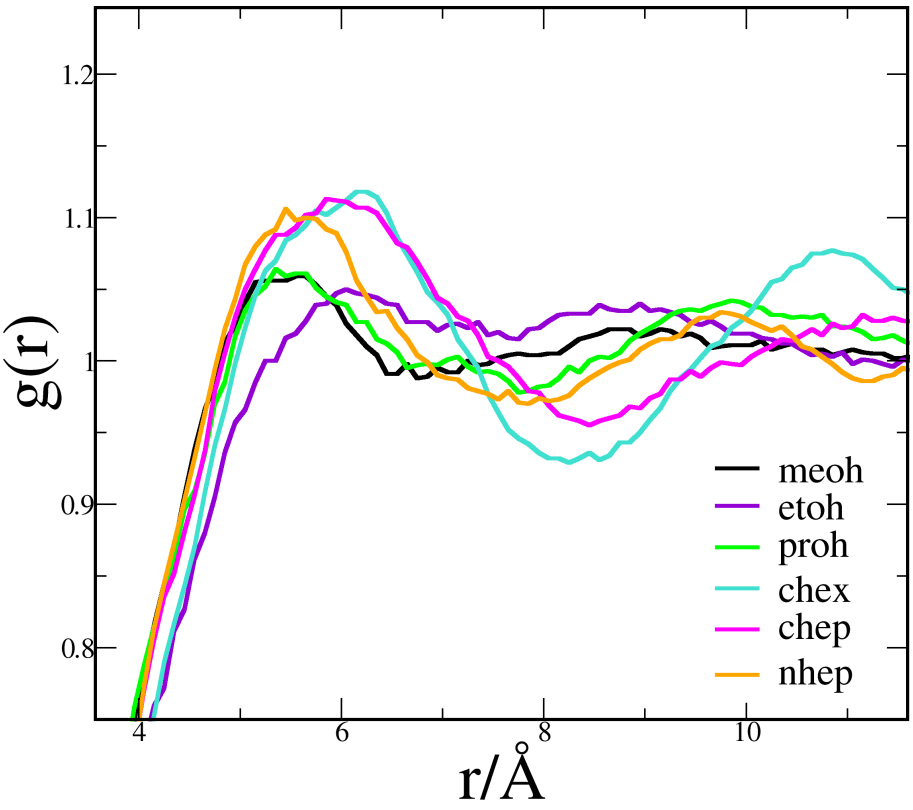

Figure 5.8: Radial distribution function between solvent and solute molecules in the TS geometry, at 320 K, for methanol (meoh), ethanol (etoh), *n*-propanol (poh), cyclohexane (chex), cycloheptane (chep), *n*-heptane (nhep) solvents.

and alcohol solvents was reproduced, several discrepancies between simulation and experiment remain. Most notably: (1) The simulated rate constants are somewhat slower than the experimental ones; (2) The experimentally observed larger activation enthalpy in alkanes relative to alcohol solvents is not reproduced by the simulations. Although the origin of these discrepancies are difficult to trace, they likely reflect inaccuracies in the force fields. To this end, it should be noted that the rate constants are exponentially sensitive to the activation Gibbs energy and that the force fields do not account for polarizability effects. Thus, employing polarizable force fields which are better parametrized for capturing the dynamics away from chemical equilibrium and in the vicinity of the TS may lead to a more quantitative agreement between simulated and experimental rate constants.

Similar studies on HT derivatives with bulkier side chains, such as pre-vitamin D, α-terpinene and α-phellandrene, offer an interesting extension of the present study.(248; 249) More specifically, one can expect trend reversal when the range of conformational motion exceeds the size of the hydrogen-bond cage in alcohol solvents, thereby leading to a higher enthalpic barrier.

CHAPTER VI

Conclusions and Future Directions

The major theme of this dissertation research has been the in-depth study of reactive and non-reactive energy relaxation processes in condensed phase using computational methods based on molecular dynamics (MD) simulations. Investigations of non-reactive energy relaxation processes comprised primarily of the prediction and analysis of vibrational energy relaxation (VER) in multiple condensed phase systems with the molecule of interest exhibiting high-energy vibrations, such that $\hbar\omega/k_BT \gg 1$. The systems studied includes neat liquid HCl and DCl and isotopomeric mixtures of CN^- in H_2O and D_2O. The primary reason behind choosing systems with high-energy vibrations (vibrational stretch frequencies for C-N and H-Cl are 2080 cm^{-1} and 2783 cm^{-1}, respectively) is that, in the study of the relaxation dynamics of these molecules, one needs to treat the relaxing vibrational mode as well as the relevant accepting modes in the framework of quantum dynamics. Recent theoretical and computational studies of VER have been mostly based on the Landau Teller (LT) formula,(40; 155) which gives the VER rate constant in terms of the Fourier transform (FT), at the vibrational transition frequency, of the *quantum-mechanical* autocorrelation function of the fluctuating force (FFCF) exerted on the relaxing mode by the other degrees of freedom (DOF), i.e. the bath. An exact calculation of the quantum-mechanical FFCF in a condensed phase system is beyond the scope of present day computational

resources due to exponential scaling of computational cost with the number of DOF. Therefore, we have explored the applications of semiclassical methods in the calculation of VER rate constants in high frequency vibrational modes in condensed phase, particularly, the linearized semiclassical (LSC) method(87; 62; 86; 76; 54; 56) that has been developed in the Geva group in the last decade. Interestingly, the study of VER in neat liquid HCl/DCl and the CN^- in aqueous solution are examples of the first ever implementations of the LSC method in the calculations of VER rate constant in case of a polar liquid system and an ionic system in polar solvent, respectively. Using a thorough approach for implementation of the LSC method, we were able to obtain VER rate constants for both the systems studied with excellent agreement with the experimentally measured rate constants.

The major conclusion that can be derived from all the VER studies combined is that, the quantum effects in the calculation of VER rate constant plays a significant role, and cannot be neglected. More specifically, it was observed that in the case of neat liquid HCl, while nonpolar forces dominate the classical FFCF, electrostatic forces make a sizable contribution to the FFCF when calculated within the framework of LSC, indicating a fundamental difference in the mechanism of VER as captured by the classical treatment and the quantum mechanical treatment of the involved VER dynamics. It was observed that while the classical treatment points to *electrostriction* as the mechanism of VER in this system, the quantum-mechanical treatment indicates towards *quantum delocalization* as the likely origin of the qualitatively different behavior of the FFCF calculated using the LSC method. On a quantitative note, the classical VER rate constant of HCl was found to be two orders of magnitude slower than the experimental result. At the same time, the VER rate constant predicted via LSC method was found to be in excellent agreement with experiment. This trend was also observed in case of the VER in cyanide ion in aqueous solution, where the classical VER rate constant was found to be an order of magnitude shorter than the

experimental rate constant, whereas, accounting for quantum effects in the calculation of VER via the LSC method and/or by using the harmonic/Schofield quantum correction factor (67) (QCF) led to VER rate constants with quantitative agreement with experimental rate constants. The major conclusion, however, was that our results suggested that taking into account quantum effects on the VER of cyanide in aqueous solution could make the intermolecular pathway (involving translations and rotations of the solvent) at least as likely as the intramolecular pathway (involving water bend vibrational modes).

There are many directions into which the VER investigations can be carried forward. In the applications of the LSC method in the calculation of VER rate constant presented in this thesis, the LSC method was, for the first time, implemented in the case of a polar liquid and an ionic species in a polar solvent. The next step from here, would be to apply the LSC method to more complex systems, for example, in molecules with multiple DOF, including multiple vibrational modes, capable to accepting the energy released by the high-frequency excited vibrational mode. One such example would be, Amide I mode of *N*-methylacetamide in D_2O solution(250), among many other examples of VER in proteins.

The second major theme of the thesis comprised of the study of reactive chemical process where we calculated the single-bond *cZt-tZt* isomerization rate constant of 1,3,5-*cis*-hexatriene dissolved in a series of explicit alkane (cyclohexane, *n*-heptane and cycloheptane) and alcohol (methanol, ethanol and *n*-propanol) solvents, using classical MD simulations via the reactive flux theory at different temperatures (275-325K). Our main objective, in this study, was to shed light on the *molecular* origin of the experimentally observed trend of isomerization rate constant,(187) wherein the isomerization rate constants in alcohol solvents were reportedly slower than those in alkane solvents. We found that the isomerization rate constants in alcohol solvents were indeed slower than those in alkane solvents, in accord with the observed exper-

imental trend. The same trend was obtained when the transition state theory limit of the reactive flux expression for the reaction rate constant was employed. It was conlcuded from the detailed study of the thermodynamics associated with the isomerization reaction, as well as, the analysis of the radial distribution function of the solvent-solute center of mass at the transition state of the solute, that, the solvent dependence of the reaction rate constant can be traced back to the fundamentally different structure of the solvation shell in alcohol and alkane solvents. It was found that whereas in alcohol solvents, hexatriene fits inside a rigid cavity formed by the hydrogen-bonded network, which is relatively insensitive to conformational dynamics, alkane solvents form a cavity around hexatriene that adjusts to the conformational state of hexatriene, thereby increasing the entropy of transition state congfiurations relative to reactant configurations and giving rise to faster isomerization. An interesting extension of the classical MD study would be a similar analysis on hexatriene derivatives with bulkier side chains, such as pre-vitamin D, α-terpinene and α-phellandrene(248; 249). More specifically, one can expect trend reversal when the range of conformational motion exceeds the size of the hydrogen-bond cage in alcohol solvents, thereby leading to a higher enthalpic barrier.

Bibliography

[1] Nitzan, A. *Chemical Dynamics in Condensed Phases*; Oxford University Press Inc.: New York, 2009.

[2] Biaz, C. R.; McRobbie, P. L.; Anna, J. M.; Geva, E. Two dimensional infrared spectroscopy of metal carbonyls. *Acc. Chem. Res.* **2009**, *42*, 1395-1404.

[3] DeFlores, L. P.; Nicodemus, R. A.; Tokmakoff, A. Two Dimensional Fourier Transform Spectroscopy in the Pump-Probe Geometry. *Opt. Lett.* **2007**, *32*, 2966-2968.

[4] Khalil, M.; Demirdoven, N.; Tokmakoff, A. Vibrational Coherence Transfer Characterized with Fourier-Transform 2D IR Spectroscopy. *J. Chem. Phys.* **2004**, *121*, 362-373.

[5] Khalil, M.; Demirdoven, N.; Tokmakoff, A. Obtaining Absorptive Line Shapes in Two- Dimensional Infrared Vibrational Correlation Spectra. *Phys. Rev. Lett.* **2003**, *90*, 047401.

[6] Khalil, M.; Demirdoven, N.; Tokmakoff, A. Correlated Vibrational Dynamics Revealed by Two-Dimensional Infrared Spectroscopy. *J. Phys. Chem. A* **2003**, *107*, 5258-5279.

[7] Demirdoven, N.; Khalil, M.; Tokmakoff, A. Coherent 2D IR Spectroscopy: Molecular Structure and Dynamics in Solution. *Phys. Rev. Lett.* **2002**, *89*, 237401.

[8] Golonzka, O.; Khalil, M.; Demirdoven, N.; Tokmakoff, A. Vibrational Anharmonicities Revealed by Coherent Two-Dimensional Infrared Spectroscopy. *Phys. Rev. Lett.* **2001**, *86*, 2154-2157.

[9] Lian, T.; Locke, B.; Kholodenko, Y.; Hochstrasser, R. M. Energy-flow from solute to solvent probed by femtosecond IR spectroscopy - malachite green and heme protein solutions. *J. Phys. Chem.* **1994**, *98*, 11648-11656.

[10] Lim, M. H.; Jackson, T. A.; Anfinrud, P. A. Femtosecond near-IR absorbance study of photoexcited myoglobin: Dynamics of electronic and thermal relaxation. *J. Phys. Chem.* **1996**, *100*, 12043-12051.

[11] Mizutani, Y.; Kitagawa, T. Direct observation of cooling of heme upon photodissociation of carbonmonoxy myoglobin. *Science* **1997**, *278*, 443-446.

[12] Sagnella, D. E.; Straub, J. E.; Jackson, T. A.; Lim, M.; Anfinrud, P. A. Vibrational population relaxation of carbon monoxide in the heme pocket of photolyzed carbonmonoxy myoglobin: Comparison of time-resolved mid-IR absorbance experiments and molecular dynamics simulations. *Proc. Natl. Acad. Sci. USA* **1999**, *96*, 14324-14329.

[13] Rosca, F.; Kumar, A. T. N.; Ye, X.; Sjodin, T.; Demidov, A. A.; Champion, P. M. Investigations of coherent vibrational oscillations in myoglobin. *J. Phys. Chem. A* **2000**, *104*, 4280-4290.

[14] Wang, W.; Ye, X.; Demidov, A. A.; Rosca, F.; Sjodin, T.; Cao, W.; Sheeran, M.; Champion, P. M. Femtosecond multicolor pump-probe spectroscopy of ferrous cytochrome C. *J. Phys. Chem. B* **2000**, *104*, 10789-10801.

[15] Xie, A.; van der Meer, L.; Hoff, W.; Austin, R. H. Long-lived amide I vibrational modes in myoglobin. *Phys. Rev. Lett.* **2000**, *84*, 5435-5438.

[16] Fayer, M. D. Fast protein dynamics probed with infrared vibrational echo experiments. *Annu. Rev. Phys. Chem.* **2001**, *52*, 315-356.

[17] Chin, J. K.; Jimenez, R.; Romesberg, F. E. Direct observation of protein vibrations by selective incorporation of spectroscopically observable carbon-deuterium bonds in cytochrome C. *J. Am. Chem. Soc.* **2001**, *123*, 2426-2427.

[18] Chin, J. K.; Jimenez, R.; Romesberg, F. E. Protein dynamics and cytochrome c: Correlations between ligand vibrations and redox activity. *J. Am. Chem. Soc.* **2002**, *124*, 1846-1847.

[19] Ye, X.; Demidov, A.; Champion, P. M. Measurements of the photodissociation quantum yields of MbNO and MbO(2) and the vibrational relaxation of the six-coordinate heme species. *J. Am. Chem. Soc.* **2002**, *124*, 5914-5924.

[20] Xie, A.; van der Meer, A. F. G.; Austin, R. H. Excited-state lifetimes of far-infrared collective modes in proteins. *Phys. Rev. Lett.* **2002**, *88*, 018102-1-4

[21] Merchant, K. A.; Noid, W. G.; Thompson, D. E.; Akiyama, R.; Loring, R. F.; Fayer, M. D. Structural assignments and dynamics of the A substates of MbCO: Spectrally resolved vibrational echo experiments and molecular dynamics simulations. *J. Phys. Chem. B* **2003**, *107*, 4-7.

[22] Sagle, L. B.; Zimmermann, J.; Dawson, P. E.; Romesberg, F. E. A high-resolution probe of protein folding. *J. Am. Chem. Soc.* **2004**, *126*, 3384-3385.

[23] Makri, N. Time-dependent quantum methods for large systems. *Annu. Rev. Phys. Chem.* **1999**, *50*, 167-191.

[24] Thoss, M.; Wang, H. Semiclassical description of molecular dynamics based on initial-value representation methods. *Annu. Rev. Phys. Chem.* **2004**, *55*, 299-332.

[25] Feynman, R. P. Space-Time Approach to Non-Relativistic Quantum Mechanics. *Rev. Mod. Phy.* **1948**, *20*, 367.

[26] Frenkel, D.; Smit, B. *Understanding molecular simulation from algorithm to applications*, 2^{nd} ed.; Academic Press: New York, 2002; pp 165-199.

[27] Grossfield, A. An implementation of WHAM : the Weighted Histogram Analysis Method. *"WHAM: an implementation of the weighted histogram analysis method", http://membrane.urmc.rochester.edu/content/wham/, version 2.0.6.*

[28] Wang, H.; Sun, X.; Miller, W. H. Semiclassical approximations for the calculation of thermal rate constants for chemical reactions in complex molecular systems. *J. Chem. Phys.* **1998**, *108*, 9726.

[29] Sun, X.; Miller, W. H. Mixed semiclassical-classical approaches to the dynamics of complex molecular systems. *J. Chem. Phys.* **1997**, *106*, 916.

[30] Wang, H.; Thoss, M.; Miller, W. H. Forward-backward initial value representation for the calculation of thermal rate constants for reactions in complex molecular systems. *J. Chem. Phys.* **2000**, *112*, 47.

[31] Sun, X.; Wang, H.; Miller, W. H. Semiclassical theory of electronically nonadiabatic dynamics: Results of a linearized approximation to the initial value representation. *J. Chem. Phys.* **1998**, *109*, 7064.

[32] Wang, H.; Song, X.; Chandler, D.; Miller, W. H. Semiclassical study of electronically nonadiabatic dynamics in the condensed-phase: Spin-boson problem with Debye spectral density. *J. Chem. Phys.* **1999**, *110*, 4828.

[33] Sun, X.; Miller, W. H. Forward-backward initial value representation for semiclassical time correlation functions. *J. Chem. Phys.* **1999**, *110*, 6635.

[34] Pollak, E.; Liao, J. A new quantum transition state theory. *J. Chem. Phys.* **1998**, *108*, 2733.

[35] Miller, W. H. A classical S-Matrix - numerical application to inelastic collisions. *J. Chem. Phys.* **1970**, *53*, 3578.

[36] Oxtoby, D. W. Vibrational relaxation in liquids. *Annu. Rev. Phys. Chem.* **1981**, *32*, 77.

[37] Oxtoby, D. W. Vibrational relaxation in liquids: Quantum states in a classical bath. *J. Phys. Chem.* **1983**, *87*, 3028.

[38] Elsaesser, T.; Kaiser, W. Vibrational and vibronic relaxation of large polyatomic molecules in liquids. *Annu. Rev. Phys. Chem.* **1991**, *42*, 83.

[39] Bader, J. S.; Berne, B. J. Quantum and classical relaxation rates from classical simulations. *J. Chem. Phys.* **1994**, *100*, 8359.

[40] Owrutsky, J. C.; Raftery, D.; Hochstrasser, R. M. Vibrational relaxation dynamics in solutions. *Annu. Rev. Phys. Chem.* **1994**, *45*, 519.

[41] Tokmakoff, A.; Sauter, B.; Fayer, M.D. Temperature-dependent vibrational relaxation in polyatomic liquids: Picosecond infrared pump-probe experiments. *J. Chem. Phys.* **1994**, *100*, 9035.

[42] Tokmakoff, A.; Fayer, M. D. Homogeneous vibrational dynamics and inhomogeneous broadening in glass-forming liquids: Infrared photon-echo experiments from room temperature to 10 K. *J. Chem. Phys.* **1995**, *103*, 2810.

[43] Stratt, R. M.; Maroncelli, M. Nonreactive dynamics in solution: The emerging molecular view of solvation dynamics and vibrational relaxation. *J. Phys. Chem.* **1996**, *100*, 12981-12996.

[44] Deng, Y.; Stratt, R. M. Vibrational energy relaxation of polyatomic molecules in liquids: The solvent's perspective. *J. Chem. Phys.* **2002**, *117*, 1735.

[45] Deng, Y.; Stratt, R. M. High-frequency vibrational energy relaxation in liquids: The foundation of the instantaneous-pair theory and some generalizations. *J. Chem. Phys.* **2002** *117*, 10752.

[46] Heilweil, E. J.; Doany, F. E.; Moore, R.; Hochstrasser, R. M. Vibrational energy relaxation of the cyanide ion in aqueous solution. *J. Chem. Phys.* **1982**, *76*, 5632.

[47] Chesnoy, J.; Ricard, D. Vibrational energy relaxation of high-density HBr fluid in the 186-366 K range. *Chem. Phys. Lett.* **1982**, *92*, 449.

[48] Chesnoy, J.; Ricard, D. Vibrational energy relaxation of high density HCl fluid in the 150-345 K range. *Chem. Phys.* **1982**, *67*, 347.

[49] Heilweil, E. J.; Casassa, M.P.; Cavanagh, R. R.; Stephenson, J. C. Population lifetimes of $OH(\mathrm{v} = 1)$ and $OD(\mathrm{v} = 1)$ stretching vibrations of alcohols and silanols in dilute solution. *J. Chem. Phys.* **1986**, *85*, 5004-5018.

[50] Owrutsky, J. C.; Kim, Y. R.; Li, M.; Sarisky, M. J.; Hochstrasser, R. M. Determination of the vibrational energy relaxation time of the azide ion in protic solvents by 2-color transient infrared spectroscopy. *Chem. Phys. Lett.* **1991**, *184*, 368.

[51] Owrutsky, J. C.; Li, M.; Locke, B.; Hochstrasser, R. M. Vibrational Relaxation of the CO Stretch Vibration in Hemoglobin-CO, Myoglobin-CO, and Protoheme-CO. *J. Phys. Chem.* **1995**, *99*, 4842.

[52] P. Hamm, M. Lim, and R. M. Hochstrasser. Vibrational energy relaxation of the cyanide ion in water. *J. Chem. Phys.* **1997**, *107*, 15023–15031.

[53] Lawrence, C. P.; Skinner, J. L. Vibrational spectroscopy of HOD in liquid D_2O. III Spectral diffusion, and hydrogen bonding and rotational dynamics. *J. Chem. Phys.* **2003**, *118*, 264.

[54] Ka, B. J.; Geva, E. Classical vs. quantum vibrational energy relaxation pathways in solvated polyatomic molecules. *J. Phys. Chem. A* **2006**, *110*, 13131.

[55] Rey, R.; Hynes, J. T. Vibrational energy relaxation of HOD in liquid D_2O. *J. Chem. Phys.* **1996**, *104*, 2356.

[56] Navrotskaya, I.; Geva, E. Vibrational energy relaxation rates of H_2 and D_2 in liquid argon via the linearized semiclassical method. *J. Phys. Chem. A* **2007**, *111*, 460-467.

[57] Navrotskaya, I.; Geva, E. Comparison between the landau-teller and flux-flux methods for computing vibrational energy relaxation rate constants in the condensed phase. *J. Chem. Phys.* **2007**, *127*, 054504.

[58] Shiga, M.; Okazaki, S. A molecular dynamics study of the vibrational energy relaxation of the cyanide ion in aqueous solution. *Chem. Phys. Lett.* **1998**, *292*, 431.

[59] Rey, R.; Hynes, J. T. Vibrational energy and phase relaxation of CN^- in water. *J. Chem. Phys.* **1998**, *108*, 142-153.

[60] Egorov, S. A.; Everitt, K. F.; Skinner, J. L. Quantum dynamics and vibrational relaxation. *J. Phys. Chem. A* **1999**, *103*, 9494.

[61] Jang, S.; Pak, Y.; Voth, G. A. Quantum dynamical simulation of the energy relaxation rate of the CN^- ion in water. *J. Phys. Chem. A* **1999**, *103*, 10289-10293.

[62] Shi, Q.; Geva, E. Vibrational energy relaxation in liquid oxygen from a semiclassical molecular dynamics simulation. *J. Phys. Chem. A* **2003**, *107*, 9070-9078.

[63] Vazquez, F. X.; Navrotskaya, I.; Geva, E. Vibrational energy relaxation rate constants via the linearized semiclassical method without force derivatives. *J. Phys. Chem. A* **2010**, *114*, 5682-5688.

[64] Lawrence, C. P.; Skinner, J. L. Vibrational spectroscopy of HOD in liquid D_2O. I. vibrational energy relaxation. *J. Chem. Phys.* **2002**, *117*, 5827.

[65] Shiga, M.; Okazaki, S. Molecular dynamics study of vibrational energy relaxation of CN^- in H_2O and D_2O solutions: An application of path integral influence functional theory to multiphonon processes. *J. Chem. Phys.* **1999**, *111*, 5390.

[66] Mikami, T.;Shiga, M.; Okazaki, S. Quantum effect of solvent on molecular vibrational energy relaxation of solute based upon path integral influence functional theory. *J. Chem. Phys.* **2001**, *115*, 9797-9807.

[67] Skinner, J. L.; Park, K. Calculating vibrational energy relaxation rates from classical molecular dynamics simulations: Quantum correction factors for processes involving vibration-vibration energy transfer. *J. Phys. Chem. B* **2001**, *105*, 6716-6721.

[68] Sato, M.; Okazaki, S. Vibrational relaxation time of CN^- ion in water studied by mixed quantum-classical molecular dynamics: Comparison with Fermi's golden rule and influence functional theory. *Mol. Simul.* **2004**, *30*, 835-839.

[69] Sagnella, D. E.; Straub, J. E.; Jackson, T. A.; Lim, M.; Anfinrud, P. A. Vibrational population relaxation of carbon monoxide in the heme pocket of photolyzed carbonmonoxy myoglobin: Comparison of time-resolved mid-IR absorbance experiments and molecular dynamics simulations. *Proc. Natl. Acad. Sci. USA* **1999**, *96*, 14324.

[70] Sato, M.; Okazaki, S. Mixed quantum classical molecular dynamics study of vibrational relaxation of CN^- ion in water: an analysis of coupling as function of time. *J. Mol. Liquids* **2005**, *119*, 15.

[71] Bastida, A.; Cruz, C. S.; Zuniga, J.; Requena, A.; Miguel, B. The Ehrenfest method with quantum corrections to simulate the relaxation of molecules in solution: Equilibrium and dynamics. *J. Chem. Phys.* **2007**, *126*, 014503.

[72] Okamoto, Y.; Mikami, T.; Yoshii, N.; Okazaki, S. A molecular analysis of the vibrational energy relaxation mechanism of the CN ion in water based upon path integral influence functional theory combined with a dipole expansion of the solutesolvent interaction. *J. Mol. Liq.* **2007**, *134*, 34.

[73] Bastida, A.; Zuniga, J.; Requena, A.; Miguel, B. Full quantum vibrational simulation of the relaxation of the cyanide ion in water using the Ehrenfest method with quantum corrections. *J. Chem. Phys.* **2008**, *129*, 154501.

[74] Skinner, J. L. Vibrational energy relaxation of small molecules and ions in liquids. *Theor. Chem. Acc.* **2011**, *128*, 147.

[75] Lee, M. W.; Meuwly, M. On the role of nonbonded interactions in vibrational energy relaxation of cyanide in water. *J. Phys. Chem. A* **2011**, *115*, 5053-5061.

[76] Ka, B. J.; Geva, E. Vibrational energy relaxation of polyatomic molecules in liquid solution via the linearized semiclassical method. *J. Phys. Chem. A* **2006**, *110*, 9555-9567.

[77] Shi, Q.; Geva, E. Vibrational energy relaxation rate constants from linear response theory. *J. Chem. Phys.* **2003**, *118*, 7562-7571.

[78] Vazquez, F. X.; Talapatra, S.; E. Geva, E. Vibrational energy relaxation in liquid HCl and DCl via the linearized semiclassical method: Electrostriction versus quantum delocalization. *J. Phys. Chem. A* **2011**, *115*, 9775-9781.

[79] Zwanzig, R. Theory of vibrational relaxation in liquids. *J. Chem. Phys.* **1961**, *34*, 1931-1935.

[80] Stock, G. Classical simulation of quantum energy flow in biomolecules. *Phys. Rev. Lett.* **2009**, *102*, 118301.

[81] Leitner, D. M. Energy flow in proteins. *Annu. Rev. Phys. Chem.* **2008**, *59*, 233.

[82] Terashima, T.; Shiga, M.; Okazaki, S. A mixed quantum-classical molecular dynamics study of vibrational relaxation of a molecule in solution. *J. Chem. Phys.* **2001**, *114*, 5663-5673.

[83] Fujisaki, H.; Zhang, Y.; Straub, J. E. Time-dependent perturbation theory for vibrational energy relaxation and dephasing in peptides and proteins. *J. Chem. Phys.* **2006**, *124*, 144910.

[84] Benjamin, I.; Whitnell, R. M. Vibrational relaxation of I_2^- in water and Ethanol: Molecular dynamics simulation. *Chem. Phys. Lett.* **1993**, *204*, 45.

[85] Gnanakaran, S.; Hochstrasser, R. M. Vibrational relaxation of HgI in Ethanol: Equilibrium molecular dynamics simulations. *J. Chem. Phys.* **1996**, *105*, 3486.

[86] Ka, B. J.; Shi, Q.; Geva, E. Vibrational energy relaxation rates via the linearized semiclassical approximations: Applications to neat diatomic liquids and atomic-diatomic liquid mixtures. *J. Phys. Chem. A* **2005**, *109*, 5527-5536.

[87] Shi, Q.; Geva, E. A semiclassical theory of vibrational energy relaxation in the condensed phase. *J. Phys. Chem. A* **2003**, *107*, 9059-9069.

[88] Schofield,P. Space-time correlation function formalism for slow neutron scattering. *Phys. Rev. Lett.* **1960**, *4*, 239.

[89] Bu, L.; Straub, J. E. Vibrational frequency shifts and relaxation rates for a selected vibrational mode in cytochrome c. *Biophys. J.* **2003**, *85*, 1429.

[90] Oxtoby, D. W. Vibrational population relaxation in liquids. *Adv. Chem. Phys.* **1981**, *47* (Part 2), 487.

[91] Ferrario, M.; McDonald, I.; Symons, M. C. R. Solvent-solute hydrogen bonding in dilute solutions of CN^- and CH_3CN in water and methanol. *Mol. Phys.* **1992**, *77*, 617.

[92] Parker, M. E.; Heyes, D. M. Molecular dynamics simulations of stretched water: Local structure and spectral signatures. *J. Chem. Phys.* **1998**, *108*(21), 9039.

[93] Jang, S.; Voth, G. A. Path integral centroid variables and the formulation of their exact real time dynamics. *J. Chem. Phys.* **1999**, *111*, 2357.

[94] Jang, S.; Voth, G. A. A derivation of centroid molecular dynamics and other approximate time evolution methods for path integral centroid variables. *J. Chem. Phys.* **1999**, *111*, 2371.

[95] Lobaugh, J.; Voth, G. A. A quantum model for water: Equilibrium and dynamical properties. *J. Chem. Phys.* **1997**, *106*, 2400.

[96] Jorgensen, W. L.; Chandrasekhar, J.; Madura, J. D.; Impey, R. W.; Klein, M. L. Comparison of simple potential functions for simulating liquid water. *J. Chem. Phys.* **1983**, *79*, 926, 1983.

[97] Kumagai, N.; Kawamura, K.; Yokokawa, T. An interatomic potential model for H_2O - Applications to water and ice polymorphs. *Mol. Simul.* **1994**, *12*, 177-186, 1994.

[98] Makri, N. Time-dependent quantum methods for large systems. *Annu. Rev. Phys. Chem.* **1999**, *50*, 167.

[99] Berne, B. J.; Jortner, J.; Gordon, R. Vibrational relaxation of diatomic molecules in gases and liquids. *J. Chem. Phys.* **1967**, *47*, 1600.

[100] Egorov, S. A.; Skinner, J. L. Vibrational energy relaxation of polyatomic solutes in simple liquids. *J. Chem. Phys.* **2000**, *112*, 275.

[101] Rostkier-Edelstein, D.; Graf, P.; Nitzan, A. Computing vibrational energy relaxation for high frequency modes in condensed environments. *J. Chem. Phys.* **1997**, *107*, 10470.

[102] Rostkier-Edelstein, D.; Graf, P.; Nitzan, A. Erratum: Computing vibrational energy relaxation for high frequency modes in condensed environments (J. Chem. Phys. **107**, 10470 (1997)). *J. Chem. Phys.* **1998**, *108*, 9598.

[103] Everitt, K. F.; Skinner, J. L.; Ladanyi, B. M. Vibrational energy relaxation in liquid oxygen (revisited) and in liquid nitrogen. *J. Chem. Phys.* **2002**, *116*, 179-183.

[104] Berens, P. H.; White, S. R.; Wilson, K. R. Molecular dynamics and spectra. *J. Chem. Phys.* **1981**, *75*, 515.

[105] Frommhold, L. *Collision-induced absorption in gases*, volume 2 of *Cambridge Monographs on Atomic, Molecular, and Chemical Physics*. Cambridge University Press, England, 1st edition, 1993.

[106] Skinner, J. L. Semiclassical approximations to golden rule rate constants. *J. Chem. Phys.* **1997**, *107*, 8717.

[107] An, S. C.; Montrose, C. J.; Litovitz, T. A. Low frequency structure in depolarized spectrum of Argon. *J. Chem. Phys.* **1976**, *64*, 3717.

[108] Egorov, S. A.; Skinner, J. L. Semiclassical approximations to quantum correlation functions. *Chem. Phys. Lett.* **1998**, *293*, 469-476.

[109] Egelstaff, P. A. Neutron scattering studies of liquid diffusion. *Adv. Phys.* **1962**, *11*, 203.

[110] Kneller, G. R. Inelastic neutron scattering from classical systems: Stationary phase approximation of the scattering law. *Mol. Phys.* **1994**, *83*, 63.

[111] Cieplak, P.; Dupradeau, F.-Y.; Duan, Y.; Wang, J. Polarization effects in molecular mechanical force fields. *J. Phys.:Condens. Matter* **2009**, *21*, 333102.

[112] Comell, W. D.; Cieplak, P.; Bayly, C. I.; Kollman, P. A. Application of resp charges to calculate conformational energies, hydrogen bond energies, and free energies of solvation. *J. Am. Chem. Soc.* **1993**, *115*, 9620.

[113] Cieplak, P.; Cornell, W. D.; Christopher, B.; Kollman, P. A. Multiconformational RESP Methodology to Biopolymers : Charge Derivation for. *J. Comput. Chem.* **1995**, *16*, 1357-1377.

[114] Bayly, C. I.; Cieplak, P.; Cornell, W. D.; Kollman, P. A. A well-behaved electrostatic potential based method using charge restraints for deriving atomic charges: The resp model. *J. Phys. Chem.* **1993**, *97*, 10269-10280.

[115] Ryckaert, J.-P.; Ciccotti, G.; Berendsen, H. J. C. Numerical integration of the cartesian equations of motion of a system with constraints: molecular dynamics of n-alkanes. *J. Comp. Phys.* **1977**, *23*, 327 - 341.

[116] Berendsen, H. J. C.; Grigera, J. R.; Straatsma, T. P. The Missing Term in Effective Pair Potentialst. *J. Phys. Chem.* **1987**, *91*, 6269.

[117] Wu, Y.; Tepper, H. L.; Voth, G. A. Flexible simple point-charge water model with improved liquid-state properties. *J. Chem. Phys.* **2006**, *124*, 024503.

[118] Andrea, T. A.; Swope, W. C.; Andersen, H. C. The role of long ranged forces in determining the structure and properties of liquid water. *J. Chem. Phys.* **1983**, *79*, 4576 - 4584.

[119] Ladanyi, B. M.; Stratt, R. M. On the role of dielectric friction in vibrational energy relaxation. *J. Chem. Phys.* **1999**, *111*, 2008.

[120] Nguyen, P. H.; Stock, G. Nonequilibrium molecular-dynamics study of the vibrational energy relaxation of peptides in water nonequilibrium molecular-dynamics study of the vibrational energy relaxation of peptides in water. *J. Chem. Phys.* **2003**, *119*, 11350.

[121] Fang, Y.; Shigeto, S.; Seong, N.-H.; Dlott, D. D. Vibrational energy dynamics of glycine, N-methylacetamide, and benzoate anion in aqueous (D_2O) solution. *J. Phys. Chem. A* **2009**, *113*, 75.

[122] Shi, Q.; Geva, E. A relationship between semiclassical and centroid correlation functions. *J. Chem. Phys.* **2003**, *118*, 8173-8184.

[123] Talapatra, S; Geva, E. Vibrational lifetimes of cyanide ion in aqueous solution from molecular dynamics simulations: Intermolecular vs. intramolecular accepting modes. *J. Phys. Chem. B* **2014**, *118*, 7395-7404.

[124] Sun, X.; Wang, H.; Miller, W. H. On the semiclassical description of quantum coherence in thermal rate constants. *J. Chem. Phys.* **1998**, *109*, 4190–4200.

[125] Talapatra, S; Geva, E. Vibrational lifetimes of cyanide ion in aqueous solution via the linearized semiclassical method. *J. Phys. Chem. B* **2014**, **In press**.

[126] Vazquez, F. X.; Talapatra, S; Sension, R. J.; Geva, E. The Entropic Origin of Solvent Effects on The Single Bond *cZt-tZt* Isomerization Rate Constant of 1,3,5-*cis*-Hexatriene in Alkane and Alcohol Solvents: A Molecular Dynamics Study *J. Phys. Chem. B* **2014**, *118*, 7869-7877.

[127] Faltermeier, B.; Protz, R.; Maier, M. Concentration and temperature-dependence of electronic and vibrational-energy relaxation of O_2 in liquid-mixtures. *Chem. Phys.* **1981**, *62*, 377.

[128] Brueck, S. R. J.; Osgood, R. M. Vibrational energy relaxation in liquid N_2-CO mixtures. *Chem. Phys. Lett.* **1976**, *39*, 568.

[129] Chateau, M.; Delalande, C.; Frey, R.; Gale, G. M.; Pradère, F. Vibrational population relaxation of compressed $^nH_2$ fluid in the 15-110 K range. *J. Chem. Phys.* **1979**, *71*, 4799.

[130] Delalande, C.; Gale, G. M. Semi-classical model for vibrational-energy relaxation in simple liquids and compressed fluids. *J. Chem. Phys.* **1979**, *71*, 4804.

[131] Delalande, C.; Gale, G. M. Vibrational-energy relaxation in fluid mixtures - hydrogen in argon. *J. Chem. Phys.* **1980**, *73*, 1918.

[132] Faltermeier, B.; Protz, R.; Maier, M.; Werner, E. Vibrational-energy relaxation of O_2 in liquid-mixtures with Ar and N_2. *Chem. Phys. Lett.* **1980**, *74*, 425.

[133] Chesnoy, J.; Gale, G. M. *Adv. Chem. Phys.* **1988**, *70 (part 2)*, 297.

[134] Harris, C. B.; Smith, D. E.; Russell, D. J. Vibrational-relaxation of diatomic-molecules in liquids. *Chem. Rev.* **1990**, *90*, 481.

[135] Miller, D. W.; Adelman, S. A. Vibrational-energy transfer in fluids. *Int. Rev. Phys. Chem.* **1994**, *13*, 359.

[136] Calaway, W. F.; Ewing, G. E. *J. Chem. Phys.* **1975**, *63*, 2842.

[137] Laubereau, A.; Kaiser, W. Vibrational dynamics of liquids and solids investigated by picosecond light-pulses. *Rev. Mod. Phys.* **1978**, *50*, 607.

[138] Roussignol, P.; Delalande, C.; Gale, G. M. Vibrational-relaxation of deuterium in argon fluid. *Chem. Phys.* **1982**, *70*, 319.

[139] Heilweil, E. J.; Casassa, M. P.; Cavanagh, R. R.; Stephenson, J. C. Temperature-dependence of the vibrational population lifetime of OH($\upsilon = 1$) in fused-silica. *Chem. Phys. Lett.* **1985**, *117*, 185.

[140] Harris, A. L.; Brown, J. K.; Harris, C. B. The nature of simple photodissociation reactions in liquids on ultrafast time scales. *Annu. Rev. Phys. Chem* **1988**, *39*, 341.

[141] Paige, M. E.; Russell, D. J.; Harris, C. B. Studies of chemical-reactivity in the condensed phase .2. vibrational-relaxation of iodine in liquid Xenon following geminate recombination. *J. Chem. Phys.* **1986**, *85*, 3699.

[142] Moustakas, A.; Weitz, E. Vibrational-relaxation of hcl as a function of xenon density - the role of HCl-Xe complexes. *J. Chem. Phys.* **1993**, *98*, 6947.

[143] Kliner, D. A. V.; Alfano, J. C.; Barbara, P. F. Photodissociation and vibrational-relaxation of I_2^- in ethanol. *J. Chem. Phys.* **1993**, *98*, 5375.

[144] Zimdars, D.; Tokmakoff, A.; Chen, S.; Greenfield, S. R.; Fayer, M. D. Picosecond infrared vibrational photon-echoes in a liquid and glass using a free-electron laser. *Phys. Rev. Lett.* **1993**, *70*, 2718.

[145] Pugliano, N.; Szarka, A. Z.; Gnanakaran, S.; Hochstrasser, R. M. Vibrational population-dynamics of the hgi photofragment in ethanol solution. *J. Chem. Phys.* **1995**, *103*, 6498.

[146] Paige, M. E.; Harris, C. B. Ultrafast studies of chemical-reactions in liquids - validity of gas-phase vibrational-relaxation models and density dependence of bound electronic state lifetimes. *Chem. Phys.* **1990**, *149*, 37.

[147] Salloum, A.; Dubost, H. Vibrational-energy transfer from CO to O_2 in rare-gas matrices .1. vibrational-excitation and relaxation of O_2 (X, V=4-20). *Chem. Phys.* **1994**, *189*, 179.

[148] Urdahl, R. S.; Myers, D. J.; Rector, K. D.; Davis, P. H.; Cherayil, B. J.; Fayer, M. D. Vibrational lifetimes and vibrational line positions in polyatomic supercritical fluids near the critical point. *J. Chem. Phys.* **1997**, *107*, 3747.

[149] Owrutsky, J. C.; Li, M.; Locke, B.; Hochstrasser, R. M. Vibrational-relaxation of the CO stretch vibration in hemoglobin-CO, myoglobin-CO, and protoheme-CO. *J. Phys. Chem.* **1995**, *99*, 4842.

[150] Laenen, R.; Rauscher, C.; Laubereau, A. Dynamics of local substructures in water observed by ultrafast infrared hole burning. *Phys. Rev. Lett.* **1998**, *80*, 2622.

[151] Woutersen, S.; Emmerichs, U.; Nienhuys, H.; Bakker, H. J. Anomalous temperature dependence of vibrational lifetimes in water and ice. *Phys. Rev. Lett.* **1998**, *81*, 1106.

[152] Myers, D. J.; Urdahl, R. S.; Cherayil, B. J.; Fayer, M. D. Temperature dependence of vibrational lifetimes at the critical density in supercritical mixtures. *J. Chem. Phys.* **1997**, *107*, 9741.

[153] Myers, D. J.; Chen, S.; Shigeiwa, M.; Cherayil, B. J.; Fayer, M. D. Temperature dependent vibrational lifetimes in supercritical fluids near the critical point. *J. Chem. Phys.* **1998**, *109*, 5971.

[154] Sibert III, E. L.; Rey, R. Vibrational relaxation in liquid chloroform following ultrafast excitation of the CH stretch fundamental. *J. Chem. Phys.* **2002**, *116*, 237.

[155] Zwanzig, R. Theory of vibrational relaxation in liquids. *J. Chem. Phys.* **1961**, *34*, 1931.

[156] Hillery, M.; O'Connell, R. F.; Scully, M. O.; Wigner, E. P. Distribution-functions in physics - fundamentals. *Phys. Rep.* **1984**, *106*(3), 121.

[157] Berne, B. J.; Thirumalai, D. On the simulation of quantum-systems - path integral methods. *Annu. Rev. Phys. Chem.* **1986**, *37*, 401.

[158] Ceperley, D. M. Path-integrals in the theory of condensed helium. *Rev. Mod. Phys.* **1995**, *67*, 279.

[159] Chesnoy, J.; Richard, D. Vibrational-energy relaxation of high-density hbr fluid in the 186-366 K range. *Chem. Phys. Lett.* **1982**, *92*, 449.

[160] Whitnell, R. M.; Wilson, K. R.; Hynes, J. T. Fast vibrational-relaxation for a dipolar molecule in a polar-solvent. *J. Phys. Chem.* **1990**, *94*, 8625.

[161] Whitnell, R. M.; Wilson, K. R.; Hynes, J. T. Vibrational-relaxation of a dipolar molecule in water. *J. Chem. Phys.* **1992**, *96*, 5354.

[162] Bruehl, M.; Hynes, J. T. Vibrational-relaxation times for a model hydrogen-bonded complex in a polar-solvent. *Chem. Phys.* **1993**, *175*, 205.

[163] Chorny, I.; Vieceli, J.; Benjamin, I. Molecular dynamics study of the vibrational relaxation of OClO in bulk liquids. *J. Chem. Phys.* **2002**, *116*, 8904.

[164] Ferrario, M.; Klein, M. L.; McDonald, I. R. Dynamical behavior of the azide ion in protic solvents. *Chem. Phys. Lett.* **1993**, *213*, 537.

[165] Morita, A.; Kato, S. Vibrational relaxation of azide ion in water: The role of intramolecular charge fluctuation and solvent-induced vibrational coupling. *J. Chem. Phys.* **1998**, *109*, 5511.

[166] Gulmen, T. S.; Sibert III, E. L. Vibrational energy relaxation of the OH stretch in liquid methanol. *J. Phys. Chem. A* **2004**, *108*, 2389.

[167] Gulmen, T. S.; Sibert III, E. L. Fluctuating energy level Landau-Teller theory: Application to the vibrational energy relaxation of liquid methanol. *J. Phys. Chem. A* **2005**, *109*, 5777-5780.

[168] Laage, D.; Demirdjian, H.; Hynes, J. T. Intermolecular vibration-vibration energy transfer in solution: Hydrogen fluoride in water. *Chem. Phys. Lett.* **2005**, *405*, 453.

[169] Chorny, I.; Benjamin, I. Molecular dynamics study of the vibrational relaxation of OCl and OCl- in the bulk and the surface of water and acetonitrile. *J. Mol. Liq.* **2004**, *110*, 133.

[170] Vieceli, J.; Chorny, I.; Benjamin, I. Vibrational relaxation at water surfaces. *J. Chem. Phys.* **2002**, *117*, 4532.

[171] Lim, M.; Gnanakaran, S.; Hochstrasser, R. M. Charge shifting in the ultrafast photoreactions of ClO^- in water. *J. Chem. Phys.* **1997**, *106*, 3485.

[172] Nitzan, A.; Mukamel, S.; Jortner, J. Some features of vibrational-relaxation of a diatomic molecule in a dense medium. *j. chem. phys.* **1974**, *60*, 3929.

[173] Nitzan, A.; Mukamel, S.; Jortner, J. Energy-gap law for vibrational-relaxation of a molecule in a dense medium. *J. Chem. Phys.* **1975**, *63*, 200.

[174] Graener, H.; Seifert, G.; Laubereau, A. New spectroscopy of water using tunable picosecond pulses in the infrared. *Phys. Rev. Lett.* **1991**, *66*, 2092.

[175] Vodopyanov, K. L. Saturation studies of H_2O and HDO near 3400 cm-1 using intense picosecond laser-pulses. *J. Chem. Phys.* **1991**, *94*, 5389.

[176] Nienhuys, H.; Woutersen, S.; van Santen, R. A.; Bakker, H. J. Mechanism for vibrational relaxation in water investigated by femtosecond infrared spectroscopy. *J. Chem. Phys.* **1999**, *111*, 1494.

[177] Deak, J. C.; Rhea, S. T.; Iwaki, L. K.; Dlott, D. D. Vibrational energy relaxation and spectral diffusion in water and deuterated water. *J. Phys. Chem. A* **2000**, *104*, 4866.

[178] Rey, R.; Hynes, J. T. Ultrafast vibrational population dynamics of water and related systems: A theoretical perspective. *Chem. Rev.* **2004**, *104*, 1915.

[179] Wang, Z.; Pakoulev, A.; Pang, Y.; Dlott, D. D. Vibrational substructure in the OH stretching band of water. *Chem. Phys. Lett.* **2003**, *378*, 281.

[180] Pakoulev, A.; Wang, Z.; Dlott, D. D. Vibrational relaxation and spectral evolution following ultrafast OH stretch excitation of water. *Chem. Phys. Lett.* **2003**, *371*, 594-600.

[181] Pakoulev, A.; Wang, Z.; Pang, Y.; Dlott, D. D. Vibrational energy relaxation pathways of water. *Chem. Phys. Lett.* **2003**, *380*, 404.

[182] Kim, J.; Tao, J. H.; White, J. L.; Petrovic, V. S.; Martinez, T. J.; Bucksbaum, P. H. Control of 1 , 3-Cyclohexadiene Photoisomerization Using Light-Induced Conical Intersections. *J. Phys. Chem. A*, **2012**, *116*, 2758-2763.

[183] Deb S.; Weber, P. M. Conical intersection,femtosecond dynamics,orbital symmetry,photochemical interconversion. *Annu. Rev. Phys. Chem.*, **2011**, *62*, 19-39.

[184] Li, A.; Yuan, S.; Dou, Y.; Wang, Y.; Wen, Z. Semiclassical dynamic simulation of photon induced ring-opening of cyclohexadiene to hexatriene. *Chem. Phys. Lett.*, **2009**, *478*, 28-32.

[185] Dou, Y.; Yuan, S.; Lo, G. V. Ring opening reaction of 1,3-cyclohexadiene studied by semiclassical dynamics simulation. *Appl. Surf. Sci.*, **2007**, *253*, 6404-6408.

[186] Carroll, E. C.; Pearson, B. J.; Florean, A. C.; Bucksbaum, P. H.; Sension, R. J. Spectral phase effects on nonlinear resonant photochemistry of 1,3-cyclohexadiene in solution. *J. Chem. Phys.*, **2006**, *124*, 114506 (10 pages).

[187] Harris, D. A.; Orozco, M. B.; Sension, R. J. Solvent dependent conformational relaxation of cis-1,3,5-hexatriene. *J. Phys. Chem. A*, **2006**, *110*, 9325-9333.

[188] Tamura, H.; Nanbu, S.; Nakamura, H.; Ishida, T A theoretical study of cyclohexadiene/hexatriene photochemical interconversion: multireference configuration interaction potential energy surfaces and transition probabilities for the radiationless decays. *Chem. Phys. Lett.*, **2005**, *401*, 487-491.

[189] Blomgren, F.; Larsson, S. Using 1,3-butadiene and 1,3,5-hexatriene to model thecis-trans isomerization of retinal, the chromophore in the visual pigment rhodopsin. *Int. J. Quantum Chem.*, **2002**, *90*, 1536.

[190] Anderson, N. A.; Durfee, C. G; Murnane, M. M.; Kapteyn, H. C.; Sension, R. J. The internal conversions of trans- and cis-1,3,5-hexatriene in cyclohexane solution studied with sub-50 fs UV pulses. *Chem. Phys. Lett.*, **2000**, *323*(3-4), 365-371.

[191] Anderson, N. A.; Pullen, S. H.; Walker II, L. A.; Shiang, J. J.; Sension, R. J. Ultrafast polyene dynamics in solution: The conformational relaxation and thermalization of highly excited cis-1,3,5- hexatriene as a function of initial conformation and solvent. *J. Phys. Chem. A*, **1998**, *102*(52), 10588-10598.

[192] Lochbrunner, S.; Fuss, W.; Schmid, W. E.; Kompa, K. L. Electronic relaxation and ground-state dynamics of 1,3- cyclohexadiene and cis-hexatriene in ethanol. *J. Phys. Chem. A*, **1998**, *102*(47), 9334-9344.

[193] Pullen, S. H.; Anderson, N. A.; Walker II, L. A.; Sension, R. J. The ultrafast photochemical ring-opening reaction of 1,3- cyclohexadiene in cyclohexane. *J. Chem. Phys.*, **1998**, *108*(2), 556-563.

[194] Pullen, S. H.; Anderson, N. A.; Walker II, L. A.; Sension, R. J. The ultrafast ground and excited state dynamics of cis-hexatriene in cyclohexane. *J. Chem. Phys.*, **1997**, *107*(13), 4985-4993.

[195] Sakai, S.; Takane, S. Theoretical Studies of the Electrocyclic Reaction Mechanisms of Hexatriene to Cyclohexadiene. *J. Phys. Chem. A*, **1999**, *103*, 2878-2882.

[196] Ohta, K.; Naitoh, Y.; Tominaga, K.; Hirota, N.; Yoshihara, K. Femtosecond transient absorption studies of trans- and cis-1,3,5-hexatriene in solution. *J. Phys. Chem. A*, **1998**, *102*(1), 35-44.

[197] Woywod, C.; Livingood, W. C.; Frederick, J. H. S[sub 1]S[sub 2] vibronic coupling in trans-1,3,5-hexatriene. I. Electronic structure calculations. *J. Chem. Phys.*, **2000**, *112*, 613-625.

[198] Woywod, C.; Livingood, W. C.; Frederick, J. H. S[sub 1]S[sub 2] vibronic coupling in trans-1,3,5-hexatriene. II. Theoretical investigation of absorption and resonance Raman spectra. *J. Chem. Phys.*, **2000**, *112*, 626-640.

[199] Woywod, C.; Livingood, W. C.; Frederick, J. H. S[sub 1]S[sub 2] vibronic coupling in cis-1,3,5-hexatriene. I. Electronic structure calculations. *J. Chem. Phys.*, **2001**, *114*, 1631-1644.

[200] Woywod, C.; Snyder, J. A.; Frederick, J. H. Out-of-Plane Modes of cis-1 , 3 , 5-Hexatriene : Frequency Shifts in the 2 1 A 1 and 1 1 B 1 Excited. *J. Phys. Chem. A*, **2001**, *105*, 2903-2910.

[201] Celani, P.; Bernardi, F.; Robb, M. A.; Olivucci, M. Do photochemical ring-openings occur in the spectroscopic state? 1b 2pathways for the cyclohexadiene/hexatriene photochemical interconversion. *J. Phys. Chem.*, **1996**, *100*, 19364-19366.

[202] Garavelli, M.; Celani, P.; Fato, M.; Bearpark, M. J.; Smith, B. R.; Olivucci, M.; Robb, M. A. Relaxation paths from a conical intersection: The mechanism of product formation in the cyclohexadiene/hexatriene photochemical interconversion. *J. Phys. Chem. A*, **1997**, *101*(11), 2023-2032.

[203] Garavelli, M.; Bernardi, F.; Olivucci, M.; Vreven, T.; Klein, S.; Celani, P.; Robb, M. A. Potential-energy surfaces for ultrafast photochemistry Static and dynamic aspects. *Faraday Discuss.*, **1998**, *110*, 51-70.

[204] Celani, P.; Ottani, S.; Olivucci, M.; Bernardi, F.; Robb, M. A. What happens during the picosecond lifetime of 2a(1) cyclohexa-1,3-diene - A CASS-SCF study of the cyclohexadiene hexatriene photochemical interconversion. *J. Am. Chem. Soc.*, **1994**, *116*(22), 10141-10151.

[205] Garavelli, M.; Page. C. S.; Celani, P.; Olivucci, M.; Schmid, W. E.; Trushin, S. A.; Fuss, W. Reaction path of a sub-200 fs photochemical electrocyclic reaction. *J. Phys. Chem. A*, **2001**, 105(18), 4458-4469.

[206] Braun, M.; Fub, W.; Kompa, K. L.; Wolfrum, J. Improved photosynthesis of previtamin-D by wavelengths of 280- 300 nm. *J. Photochem. Photobiol. A-Chem.*, **1991**, *61*(1), 15-26.

[207] Anderson, N. A.; Sension, R. J. Solvent dependence of excited state lifetimes in 7- dehydrocholesterol and simple polyenes. *In Liquid Dynamics: Experiment, Simulation, and Theory.*; Fourkas, J. Ed.; ACS, **2002**, 148-158.

[208] Anderson, N. A.; Shiang, J. J.; Sension, R. J. Subpicosecond ring opening of 7-dehydrocholesterol studied by ultrafast spectroscopy. *J. Phys. Chem. A*, **1999**, *103*(50), 10730-10736.

[209] Fuss, W.; Hofer, T.; Hering, P.; Kompa, K. L.; Lochbrunner, S.; Schikarski, T.; Schmid, W. E. Ring opening in the dehydrocholesterol previtamin D system studied by ultrafast spectroscopy. *J. Phys. Chem.*, **1996**, *100*(2), 921-927.

[210] Minnaard, N. G.; Havinga, E. Some aspects of solution photochemistry of 1,3-cyclohexadiene, z-1,3,5-hexatriene and (e)-1,3,5-hexatriene. *Recueil Des Travaux Chimiques Des Pays-Bas-Journal Of The Royal Netherlands Chemical Society*, **1973**, *92*(12), 1315-1320.

[211] Kramers, H. Brownian motion in a field of force and the diffusion model of chemical reactions. *Physica*, **1940**, *7*, 284-304.

[212] Hanggi, P.; Talkner, P.; Borkovec, M. Reaction-rate theory - 50 years after Kramers. *Rev. Mod. Phys.*, **1990**, *62*(2), 251-341.

[213] Belega, E. D.; Tatarenko, K. A.; Trubnikov, D. N.; Cheremukhin, E. A. The dynamics of water hexamer isomerization. *Russ. J. Phys. Chem. B*, **2009**, *3*, 404.

[214] Qian, X.; Wei, X. Glucose isomerization to fructose from ab initio molecular dynamics simulations. *J. Phys. Chem. B*, **2012**, *116*, 10898-10904.

[215] Perkins, J.; Edwards, E.; Kleiv, R.; Weinberg, N. Molecular dynamics study of reaction kinetics in viscous media. *Mol. Phys.*, **2011**, *109*, 1901-1909.

[216] Tiberio, G.; Muccioli, L.; Berardi, R.; Zannoni, C. How does the trans-cis photoisomerization of azobenzene take place in organic solvents? *ChemPhysChem*, **2010**, *11*, 1018-1028.

[217] Poater, A.; Ragone, F.; Correa, A.; Szadkowska, A.; Barbasiewicz, M.; Grela, K.; Cavallo, L. Mechanistic insights into the cis-trans isomerization of ruthenium complexes relevant to catalysis of olefin metathesis. *Chem. Eur. J.*, **2010**, *16*, 14354-14364.

[218] Jardón-Valadez, E.; Bondar, A.-N.; Tobias, D. J. Dynamics of the internal water molecules in squid rhodopsin. *Biophys. J.*, **2009**, *96*, 2572-2576.

[219] Mantz, Y. A.; Branduardi, D.; Bussi, G.; Parrinello, M. Ensemble of transition state structures for the cis-trans isomerization of N-methylacetamide. *J. Phys. Chem. B*, **2009**, *113*, 12521-12529.

[220] Toxvaerd, S. Molecular dynamics simulations of isomerization kinetics in condensed fluids. *Phys. Rev. Lett.*, **2000**, *85*, 4747-4750.

[221] Wan, S. Z.; Wang, C. X.; Xu, Y. W.; Shi, Y. Y. Molecular dynamics simulations of cis-trans isomerization for a proline-containing tripeptide in solution. *Chem. Phys.*, **1996**, *211*, 227-234.

[222] den Otter, W. K.; Briels, W. J. The reactive flux method applied to complex isomerization reactions: Using the unstable normal mode as a reaction coordinate. *J. Chem. Phys.*, **1997**, *106*, 5494-5508.

[223] Rosenberg, R. O.; Berne, B. J.; Chandler, D. Isomerization Dynamics in Liquids By Molecular Dynamics. *Chem. Phys. Lett.*, **1980**, *75*, 162-168.

[224] Gershinsky, G.; Pollak, E. Isomerization of trans-stilbene: Theory for pressure dependence of the rate. *J. Chem. Phys.*, **1998**, *108*, 9186-9187.

[225] Gershinsky, G.; Pollak, E. Unimolecular reactions in the gas and liquid phases: A possible resolution to the puzzle of the trans-stilbene isomerization. *J. Chem. Phys.*, **1997**, *107*(3), 812-824.

[226] Gershinsky, G.; Pollak, E. Theoretical study of the trans-stilbene isomerization reaction in ethane. *J. Chem. Phys.*, **1996**, *105*, 4388-4390.

[227] Tapavicza, E.; Meyer, A. M.; Furche, F. Unravelling the details of vitamin D photosynthesis by non-adiabatic molecular dynamics simulations. *Phys. Chem. Chem. Phys.*, **2011**, *13*, 20986-20998.

[228] Yamamoto, T. Quantum statistical mechanical theory of the rate of exchange chemical reactions in the gas phase. *J. Chem. Phys.*, **1960**, *33*, 281-289.

[229] Miller, W. H. Quantum mechanical transition state theory and a new semiclassical model for reaction rate constants. *J. Chem. Phys.*, **1974**, *61*, 1823-1834.

[230] Miller, W. H.; Schwartz, S. D.; Tromp, J. W. Quantum mechanical rate constants for bimolecular reactions. *J. Chem. Phys.*, **1983**, *79*, 4889-4898.

[231] Miller, W. H. Direct and correct calculation of canonical and microcanonical rate constants for chemical reactions. *J. Phys. Chem. A*, **1983** *102*, 793-806.

[232] Geva, E.; Shi, Q.; Voth, G. A. Quantum-mechanical reaction rate constants from centroid molecular dynamics simulations. *J. Chem. Phys.*, **2001**, *115*, 9209-9222.

[233] Chandler, D. Statistical mechanics of isomerization dynamics in liquids and the transition state approximation. *J. Chem. Phys.*, **1978**, *68*, 2959-2970.

[234] Pollak, E.; Talkner, P. Reaction rate theory: what it was, where is it today, and where is it going? *CHAOS*, **2005**, *15*, 026116 (11 pages).

[235] Eyring, H. The Activated Complex in Chemical Reactions. *J. Chem. Phys.*, **1935**, *3*, 107-115.

[236] Widom, B. Reaction kinetics in stochastic models. *J. Chem. Phys.*, **1971**, *55*, 44.

[237] Skinner, J. L.; Wolynes, P. G. Relaxation processes and chemical kinetics. *J. Chem. Phys.*, **1978**, *69*, 2143.

[238] Montgomery Jr., J. A.; Chandler, D.; Berne, B. J. Trajectory analysis of a kinetic theory for isomerization dynamics in condensed phases. *J. Chem. Phys.*, **1979**, *70*, 4056.

[239] Kubo, R.; Toda, M.; Hashitsume, N. *Statistical Physics II - Nonequilibrium Statistical Mechanics*. Springer-Verlag, Berlin, **1983**.

[240] Ankerhold, J.; Grabert, H. Quantum effects in barrier dynamics. *Chem. Phys.*, **1996**, *204*, 27.

[241] Wang, J.; Wolf, R. M.; Caldwell, J. W.; Kollamn, P. A.; Case, D. A. Development and testing of a general amber force field. *J. Comput. Chem.*, **2004**, *25*, 1157-1174.

[242] Bayly, C. I.; Cieplak, P.; Cornell, W. D.; Kollman, P. A. A well-behaved electrostatic potential based method using charge restraints for deriving atomic charges: The resp model. *J. Phys. Chem.*, **1993**, *97*, 10269-10280.

[243] Cieplak, P.; Cornell, W. D.; Bayly, C.; Kollman, P. A. Multiconformational RESP Methodology to Biopolymers : Charge Derivation for. *J. Comput. Chem.*, **1995**, *16*(11), 1357-1377.

[244] Cornell, W. D.; Cieplak, P.; Bayly, C. I.; Kollman, P. A. Application of RESP Charges To Calculate Conformational Energies, Hydrogen Bond Energies, and Free Energies of Solvation. *J. Am. Chem. Soc.*, **1993**, *115*, 9620-9631.

[245] Grossfield, A. An implementation of WHAM : the Weighted Histogram Analysis Method Alan Grossfield. *"WHAM: an implementation of the weighted histogram analysis method", http://membrane.urmc.rochester.edu/content/wham/, version 2.0.6.*

[246] Andrea, T. A.; Swope, W. C.; Andersen, H. C. The role of long ranged forces in determining the structure and properties of liquid water. *J. Chem. Phys.*, **1983**, *79*, 4576-4584.

[247] Ryckaert, J.-P.; Ciccotti, G.; Berendsen, H. J. C. Numerical integration of the cartesian equations of motion of a system with constraints: molecular dynamics of n-alkanes. *J. Comput. Phys.*, **1977**, *23*(3), 327-341.

[248] Arruda, B. C.; Smith, B.; Spears, K. G.; Sension, R. J. Ultrafast ring-opening reactions: a comparison of α-terpinene, α-phellandrene, and 7-dehydrocholesterol with 1,3-cyclohexadiene. *Faraday Discuss.*, **2013**, *163*, 159-171.

[249] Arruda, B. C.; Peng, J.; Smith, B.; Spears, K. G.; Sension, R. J. Photochemical ring-opening and ground state relaxation in α-terpinene with comparison to provitamin D3. *J. Phys. Chem. B*, **2013**, *117*, 4696-4704.

[250] Bastida, A.; Soler, M. A.; Ziga,J.; Requena, A.; Kalstein, A.; Fernndez-Alberti, S. Hybrid Quantum/Classical Simulations of the Vibrational Relaxation of the Amide I Mode of N-Methylacetamide in D_2O Solution. *J. Phys. Chem. B*, **2012**, *116*, 2969-2980.